Cathodes for Solid Oxide Fuel Cells Operating at Low Temperatures

Samson, Alfred Junio

Publication date:
2012

Document Version
Publisher's PDF, also known as Version of record

Cathodes for Solid Oxide Fuel Cells Operating at Low Temperatures

Dissertation

In partial fulfillment of the requirements
for the degree of Doctor of Philosophy

Alfred Junio Samson

Department of Energy Conversion and Storage
Technical University of Denmark

February 2012

Academic Advisors:

Nikolaos Bonanos
Department of Energy Conversion and Storage
Technical University of Denmark
DK-4000 Roskilde
Denmark

Martin Søgaard
Department of Energy Conversion and Storage
Technical University of Denmark
DK-4000 Roskilde
Denmark

This study was funded by the Department of Energy Conversion and Storage, Technical University of Denmark

The study was carried out in the time period between February 2009 and February 2012

Acknowledgments

This dissertation would have not been possible without the help of many inspiring and generous people. I am forever thankful to the contribution of each one during the course of my work.

I owe my sincere gratitude to my supervisors, Nikolaos Bonanos and Martin Søgaard, gracious mentors who have shared their time, attention, and ideas to make my graduate study a fruitful and stimulating experience. Their advice and comments have been instrumental in shaping up my research. Both have imparted a sense of positivity and optimism that have been motivational for me during the grueling times of Phd pursuit.

I am deeply grateful to Peter Vang Hendriksen for his invaluable suggestions in my research and for all his professional advice. I am very much thankful to Per Hjalmarsson for sharing his expertise on cathodes and cell testing, and for having always the time for discussion. My appreciation also goes to Johan Hjelm for his insightful suggestions to improve the work on anode supported cells. I am also indebted to Finn Willy Poulsen for spending his time with me in the set up and discussion of high temperature XRD. Special thanks to Ruth Knibbe for having the patience in performing transmission electron microscopy on my multiphased samples.

The $Ca_3Co_4O_{9+\delta}$ study would have not materialized without the generosity of the thermoelectric group. I am very thankful to Ngo Van Nong for his help in preparing the powder samples and for sharing his command on the subject of thermoelectric materials. His energy and enthusiasm toward research have been very contagious. I also thank Nini Pryds for providing valuable suggestions to improve the discussion on the $Ca_3Co_4O_{9+\delta}$ text.

I owe sincere and earnest thankfulness to the lab technicians. Thanks to: Jens F. S. Borchsenius for making himself always available to help in electronic stuffs, Ulla Forsberg for sharing her knowledge on screen printing, Lene Knudsen for showing me

the way to properly prepare inks, Carsten Gynther Sørensen for patiently running my samples for thermal analysis, Ebtisam Abdellahi for preparing my samples for SEM, and Charlotte Maul and Annelise Hoffbeck for being always ready to help with a smile in finding things in the lab.

I gratefully acknowledge the funding provided by the Department of Energy Conversion and Storage that made this Phd work possible.

I appreciate the friendship of Mohammed Hussain, Qiang Hu, Suresh Kannan and all the other colleagues who have made my stay in the Department a fun and enjoyable experience.

My heartfelt thanks also goes to my family and friends in the Philippines, who have always been supportive of my studies. Finally, I wish to thank my wife, Shiena Marie Samson, for her love, encouragement, patience, faithful support, and understanding throughout my studies.

Alfred Junio Samson
Technical University of Denmark, Risø Campus
February 2012

Abstract

This dissertation focuses on the development of nanostructured cathodes for solid oxide fuel cells (SOFCs) and their performance at low operating temperatures. Cathodes were mainly fabricated by the infiltration method, whereby electrocatalysts are introduced onto porous, ionic conducting backbones. High performance cathodes were obtained from strontium-doped lanthanum cobaltite (LSC) infiltrated - $Ce_{0.9}Gd_{0.1}O_{1.95}$ (CGO) ionic conducting backbone. Systematic tuning of the CGO and LSC firing temperatures and LSC loading resulted in a cathode with low polarization resistance, R_p = 0.044 Ω cm^2 at 600°C. The most promising cathode was integrated onto an anode supported cell and it was found that the cell exhibits electrochemical stability with no measureable degradation during 1500 h operation at 700°C. $LaCoO_3$ and Co_3O_4 infiltrated - CGO cathodes were also investigated and revealed that these nanoparticulate infiltrates have good oxygen reduction capabilities. The significance of the choice of ionic conducting backbone was also addressed by replacing the CGO with $Bi_2V_{0.9}Cu_{0.1}O_{5.35}$ (BICUVOX). Cathodes with a BICUVOX backbone exhibit performance degradation not observed in LSC infiltrated - CGO cathodes with increasing LSC firing temperature, highlighting the importance of materials compability over higher ionic conductivity. The potential of $Ca_3Co_4O_{9+\delta}$ as an electrocatalyst for SOFCs has also been explored and encouraging results were found i.e., R_p = 0.64 Ω cm^2 for a $Ca_3Co_4O_{9+\delta}$/CGO 50 vol % composite cathode at 600°C. A 1-dimensional model has been developed in order to understand and predict the the performance of cathodes prepared by LSC infiltration. With the model, it was possible to extract an expression for the area specific resistance associated with oxygen surface exchange for the infiltrated LSC. The extracted values are significantly lower than literature values suggesting that the performance of LSC-infiltrated cathodes could not be explained by downscaled microstructure alone. A series of microstructural parameter variations are presented and discussed with the goal of guiding future studies on infiltrated cathodes.

Resumé

Denne afhandling omhandler udviklingen af nanostrukturerede lavtemperaturkatoder til keramiske brændselsceller. Katoderne er primært fremstillet ved brug af en infiltreringsmetode, hvor en eletrokatalysator infiltreres ind i en porøs, oxidionledende bærestruktur. Højtydende katoder kunne fremstilles ud fra strontiumdoteret lantancobaltit (LSC) infiltreret i en porøs bærestruktur af $Ce_{0.9}Gd_{0.1}O_{1.95}$ (CGO). Systematiske variationer af den porøse CGO-bærestruktur, LSC-afbrændingstemperaturen og mængden af infiltreret LSC blev foretaget, og en katodepolarisationsmodstand på $R_p = 0.044\ \Omega\ cm^2$ ved 600°C blev opnået. Den mest lovende katode blev integreret på en anodesupporteret brændselscelle og fremragende stabilitet over 1500 timer ved 700°C blev demonstreret. Katoder af henholdsvis $LaCoO_3$ og Co_3O_4 infiltreret ind i porøse bærestrukturer af CGO blev også fremstillet og undersøgt. En god ydeevne blev også fundet for disse katoder, såfremt infiltratet blev holdt nanokrystallinsk. Betydningen af valget af bærestruktur blev også undersøgt ved at udskifte CGO med $Bi_2V_{0.9}Cu_{0.1}O_{5.95}$(BICUVOX). Katoden med en BICUVOX-bærestruktur udviste en degradering i ydeevne, som ikke er observeret for de tilsvarende LSC-infiltrerede CGO-katoder. Dette viser betydningen af materialekompatibilitet frem for en høj ionledningsevne i den porøse bærestruktur. $Ca_3Co_4O_{9+\delta}$ er også blevet undersøgt som muligt katodemateriale. Lovende resultater ($R_p = 0.64\ \Omega\ cm^2$ ved 600°C for en kompositkatode bestående af $Ca_3Co_4O_{9+\delta}$:CGO 50/50 vol %) blev fundet. En endimensionel katodemodel, der inkluderer infiltrering, er blevet udviklet for opnåelse af en bedre forståelse af infiltreringselektroder samt mulighed for at forudsige ydeevnen af disse katoder. Med modellen er det muligt at bestemme et udtryk for den arealspecifikke modstand associeret med iltudveksling for infiltreret LSC. De bestemte værdier er signifikant lavere end tilsvarende i litteraturen, hvilket sandsynliggør, at de mindre dimensioner i en infiltreringselektrode ikke alene er ansvarlig for den forbedrede ydeevne. For at forklare de eksperimentelt bestemte resultater var det nødvendigt at antage, at iltudvekslingen af det infiltrerede LSC er forøget. En række parametervariationer blev foretaget med modellen, og betydningen af disse, for fremtidige studier omhandlende infiltreringselektroder, er blevet diskuteret.

Contents

Chapter 1

Introduction

1.1 Solid oxide fuel cells as an alternative energy source

The solid oxide fuel cell (SOFC) is just one of the choices in a wide range of alternative energy sources that are gaining much attention in recent years, but why SOFCs? The SOFC is an electrochemical device that converts chemical energy directly into electrical energy. The non-necessity of intermediate conversions of the fuel to other energy forms implies that in theory, the electrical conversion efficiency of SOFC can be greater than any conventional energy conversion technology. Another attractive feature of fuel cells is that their efficiency is independent of size. The size flexibility implies that fuel cells are attractive to a wide range of applications, from small scale power sources for portable and mobile electronic devices, to small auxiliary power units for automotive applications and combined heat and power systems for homes, to large central power generating system. The low noise and low NO_x [1] emission in fuel cells also make them an attractive environment friendly energy source.

In light of these advantages, it can be seen that indeed, SOFCs offer a lot of promise as an alternative energy source. The technology has been known for quite some time since the first demonstration of a solid conducting oxide ions by Walter Nernst in 1899 [2]. However, even with more than a century of research and development, the widespread commercialization of SOFCs has remained elusive. The roadblocks to this realization are primarily the cost and reliability of these devices. To attain commercial viability, efforts to date have been directed to materials selection and better design of SOFC components. Specifically, the development of SOFCs that operate at interme-

diate temperature range (500 - 700 °C) has become one of the main SOFC research goals. By operating at these temperatures, it is expected that cell degradation problems such as interdiffusion between cell components are mitigated. Lowered operating temperatures also enable the use of cheap metal supports and steel interconnects [3] thereby cutting materials cost significantly.

The benefits of lowered operating temperatures also have their accompanying disadvantages. Slow electrode kinetics [4] and decrease in oxygen ion conductivity [5, 6] at lowered operating temperatures lead to high polarization resistances. To date, the performance of most of the reported cells is usually limited by the electrodes, thus requiring the search and development of improved anodes and cathodes for low-to-medium temperature SOFCs. This dissertation concentrates on the cathode performance issues at lowered operating temperatures and explores materials and fabrication methods to address these problems.

1.2 SOFC fundamentals

The basic structure of SOFCs consists of two porous electrodes separated by a dense, gas tight oxygen-ion-conducting electrolyte. The operating principle of a SOFC, with O_2 as oxidant and H_2 as fuel, is illustrated in Fig. 1.1. The oxygen supplied at the cathode is reduced, forming oxide ions which migrate to the anode through the oxygen-ion-conducting electrolyte. The oxide ions react with hydrogen at the anode to form water and release electrons.

Under cell operating conditions the cell produces current as long as the reactants are provided to the electrodes. For hydrogen as fuel, the following electrochemical reactions occur at the two electrodes:

$$\frac{1}{2}O_2(g) + 2e^- \longrightarrow O^{2-}(\text{cathode}) \tag{1.1}$$

$$O^{2-} + H_2(g) \longrightarrow H_2O(g) + 2e^-(\text{anode}) \tag{1.2}$$

The overall reaction is

$$\frac{1}{2}O_2(g) + H_2(g) \longrightarrow H_2O(g) \tag{1.3}$$

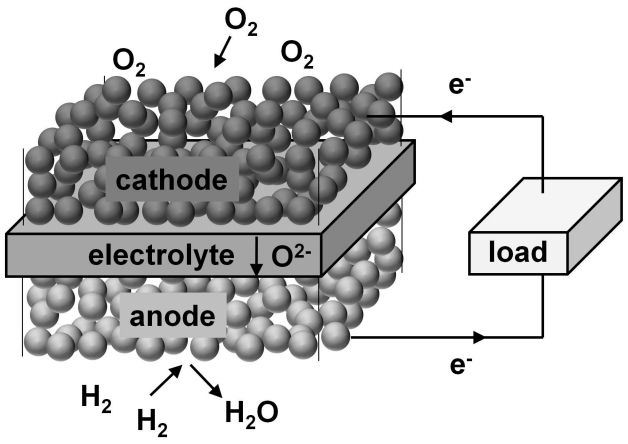

Figure 1.1: Schematic of a solid oxide fuel cell.

The corresponding Nernst equation for the overall potential of the cell reaction is simply

$$E = E^0 + \frac{RT}{2F} \ln \left(\frac{p_{\mathrm{H_2}} p_{\mathrm{O_2}}^{\frac{1}{2}}}{p_{\mathrm{H_2O}}} \right) \tag{1.4}$$

where E^0 is the ideal standard potential for the cell reaction, R is the gas constant, T is the cell temperature in Kelvin, F is the Faraday constant, and $p_{\mathrm{H_2}}$,$p_{\mathrm{O_2}}$,$p_{\mathrm{H_2O}}$, are the hydrogen, oxygen (cathode side), and water partial pressures, respectively. E represents the maximum available voltage from one cell.

During operation where current is drawn from the cell, the cell voltage is lower than that in 1.4 due to several internal irreversible loss mechanisms. In terms of voltages, these losses are termed as polarizations. In SOFCs, the three dominant polarizations are ohmic, activation and concentration polarizations [7]. Ohmic polarization arises from resistances to electronic and ionic transport through the various cell components. Activation polarization is associated with resistance on electrode reaction kinetics and is dominant at low current densities. At high current densities, the concentration polarization dominates as the transport of reactive species to the electrolyte/electrode interface becomes a limiting factor for the cell reaction.

1.3 SOFC cathodes: Fundamentals and materials

The primary function of the cathode in a fuel cell based on an oxygen-conducting electrolyte is to facilitate the reduction of oxygen as outlined in equation 1.1. It is important to consider that 1.1 is a multi-step process, usually comprised of several parallel reaction pathways [8, 9]. Fig. 1.2 outlines two distinguishable mechanisms for common cathode materials. For pure electronic conductors such as Pt or doped $LaMnO_3$ which has a relatively low ionic conductivity, the surface path shown in Fig. 1.2a is the most probable mechanism. In the surface path, adsorbed oxygen diffuses along the surface toward the triple-phase boundary (TPB) where electrolyte, electrode, and gas phase meet, followed by complete ionization and ionic transfer into the electrolyte. For mixed ionic and electronic conductors such as doped - $LaCoO_3$, and $LaFeO_3$, oxygen incorporation is no longer restricted to the TPB but a bulk path shown in Fig. 1.2b is also possible. In this case, the oxygen is adsorbed on the electrode surface, and then gets dissociated and ionized. The O^{2-} ions are incorporated into the electrode material and diffuse towards the electrode/electrolyte boundary. The extension of the electrochemical reaction zone is crucial as this entails a lower cathode polarization resistance. For this reason, the use of mixed ionic and electronic conductors (MIECs) in SOFCs has been gaining a lot of attention.

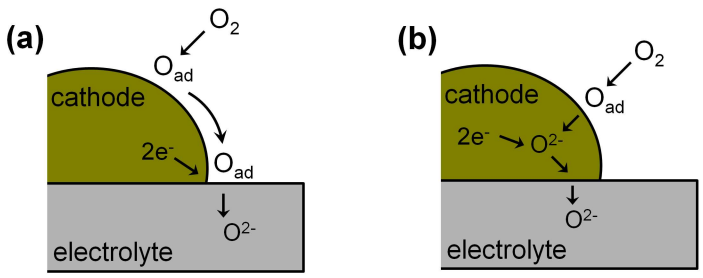

Figure 1.2: Schematic showing two generalized paths for oxygen reduction and incorporation. (a) surface path and (b) bulk path.

The extent of the electrochemical reaction zone is not the only determining factor for a high performance SOFC cathode. The cathode material has to meet various requirements in catalytic activity, thermodynamic stability, and component compatibility. In general, the highest possible electronic conductivity is desired at the operating temperature and oxidizing environment to minimize the ohmic losses of the cathode. The

electrocatalytic activity is also an important parameter to be considered in selecting cathode materials. In this case, the electrode material should be able to catalyze the dissociation of the oxygen molecules and their incorporation into the electrolyte. The oxygen incorporation rate and the oxygen flux through the materials can be characterized in terms of two parameters: the oxygen surface exchange coefficient and the oxygen diffusion coefficient, where the oxygen isotope exchange technique provides meaningful data on these parameters [10]. In relation to other cell components, the cathode should have chemical and dimensional stability in the environments encountered during cell operation and during fabrication. Ideally, the thermal expansion coefficient (TEC) of the cathode material should match match that of the electrolyte material. Furthermore, the cathode should be morphologically stable, i.e., its microstructure should be maintained during long term operation.

For many years, manganese-based perovskites have been widely recognized as the materials best suited for the cathode of a high-temperature SOFC that uses a zirconia-based electrolyte and operates at temperatures higher than 800 °C. In particular, strontium doped - $LaMnO_3$ (LSM) is the most commonly used since these have high electronic conductivity in oxidizing atmospheres (> 100 S cm^{-1} at 800 °C in air [11]) and relatively well matches the thermal expansion of yttria-stabilized zirconia (YSZ), the electrolyte of choice for high temperature SOFCs[†]. The main problem with LSM is its negligible ionic conductivity. This implies that the electrochemical reaction zone is only confined to the TPBs. While the low ionic conductivity of the LSM is not an issue for SOFCs operating at temperatures above 800 °C, it is generally accepted that the electrochemical performance of LSM based cathodes is not sufficient for IT-SOFCs.

For operation at low temperatures, materials which have high mixed electronic and ionic conductivities and exceptional electrochemical activity for oxygen reduction, such as perovskite-related ferrites and cobaltites are preferred. Ferrites possess considerably higher ionic and electronic conductivity than manganite systems at temperatures below 800 °C. Ferrites of most interest for SOFC applications are from the system $La_{1-x}Sr_xFe_{3-\delta}$ (LSF), where the highest electronic and ionic conductivity is known for $x = 0.5$ [14]. LSF cathodes reported in literature have shown promising performance with respect to power density and stability at 750 °C [15, 16]. Cobaltites are one of the most interesting cathode materials for SOFC due to their exceptional electrochemical activity for oxygen reduction. Like in the case of manganites and ferrites, cobaltites of most interest are from the perovskite-type $La_{1-x}Sr_xCoO_{3-\delta}$ (LSC). LSC exhibit higher

[†]LSM, TEC $\sim$ 11 - 12.5 $\times$ 10^{-6} K^{-1} [12]; YSZ, TEC $\sim$ 10 $\times$ 10^{-6} K^{-1} [13]

oxygen diffusivity and better catalytic activity for oxygen reduction than other known cathode materials. Unfortunately, many of the cobalt containing perovskites have very high thermal expansion coefficients ($> 20 \times 10^{-6}$ K^{-1}) and very high reactivity with the common SOFC electrolyte YSZ. Perhaps, one of the most studied cathode material today is the ferro-cobaltite composition $La_{1-x}Sr_xFe_{1-y}Co_yO_{3-\delta}$ (LSCF). In particular, the composition $La_{0.6}Sr_{0.4}Co_{0.2}Fe_{0.8}O_{3-\delta}$ is the most common since it provides a compromise between thermal expansion match, conductivity, and reactivity with the electrolyte such as YSZ. Ferrites and cobaltites are mainly used today together with electrolytes that have higher ionic conductivity than YSZ such as doped ceria. Other perovskite-type materials that are widely studied today are $Sm_xSr_{1-x}CoO_{3-\delta}$ (SSC) [17, 18] and $Ba_{1-x}Sr_xCo_{1-y}Fe_yO_{3-\delta}$ (BSCF) [19].

Aside from perovskite type materials, ordered double perovksites and K_2NiF_4 structure type materials also possess some properties that make them suitable as cathode for SOFCs. Ln_2NiO_4 (Ln = La, Pr, Nd), which exhibits a K_2NiF_4 structure, have been observed to possess high diffusivity for interstitial oxygen ions [20].In particular, $LaNiO_{4+x}$ has been found to have an oxygen diffusivity higher than $La_{0.6}Sr_{0.4}Co_{0.2}Fe_{0.8}O_{3-\delta}$ but significantly lower than $La_{0.3}Sr_{0.7}CoO_{3-\delta}$ [21].Another encouraging aspect for these materials is that their thermal expansion coefficients (e.g. La_2NiO_4, TEC $\sim$ 11 - 13 $\times$ 10^{-6} K^{-1} [22])are relatively close to that of common SOFC electrolytes such as YSZ, CGO, and LSGM. Despite these advantages, the performance of these materials in SOFCs is found to be inferior to that of common ferro-cobaltite cathodes, thus requiring the need for further research. Another interesting class of materials for cathodes is the ordered double perovskites which are mixed conductors represented by the general formula $AA'Co_2O_{5+x}$ (A = rare earths, Y and A' = Ba, Sr). In these materials, rapid oxygen transport is thought to originate from A-site ordering brought about by the combination of rare earths and Ba or Sr in the A-site [23]. Several researchers working on various compositions (e.g. $GdBaCo_2O_{5+x}$, $PrBaCo_2O_{5+x}$, $NdBaCo_2O_{5+x}$, $EuBaCo_2O_{5+x}$, $SmBa_{0.5}Sr_{0.5}Co_2O_{5+x}$) have reported promisingly low values of area specific resistance especially when these materials are used as single phase or employed together with CGO as composite cathodes (e.g. $GdBaCo_2O_{5+x}$, 0.5 Ω cm^2 at 650°C [24]; 50:50 wt% $SmBa_{0.5}Sr_{0.5}Co_2O_{5+x}$ + CGO, 0.12 Ω cm^2 at 600°C [25]).

1.4 Strategies to improve LT-SOFC cathode performance

1.4.1 Composite cathodes

It has long been realized that due to the very low oxide ion conductivity in bulk LSM, the active sites for O_2 reduction reaction are mainly confined to the TPB sites. Hence the electrochemical performance of a cathode fabricated by depositing a layer of LSM onto a dense YSZ electrolyte is mainly dictated by the amount of active contact sites of LSM on or near the YSZ electrolyte. An idea to enlarge the active sites is to extend the electrolyte through the whole thickness of the LSM layer. Thus, attempts have been made to use a composite of LSM and YSZ as a cathode for SOFCs. Several works have demonstrated that the area specific resistance of pure LSM cathode is significantly higher than that of LSM-YSZ composite cathode [26, 27, 28, 29]. For instance, Murray and Barnett [26] reported that at 700°C, the R_p for pure LSM cathode is 7.82 Ω cm^2 while that for a LSM-YSZ composite cathode is 2.49 Ω cm^2. Aside from the extension of electrochemical active region, the use of composites is seen to enhance the electrode microstructural stability and adherence to the electrolyte [30].

The present shift to IT-SOFCs has necessitated the replacement of YSZ with a material of higher ionic conductivity such as Gd-doped ceria (CGO) and the replacement of LSM with a mixed ionic and electronic conductor (MIEC) such as those discussed in section 1.3. The use of MIEC is based on the idea that oxygen exchange occurs at a larger surface of the material due to its appreciable amount of oxygen vacancies and faster oxide ion transport within the material. To date, the most common MIEC that is used as a SOFC cathode is LSCF. Several works have indeed demonstrated that the electrochemical performance of porous LSCF cathodes is far superior to that of LSM cathodes. It should be noted, however, that MIECs generally have a high activation energy for oxygen ion diffusion compared to common solid oxide electrolytes such as CGO. Therefore, the ionic conductivity of MIECs drops more sharply with decreasing temperature. For example, the activation energy for oxygen tracer diffusion (E_{A,D^*}) in $La_{0.6}Sr_{0.4}CoO_{3-\delta}$ is 176 kJ mol^{-1} [31] while that for CGO is 87 kJ mol^{-1} [32]. Thus, the addition of a high ionic conductivity phase such as CGO is advantageous at reduced temperatures. Moreover, as the common electrolyte of choice for IT-SOFCs is also CGO, the presence of the same phase in the cathode should serve to enhance the compatibility of the electrode and the electrolyte by improving the adhesion and the thermal expansion match of the materials. For the reasons mentioned above, composite

cathodes are favored over cathodes only containing a MIEC, even though one removes a significant portion of the catalytic active area.

Further reduction in the target operating temperatures makes it necessary to explore other composite cathode materials. In the case of the ionic conducting component, there are many materials with higher ionic conductivity than YSZ that can be considered. Aside from doped cerias, certain compositions of perovskite-type ABO_3 phases derived from $LaGaO_3$, e.g. $La_{0.9}Sr_{0.1}Ga_{0.9}Mg_{0.1}O_3$ (LSGM) [33], and oxide phases derived from Bi_2O_3, e.g. $Bi_2V_{0.9}Cu_{0.1}O_{5.35}$ (BICUVOX) [34], possess higher ionic conductivity than that of stabilized zirconia as seen in Fig. 1.3. All these systems, however, carry several disadvantages. LSGM, for instance, suffers from significant reactivity with perovskite electrodes under oxidizing conditions and the formation of secondary phases in the course of processing [35, 36]. Bismuth oxides are known for their thermodynamic instability under reducing atmospheres [37] such as in an SOFC anode. While reducing conditions can be avoided if they're used strictly in oxidizing atmospheres such as in a SOFC cathode, the relatively low melting point of Bi_2O_3 (823°C [38]) and their reactivity with common IT-SOFC materials such as doped ceria and LSCF [39, 40] make them very challenging material to work with. Doped cerias exhibit relatively easy reducibility at low oxygen partial pressures, leading to increased electronic conductivity [41]. This is a problem if the material is intended for use as an SOFC electrolyte as the electronic conduction results in a reduced open circuit voltage which translates into decreased efficiency [6]. However, if these materials are maintained under oxidizing conditions such as in a SOFC cathode, there appears to be no issues reported in literature. Thus, from these materials, doped cerias appear to be the most promising component material in a SOFC cathode in terms of thermomechanical stability and reactivity with common electrocatalysts.

As reliability is very important in a SOFC cathode, it is imperative that a careful choice of components for a composite cathode is made based on chemical and thermomechanical compatibility. The compatibility of these components with the electrolyte should also be considered. For example, it is almost always a necessity for cobaltite- and ferrite-based materials to be in a composite due to the TEC of these materials being incompatible with common SOFC electrolytes. A number of studies have demonstrated that promising ionic conducting components described above can be utilized together with the cathode materials described in Section 1.3 by proper materials selection. In one example, Xia and Liu [44] demonstrated that BICUVOX can be effectively employed in a composite cathode using Ag (57 wt%) as the electronic conducting component. This

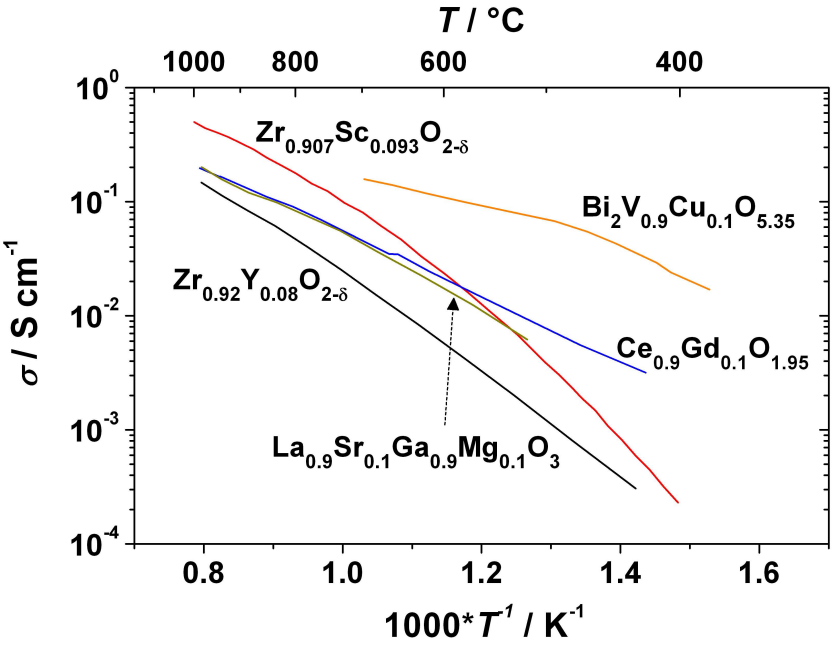

Figure 1.3: Ionic conductivities of selected SOFC electrolytes [34, 33, 13, 42, 43].

composite cathode showed remarkable performance at low temperatures (e.g. 0.53 Ω cm^2 at 500°C) using CGO as electrolyte.

Once proper materials are selected for the composite cathode, the next strategy to improve the cathode performance is to optimize the amount of ionic conducting component. Several optimization studies have been performed for different composite cathodes and found that the optimum amount of IC component falls in range 30 - 60 % [30]. The addition of more IC phase results in an increase in R_p due to a decrease in the amount electrocatalysts.

1.4.2 Fabrication techniques

The method to prepare cathodes is as important as the materials selection. This includes the processing parameters such as temperature and atmosphere conditions which determine the final microstructure and/or composition of the cathode. The choice of fabrication method commonly depends on the cell design, which can be tubular, planar, and more recently, "micro-fabricated". The present work is geared towards planar and micro-fabricated designs.

The common way to prepare cathodes in a planar design, particulary in an anode supported SOFC, is to deposit the cathode after preparing the anode/electrolyte assembly, employing conventional techniques such as slurry coating, screen printing, tape casting, and wet powder spraying [45]. The deposition is followed by drying and then sintering. In these methods, the thickness of the deposited layer after sintering are usually several micrometers. The sintering temperature is a compromise between the formation of sufficient connection between the electrode and the electrolyte and the prevention of solid-state reactions between the components of the cathode mixture and the electrolyte. Sometimes, the sintering temperature range is narrow such that the choice of materials for a two-phase combination is limited. For example, YSZ requires at least 1000°C to attain sufficient connection of grains [46].

The surface areas of cathodes prepared by conventional methods are usually insufficient to enable a low area specific resistance at low operating temperatures. Thus, there has been a greater interest on nano-scaled cathodes which possess inherently large electrochemically active surface area. Nano-scaled cathodes that operate at low-to-medium temperature range also have the potential for small scale power source applications such as in portable and mobile electronic devices with power rating of several watts. There are at least two ways to prepare nano-sized particle electrodes as illustrated in Fig. 1.4. The first is by depositing the entire cathode in a nanostructured way as shown schematically in Fig. 1.4a. The thicknesses of electrodes attained in this method range in the submicron to several micrometers level and are usually used in μ-SOFCs [47]. Most relevant thin film deposition techniques for SOFC applications include vacuum deposition techniques such as physical vapor deposition (PVD), chemical vapor deposition (CVD), and pulsed laser deposition (PLD), and liquid precursor-based thin film deposition such as spray deposition, electrophoretic deposition (EPD) and spin- and dip- coating. A good review of these techniques can be found in Ref. [48]. Cathode materials that are used in μ-SOFCs so far include Pt [49, 50], LSC [51], LSCF [52], and BSCF [53]. In one example, electrode polarization resistances as low as 0.023 Ω cm^2 at 600°C for nanoporous $La_{0.6}Sr_{0.4}CoO_{3-\delta}$ thin films (150 - 200 nm) prepared by dip coating have been reported [54]. However, it was also shown in that study that significant degradation of performance (increase to 0.069 Ω cm^2 at 600°C) occurs after 100 h of annealing. Employing spray pyrolysis technique, Darbandi et al. [55] obtained electrode polarization resistance of 0.038 Ω cm^2 at 600°C for nanoporous $La_{0.25}Ba_{0.25}Sr_{0.5}Co_{0.2}Fe_{0.8}O_{3-\delta}$ (LBSCF) thin films ($\leq$ 1 μm). However, the stability was not reported for this thin film. Although promising, the use of this deposition method in μ-SOFC development

still has several issues that need to be addressed before commercialization is realistic. These issues are among others, optimization of electrode microstructure, substrate choice and component durability [56].

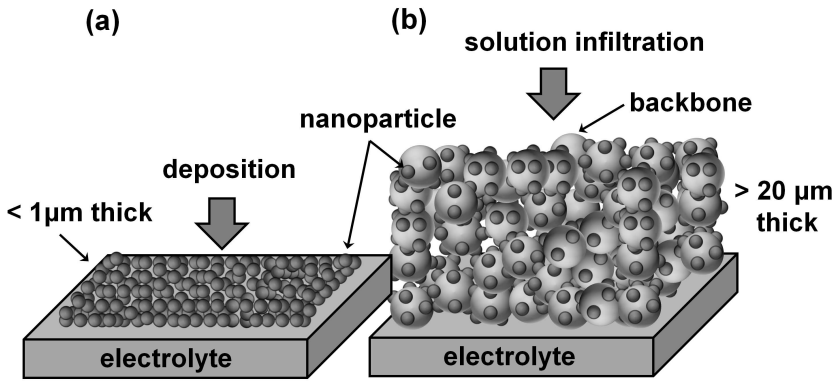

Figure 1.4: Two ways to prepare nano-sized particle electrodes. (a) the entire electrode is prepared is prepared in a nanostructured way using special deposition techniques or (b) a solution is infiltrated into an ion conducting porous backbone such that nanoparticles are obtained after calcination.

The second method to prepare cathodes is through infiltration as shown in Fig. 1.4b. In this technique, a liquid solution usually composed of dissolved metal nitrates is introduced into a pre-formed porous backbone (usually an electrolyte material), followed by drying and calcining to produce the desired oxide phase. Aside from the easy and relatively cheap processing compared to the first method, the main benefit of using a nano-composite cathode instead of a single phase nano-structured MIEC cathode is that the bulk oxygen ion conductivity of the ionic conducting backbone is much higher than that of the MIEC. This allows the electrochemically active thickness of the electrode to be spread out further in the electrode and thus increases the catalytically active surface area significantly. Another advantage of this method is that infiltration can be done independently of other sintering steps. It means that it can be additionally employed on electrodes prepared by conventional methods such as screen printing, tape-casting or spraying. The possible reactions between infiltrated and backbone phases is also minimized because of the relatively low calcination temperature involved. The infiltration method has shown improved electrochemical performance using a variety of candidate cathode materials. Several combinations including perovskite/YSZ [46, 57, 58] and perovskite/ceria, especially lanthanum cobaltite-based perovskite/ceria combinations [59, 60, 61, 62] have been studied. Despite the advantage of improved

electrochemical performance over their conventionally prepared counterparts, the use of infiltrated cathodes in actual fuel cells is limited due to the perceived instability of nanoparticulate infiltrates during long term operation. Specifically, the high surface area nanoparticles are highly prone to coarsening and grain growth, which increases R_p.

1.5 Approach to develop LT-SOFC cathodes

The move to very low target operating temperatures ($< 600°C$) for SOFCs in this dissertation requires a significant step in terms of materials selection and fabrication techniques. As seen from the review above, the literature presents a wide range of choices for developing cathodes that would potentially operate at temperatures $< 600°C$. The review of fundamental cathode processes, basic cathode material requirements and the limiting factors during operation in an actual device was also essential to the choice of materials and methods in this dissertation. Prior to performing fabrication and characterization of the cathodes considered in this work, it was essential to also gather information on the performance, in terms of R_p, of a wide variety of cathode systems found in literature at very low temperature, e.g. 400 °C. A comparison of the performances in the form of R_p vs. reciprocal absolute temperature for different types of cathode systems and materials found in literature [19, 26, 44, 63, 64, 65] and from this work is shown in Fig. 1.5. It should be noted that comparing these systems directly may not be correct due to different microstructures, materials, and electrolyte used. Further, the systems shown may not be optimized. Nonetheless, the comparison provides an idea for a base cathode system that can be explored for LT-SOFC cathodes. The list of materials and fabrication techniques may not be exhaustive, but Fig. 1.5 may be viewed as a representation of the advances in cathode materials selection and fabrication techniques. There are several key trends that can be found in Fig. 1.5. The use of materials which have mixed ionic and electronic conductivity, specifically that of ferrite and cobaltite-based materials produces the lowest R_p's. It also appears that the use of composites produces lower R_p than that of using pure electrocatalyst. The choice of the component which has a high ionic conductivity is also important in this case. The fabrication technique is also important, as the cathodes prepared by techniques which produces a very fine microstructure such as infiltration easily outperforms those which are prepared conventionally.

Based on the review of materials properties, fabrication methods, and performance

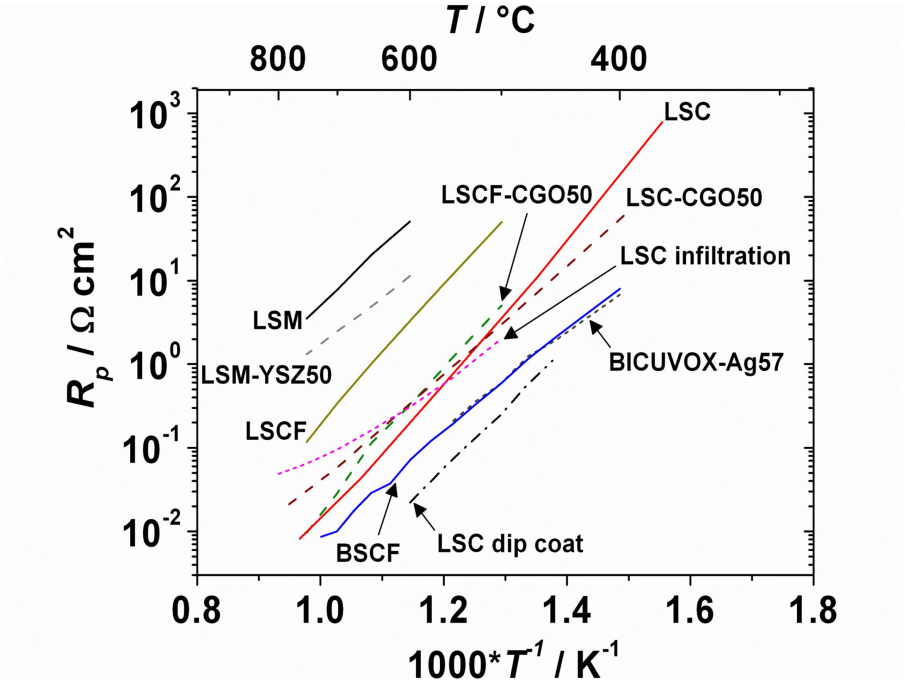

Figure 1.5: R_p vs. reciprocal absolute temperature plot of various cathode materials and systems. LSM - $La_{0.8}Sr_{0.2}MnO_3$ [26], LSM-YSZ50 - $La_{0.8}Sr_{0.2}MnO_3$-50 wt % yttria stabilized zirconia [26], LSCF - $La_{0.6}Sr_{0.4}Co_{0.2}Fe_{0.8}O_{3-\delta}$ [63], LSCF-CGO50 - $La_{0.6}Sr_{0.4}Co_{0.2}Fe_{0.8}O_{3-\delta}$-50 wt % $Ce_{0.8}Gd_{0.2}O_{2-\delta}$ [63], LSC - $La_{0.6}S_{0.4}CoO_{3-\delta}$ (This work), LSC-CGO50 - $La_{0.6}S_{0.4}CoO_{3-\delta}$ 50 wt % $Ce_{0.8}Gd_{0.2}O_{2-\delta}$ (This work), LSC infiltration - $La_{0.6}S_{0.4}CoO_{3-\delta}$ infiltrated into $Ce_{0.8}Sm_{0.2}O_{1.9}$ backbone [63], BSCF - $Ba_{0.5}Sr_{0.5}Co_{0.8}Fe_{0.2}O_{3-\delta}$ [19], BICUVOX-Ag57 - $Bi_2V_{0.9}Cu_{0.1}O_{5.35}$ - 57 wt % Ag [44], LSC dip coat - $La_{0.6}S_{0.4}CoO_{3-\delta}$ deposition by dip coating [65]

.

comparisons presented above, the main route followed in this work is the infiltration technique with lanthanum cobaltite-based perovskite as an electrocatalyst and Gd-doped ceria as an ionic conducting component (mainly as a backbone). An effort to optimize the sintering temperature of the CGO backbone, the amount of LSC infiltrate, and the firing temperature of LSC was undertaken. A long term test was also conducted to assess the possible problems that could be encountered in an actual SOFC operation. The cathode was integrated into an anode supported SOFC and the whole cell is evaluated for its long term performance. An extension of study using a BICUVOX backbone was also conducted to assess the importance of the backbone material. BICUVOX was seen as a very promising backbone material because of its significantly

higher ionic conductivity than CGO especially at low temperatures. To guide the development of LT-SOFC cathodes using the infiltration technique, a model which accounts for the microstructure and the transport properties of the backbones and infiltrates has been developed. A short study on exploring the potential of $Ca_3Co_4O_{9+\delta}$ as a cathode is also performed.

1.6 Overview

The dissertation contains 8 chapters including the Introduction and Conclusion and Recommendations for Future Work. Each chapter is presented as an independent article and arranged such that succeeding chapters follow logically from the previous ones. Care is taken to avoid repetitions especially in the introduction and the experimental parts of each chapters but some overlap between these is unavoidable. The co-authors of the chapter are stated in a footnote. This chapter provides a literature survey on cathode materials and fabrication techniques and presented a rationale for the selection of the materials and the processing routes employed in the dissertation. It also gives a short background on SOFC and SOFC cathode fundamentals. Chapter 2 presents a study on the performance of cathodes prepared by infiltration of $La_{0.6}Sr_{0.4}CoO_{3-\delta}$ (LSC) into a porous Gd-doped ceria (CGO) backbone. Chapter 3 deals with the performance of cathodes fabricated by infiltrating $LaCoO_3$ and Co_3O_4 into a CGO backbone. Chapter 4 investigates the feasibility of replacing the CGO backbone with BICUVOX. Chapter 5 discusses the long term performance of an anode supported SOFC, where an LSC infiltrated-CGO cathode has been integrated into the cell. Chapter 6 explores the potential of $Ca_3Co_4O_{9+\delta}$ as cathode for SOFCs. Chapter 7 presents a 1-dimensional model that takes into account the ionic and electronic conductivities and the microstructure of both the backbone and the infiltrate material to understand and predict the performance of infiltrated cathodes. Chapter 8 provides the conclusion and recommendations for future work. There are two Appendices in the dissertation. The first presents the results of the electrochemical testing of Pt paste/noninfiltrated backbone cathodes. The second presents the results of the electrochemical testing of cathodes prepared by wet deposition of aqueous nitrate solution of LSC onto dense CGO without any porous backbone.

Chapter 2

LSC infiltrated - CGO cathodes[†]

2.1 Introduction

Infiltration with perovskite/ceria combination, specifically lanthanum cobaltite-based perovskite/doped ceria combination [59, 60, 61, 62] produces cathodes with relatively low area specific resistance. Lanthanum cobaltite-based perovskites are chosen since they have good catalytic activity for oxygen reduction and possess oxide ion conductivity and electronic conductivity that are higher than lanthanum manganites [30]. The choice of a ceria based backbone material, rather than zirconia is due to its higher ionic conductivity, particularly at lower temperatures and its stability towards perovskites containing Co and/or Fe [66]. When these materials are employed in the infiltration method, it is important to have an understanding of the effect of the processing parameters on the performance of the cathode in order to have a guide for developing cathodes that operate at lower temperatures.

This chapter presents a systematic study of the effect of processing paramaters such as the backbone firing temperature, the infiltrate firing temperature, and the amount of loading of the infiltrate material on the peformance of a cathode prepared by infiltration of $La_{0.6}Sr_{0.4}CoO_{3-\delta}$ (LSC) into a porous $Ce_{0.9}Gd_{0.1}O_{1.95}$ (CGO). A short study on the long term stability of the infiltrated cathode is also presented.

[†]Parts of this chapter has been published as A. Samson, M. Søgaard, R. Knibbe, and N. Bonanos,"High performance cathodes for solid oxide fuel cells prepared by infiltration of $La_{0.6}Sr_{0.4}CoO_{3-\delta}$ into Gd-doped ceria", *J. Electrochem. Soc.*, 158 (2011) B650-B659.

2.2 Experimental

Backbones of $Ce_{0.9}Gd_{0.1}O_{1.95}$ (CGO) were prepared by screen printing an in-house CGO ink onto both sides of a 5 x 5 cm^2, dense 180 μm thick CGO electrolyte (KERAFOL). These samples were then fired at 1050, 1150 and 1250°C for 2 h, resulting in all cases in a backbone with a thickness of about 25 μm. Polished cross section of the CGO backbones fired at different temperatures are shown in the SEM micrographs in Fig. 2.1. The porosities are 71 %, 64 % and 59 % for backbones fired at 1050, 1150, and 1250°C, respectively. The porosities are estimated based on counting black and gray pixels of the SEM micrographs of the polished samples, which refers to pores and grains, respectively. This image analysis was performed using simple phase analyzer software developed in our group. These backbone structures were all infiltrated to study how the electrochemical performance varies with the backbone firing temperature. The number of infiltrations was also varied in order to study the effect of the amount of LSC infiltrated material on electrode performance. The large symmetric cells were cut in squares with an approximate size of 6 $\times$ 6 mm^2 which were used for infiltration and subsequently, impedance measurements.

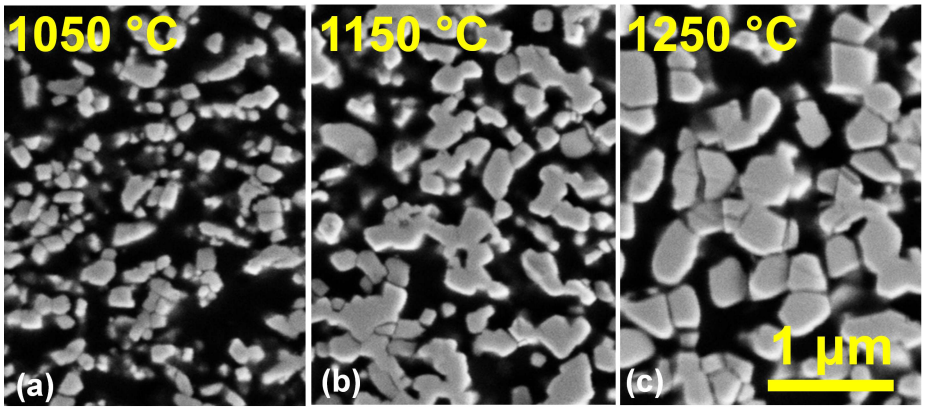

Figure 2.1: SEM micrographs of the polished cross section of the CGO backbone at different firing temperatures.(a) 1050°C, (b) 1150°C, (c) 1250°C. The scale bar holds for all SEM micrographs.

The LSC precursor solution used for infiltration was prepared by mixing individual

aqueous stock solutions of La, Sr, and Co nitrates in precise amounts to obtain the nominal composition $La_{0.6}Sr_{0.4}Co_{1.05}O_{3-\delta}$. The concentrations of the stock solutions were determined by thermogravimetry. A surfactant was also added in the solution to improve dispersion. The concentration of the resulting solution was about 1 M. The nitrate solution was then pipetted onto the backbone and infiltrated into the CGO pores by capillary force. The samples dripped with nitrate solution were placed under rough vacuum (1 mbar) to extract trapped air in the backbones and enhance the penetration of the solution into the backbone. The application of vacuum also serves to enhance the removal of water as to leave the metal nitrates with surfactant well dispersed on the backbone. To introduce sufficient amounts of LSC, the infiltration was repeated several times. In this study, infiltration was done 6, 9 and 12 times. The samples were precalcined at 350°C for one hour after each infiltration in order to completely remove the residues of the surfactant. To estimate the LSC loading, the weight of the sample with infiltrated LSC was measured after the desired number of infiltrations. Considering the likelihood that LSC is yet to be formed at 350°C, the measured weight is corrected for the total weight loss associated with the formation of LSC. The correction is obtained by performing a thermogravimetric analysis of a sample powder from the LSC solution heated at 350°C. The total weight loss after forming a seemingly stable compound at 1000°C was found to be about 20 %. Assuming complete formation of LSC, infiltration with 6, 9, and 12 times yields approximately 12, 17, and 19 vol % out of the total volume of one cathode side, for all the backbones. The values are calculated from the estimated thickness of 25 μm for all backbones and the theoretical density of LSC, 6.63 g cm^{-3} [67]. The initial and final (after infiltration) porosities of all the CGO backbones are summarized in Table 2.1. Examination of the SEM micrographs of fractured surfaces of the infiltrated backbones revealed that the infiltrate material seems to reach all the way through to the CGO backbone - CGO electrolyte interface.

CGO backbone firing (°C)	Initial porosity (vol. %)	Final porosity (vol%) after infiltration 6×	9×	12×
1050	71	59	54	52
1150	64	52	47	45
1250	59	47	42	40

Table 2.1: Summary of the initial and final (after infiltration) porosities of all the CGO backbones. The estimation of the final porosity assumes complete formation of LSC.

The backbone structures with infiltrated materials were finally heated in-situ in an electrochemical setup at temperatures ranging from 300 - 900°C to investigate the performance with varying firing temperature. A sketch of the measurement setup is shown in Fig. 2.2a. The temperature profile used during impedance measurement is shown in Fig. 2.2b. This cyclic, stepped temperature profile was chosen such that impedance spectra from each measuring temperature can be obtained as the samples were heated and cooled progressively in the rig. After the samples had been heated to a maximum firing temperature (labeled as "T_{max}"), they were cooled to 300°C and then an impedance measurement was performed. The samples were then heated further, carrying out impedance measurements at each step. In this way, impedance spectra from each measuring temperature from their corresponding T_{max} could be compared. For example, at 300°C, there are a total of six different spectra that can be compared corresponding to T_{max} = 400°C to T_{max} = 900°C. Obviously, fewer spectra can be compared at higher measuring temperatures (e.g., only four spectra can be compared at 600°C corresponding to T_{max} = 600°C, T_{max} = 700°C, T_{max} = 800°C and T_{max} = 900°C).

In all cases, Pt paste (Ferro GmbH) and a Pt mesh were used for current collection of the symmetric cells. Separate tests established that the electrochemical performance of the Pt paste was greatly inferior to that of standard perovskite based SOFC cathodes. Electrochemical impedance spectroscopy (EIS) was carried out using either a Hioki impedance analyzer with a frequency range from 0.06 Hz to 100 kHz or a Solartron 1260 impedance analyzer with a frequency range from 0.06 Hz to 1 MHz. The samples were tested with a 50 mV amplitude AC signal under open-circuit conditions. The data were normalized with the measured geometrical area of the sample, approximately 0.3 cm^2 and were divided by two to account for the symmetric structure of the cell. The data were corrected for the series inductance of the measurement rig, determined by measurements of the set up without any samples. Typical values obtained in this way gave values of the inductance in the range of 60-80 nH. Microstructures of the infiltrated LSC were characterized using a Zeiss Supra 35 scanning electron microscope. Three samples were also inspected with a JEOL 3000F Transmission Electron Microscope (TEM) operated at 300 kV. The samples were prepared by infiltrating the CGO powder with the aforementioned nitrates and subsequently sintered at 500, 700 and 900°C. The samples were dispersed on Cu grids with a holey carbon film. Several regions were inspected to ensure good sampling. In-situ HT-XRD in air was performed on both LSC powder and CGO - LSC powder mixture using a Bruker D8 Bragg-Brentano

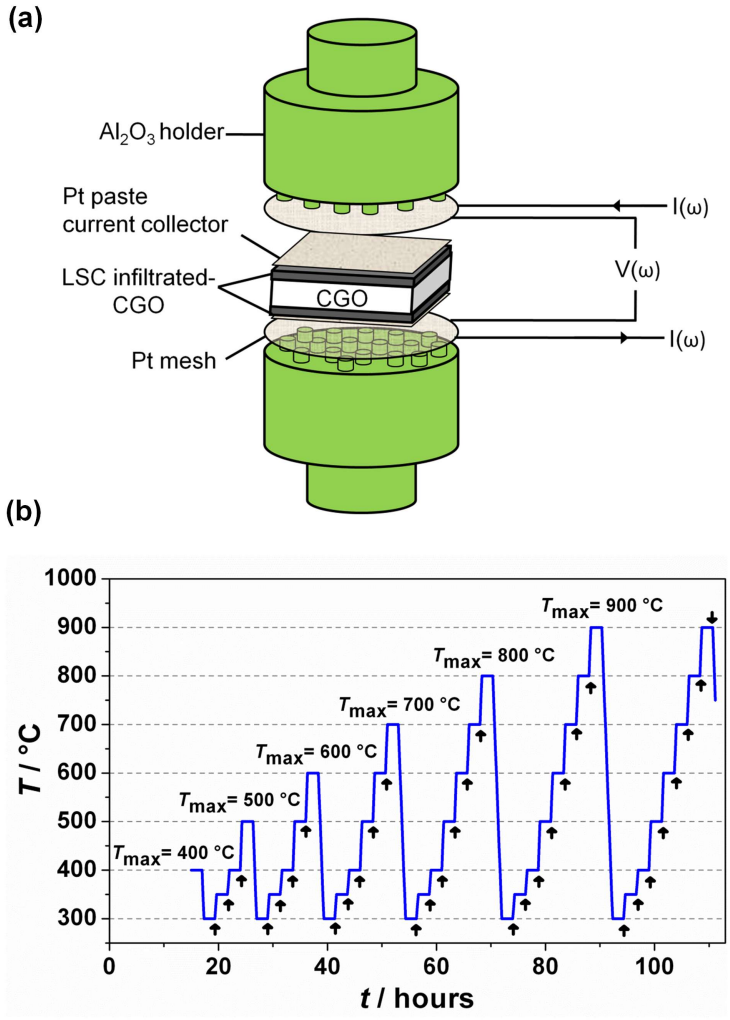

Figure 2.2: (a) Schematic of the measurement setup for electrochemical impedance spectroscopy. (b) The temperature program used in the study. Arrows indicate measurements after holding for two hours at each temperature.

diffractometer with Cu Kα radiation in order to identify the phases formed with respect to firing temperature. The LSC powder was prepared by drying the LSC precursor solution and heating it to 350°C for 1 h in air. The CGO - LSC powder mixture was obtained by mixing the LSC precursor solution into the CGO powder, which in turn had been prepared by heating part of the CGO ink used in screen printing to 1050°C. The mixture was then dried and heated to 350°C for 1 hour in air. A separate study

on the CGO powder revealed a phase pure powder.

2.3 Results and Discussion

2.3.1 Effect of the LSC firing temperature

Phase evolution and microstructure

The in-situ HT-XRD of the LSC precursor powder is shown in Fig. 2.3a. The XRD patterns in Fig. 2.3a are presented in ascending order starting from room temperature (RT1) up to 900°C. An XRD pattern was also taken at room temperature (RT2) after it has been cooled down from 900°C. The XRD peaks shift towards low reflection angles upon heating, reflecting lattice expansion. Additional peak shift is also expected from the expansion of the platinum heating band which displaces the sample from the X-ray plane. The platinum peaks (▲, PDF no. 00-004-0802) in the pattern originate from the heater material. Several phases including $Sr(NO_3)_2$ (*, PDF no. 01-076-1375), $LaO(NO_3)$ (+, PDF no. 00-047-0890) and Co_3O_4 (○, PDF no. 00-043-1003) were identified at RT1 for the LSC powder preheated at 350°C. The identified phases are consistent with previous observations on the thermal decomposition of the component nitrates. Several studies have reported varying thermal decomposition temperature for $Sr(NO_3)_2$ but most fall within the range of 550 - 620°C [68, 69]. The decomposition of $La(NO_3)_3$ to $LaO(NO_3)$ is in the range of 350 to 470°C [70] and of $Co(NO_3)_2$ to Co_3O_4 at 100 - 105°C [71]. As the sample is heated to 400°C, the $Sr(NO_3)_2$ peaks start to vanish indicating decomposition of this material. The peaks originating from $La_2O_2CO_3$ (×, PDF no. 00-048-1113) were also identified. The carbonate formation can be explained by the high reactivity of $LaO(NO_3)$ with the carbon dioxide from atmospheric air [72]. At 500°C, the dominant phase already formed is the desired perovskite (cubic) LSC (■, PDF no. 01-089-5717). Minor secondary phases including the already formed Co_3O_4, and the newly formed $SrCO_3$ (▼, PDF no. 00-05-0418) phase were also detected. The Co_3O_4 was observed until 700°C, after which the cobalt changes its valence to divalent cobalt (CoO) at 800°C (●, PDF no. 01-071-1178). The amount of CoO increased with temperature. Meanwhile, the relative amount of $SrCO_3$ phase increased with temperature up to 600°C. With further heating, the amount of $SrCO_3$ phase decreased until it was no longer detectable at 900°C. At 800°C, an additional secondary phase identified as SrO (¤, PDF no. 00-006-0520) was detected.

The amount increased as the sample is heated further. After the powder was cooled down to RT2, the dominant phase(s) appear to be a mixture of strontium substituted lanthanum cobalt oxide (LSC) related phases and rhombohedral $LaCoO_3$ (□, PDF no. 00-048-0123). Secondary phases including both the Co_3O_4 and CoO phases and SrO were also present at RT2. Several other unidentified peaks which could be coming from perovskite intergrowths and perovskite-related phases are also present.

To study the phase evolution of LSC together with the CGO backbone during operation, a mixture of LSC - CGO powder was also studied in HT-XRD. The infiltrate will hereafter be called "LSC", even though it is composed of several phases as discussed above. Fig. 2.3b shows the in-situ HT-XRD of the LSC - CGO powder mixture. The XRD patterns are presented like in Fig. 2.3a. Aside from the cubic CGO phase (◇, PDF no. 01-075-0161), no other phases different from those identified in the pure LSC powder in Fig. 2.3a were identified. This confirms the known chemical stability of CGO with LSC perovskites. However, there are differences with regards to the temperature at which several phases are detected. With CGO, the $SrCO_3$ phase is now detected at lower temperature (400°C) compared to the observation with pure LSC (500°C). The phase was also no longer detected at 800°C. Further, the SrO phase was now detected at 700°C, compared to 800°C in the LSC powder only. The dominant phase formed after the powder was cooled down from 900°C could not be established from the XRD data due to the overlap of the intense peaks with CGO and other phases. It is possible that it may also be $LaCoO_3$ with a mixture or intergrowths of LSC and perovskite-related structures. In this case, transmission electron microscope is necessary to distinguish the phases. The detection of LSC at high temperatures was not easy due to the proximity of the most intense reflections of LSC with that of CGO phase. It was still identified through the evolution of the shoulder features near the CGO peaks centered at 33°, 47.4°, 59°, and 69.3°. The lanthanum related phases observed in the pure LSC powder may also be present but were difficult to detect due to the overlap of their most intense peaks with that of the CGO phase. The CGO phase may appear to have influenced the kinetics of formation of secondary phases including $SrCO_3$ and SrO leading them to form at lower temperatures but this could not be unambiguously determined with the current data.

Overall, the presented XRD patterns indicate a series of decomposition and formation of the component oxides and the crystallization of the desired LSC phase. It is first noteworthy to mention that the probability of formation of secondary phases in the infiltration method is high due to the different thermal decomposition temperatures of

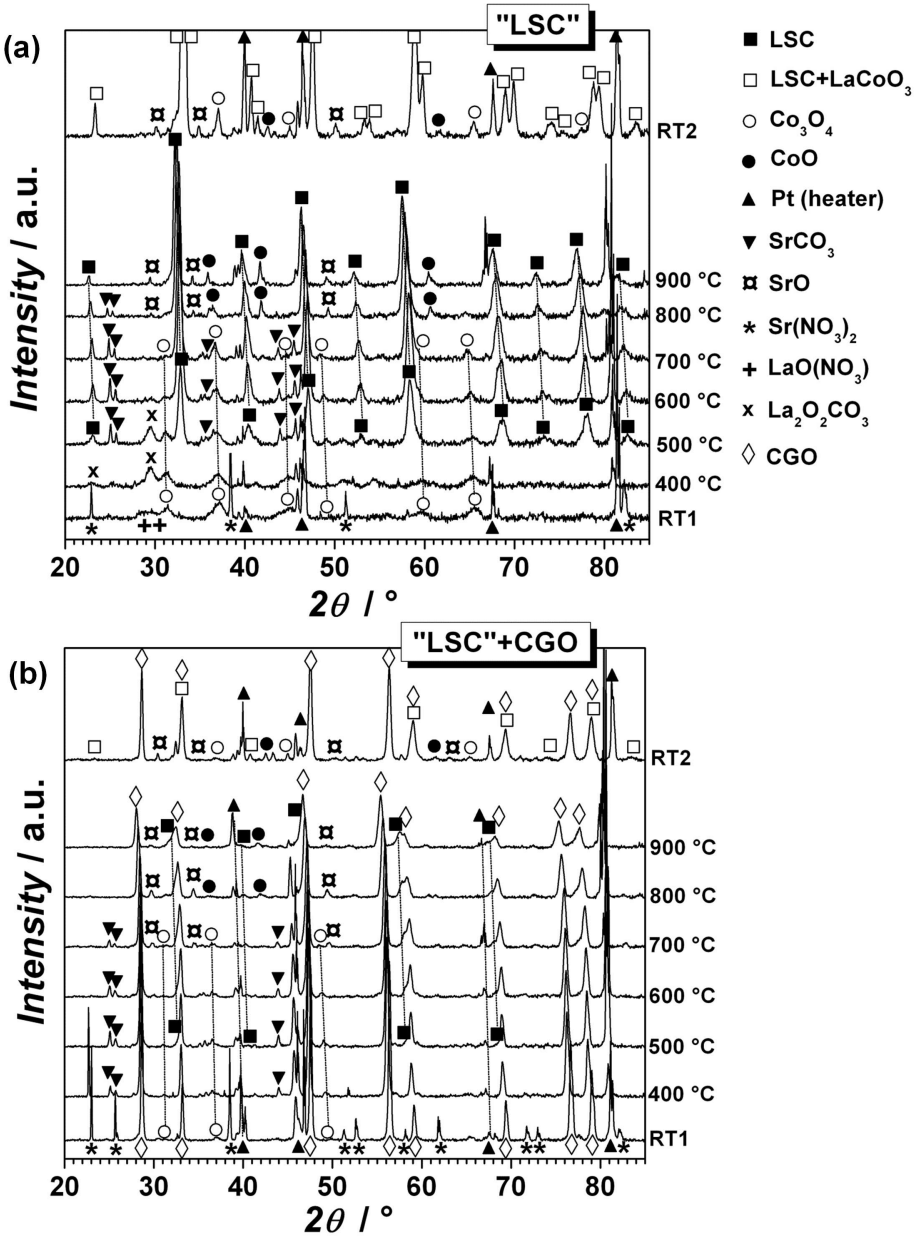

Figure 2.3: HT-XRD patterns of (a) the LSC powder and (b) the LSC-CGO powder mixture at RT≤T≤900°C. Both powders were preheated at 350°C. The CGO powder was fired at 1050°C. Identified phases are labeled.

the precursors. This is further influenced by the atmosphere which they are exposed to and the reactivity of the compounds. The product formation will also certainly depend on the time the sample is subjected to a given temperature. It can be concluded that the dynamics and interaction of phases with temperature is so complex, that it must be carried out in a separate study in order to characterize the interaction of phases and precisely quantify the influence of the secondary phases especially $SrCO_3$ and Co_3O_4 on the cathode performance. $SrCO_3$ has also been reported in many studies and is often an unwanted phase during synthesis [55, 73, 74].

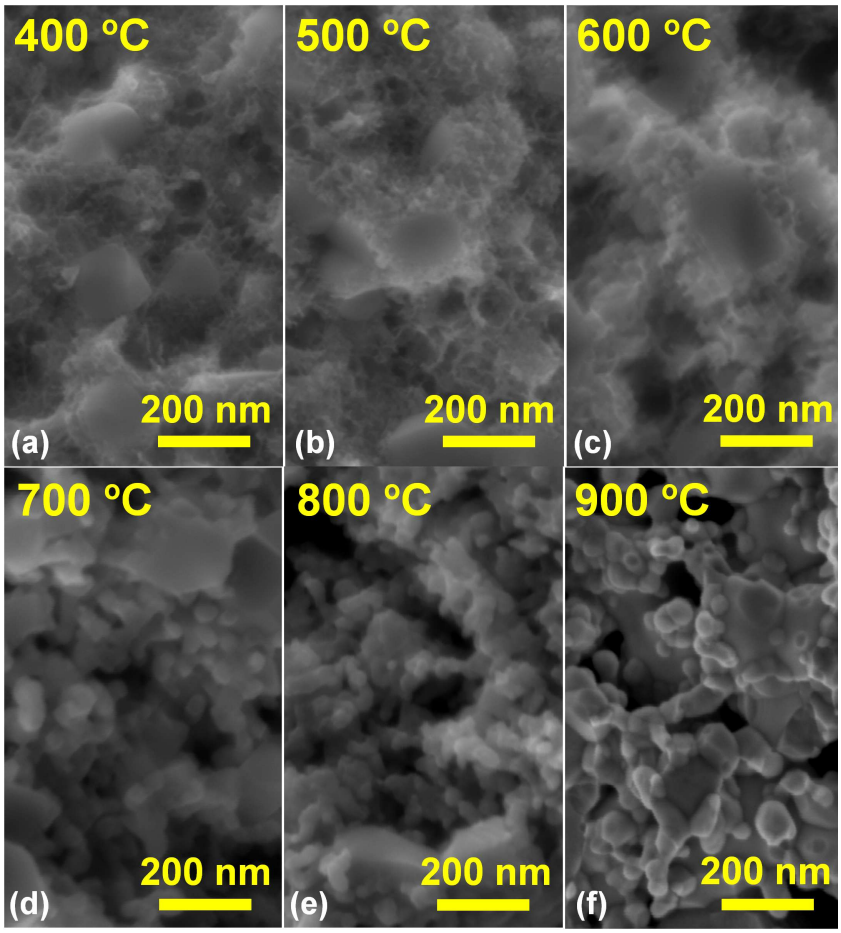

Figure 2.4: SEM micrographs of LSC infiltrated - CGO backbone at different LSC firing temperatures.(a) 400°C, (b) 500°C, (c) 600°C, (d) 700°C, (e) 800°C, and (f) 900°C.

The effect of LSC firing temperature on the nano/microstructure of the infiltrated LSC particles is summarized in the SEM images in Fig. 2.4. The CGO backbone was fired at 1050°C. The CGO particles are seen as interconnected grains of about 200 nm in diameter. The "LSC" is seen as a network of particles partially covering the CGO grains. It should be remembered that this infiltrate material is composed of several phases as seen in HT-XRD. Starting at 400°C, the LSC grains can be seen as a very fine network of interconnected particles (<10 nm) with a cotton-like texture. As the sample is fired at higher temperatures, these very fine interconnected particles start to grow and agglomerate, and at 700°C (Fig. 2.4d) the individual grains can be clearly distinguished. At this point, it is also seen that the connectivity of the grains becomes much poorer as the fine particles starts to agglomerate and segregate from each other. The grain coarsening continues with increasing temperatures, such that at 900°C, the grain size of the LSC particles is about 100 nm. Firing above 700°C also resulted in a coarse yet relatively well-sintered LSC with better contact to the CGO backbone. Morphological details of the infiltrated particles are much better seen in TEM. Figure 2.5 is an overview of TEM micrographs of the three TEM samples - 500, 700 and 900°C (seen in Figs. 2.5a, 2.5b, and 2.5c, respectively). In the 500°C there are two distinct grains present in the sample the large ca. 150 nm sized particles are the CGO particles (also indicated by arrows in Figs. 2.5a-c) and the ca. 5 - 15 nm sized infiltrate particles which are evenly distributed through the CGO matrix. After the sample is heated to 700°C the infiltrate particles have clearly increased in size up to 50 nm in size (Fig. 2.5e). The infiltrate particles retain good connectivity with each other. Finally after firing to 900°C the particles grow to ca. 100 nm in size (Fig. 2.5f) and have a more homogenous elemental distribution than the 500 and 700°C samples. A rough estimate based on simple geometrical considerations can provide an idea on the change in surface area associated with LSC grain coarsening starting at $T_{max} = 700$ where LSC particle sizes can be clearly distinguished. By assuming CGO particles as interconnected spheres of 200 nm diameter spanning the whole volume of the electrode and with LSC spheres partially covering the surface of the CGO grains as schematically shown in Fig. 2.6, the calculated LSC volume specific surface areas corresponding to $T_{max} = 700$°C and $T_{max} = 900$°C are 1.2×10^8 and 1.6×10^8 m^2 m^{-3}, respectively. These values are up to two orders of magnitude larger than for cathodes prepared by standard ceramic methods (10^5 - 10^6 m^2 m^{-3}) [75]. The calculation approximates, based on SEM, an average diameter of 50 and 100 nm LSC particles for $T_{max} = 700$°C and $T_{max} = 900$°C, respectively. Further, the number of LSC particles associated in a single CGO grain for $T_{max} = 700$ and $T_{max} = 900$°C are approximated to be 15 and

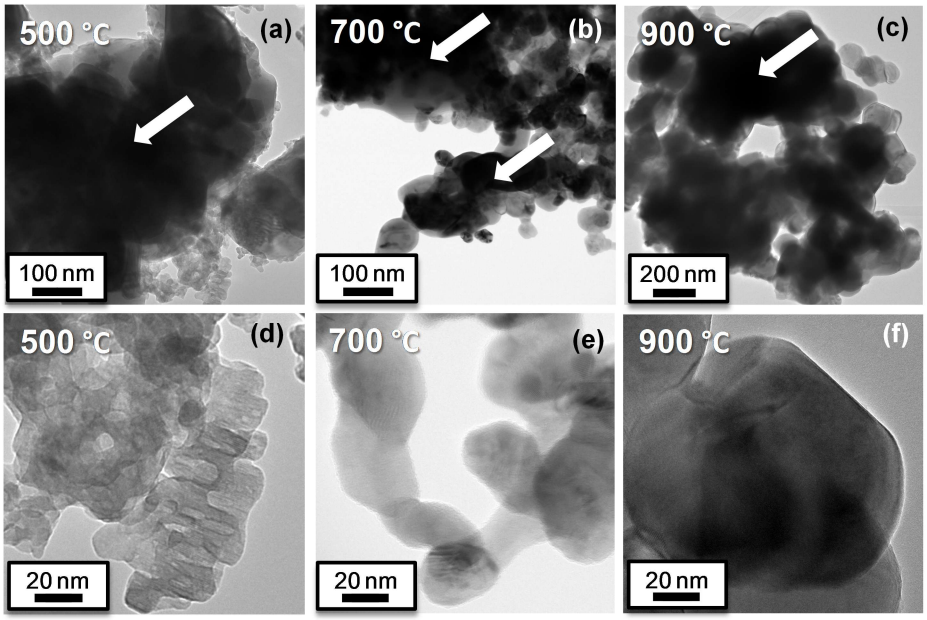

Figure 2.5: TEM micrographs of LSC infiltrate in CGO matrix fired at (a) 500°C, (b) 700°C, and (c) 900°C and the corresponding magnified images of the LSC infiltrate - (d) 500°C, (e) 700°C, and (f) 900°C. The CGO grains which appear much darker in the TEM micrographs are indicated by arrows.

5, respectively. The determination of the coordination number is based on counting the number of particles attached to the CGO grains in one SEM image. It can be expected that a much larger surface area can be obtained at lower firing temperatures since the LSC particles produced are much smaller. However, even though the surface area will be very large, the particles will most likely not have the nominal composition $La_{0.6}Sr_{0.4}Co_{1.05}O_3$.

Evolution of electrochemical performance

The complex plane plots measured in air at 400°C of a representative sample infiltrated 6 times and fired at varying temperatures (T_{max}) are shown in Fig. 2.7a. The CGO backbone was fired at 1050°C. The impedance spectra can be fitted using the equivalent-circuit model shown in Fig 2.7b. Figure 2.7c shows the complex plane plot measured at 400°C, with $T_{max} = 600$°C. Also shown is the best fit to the measured data.

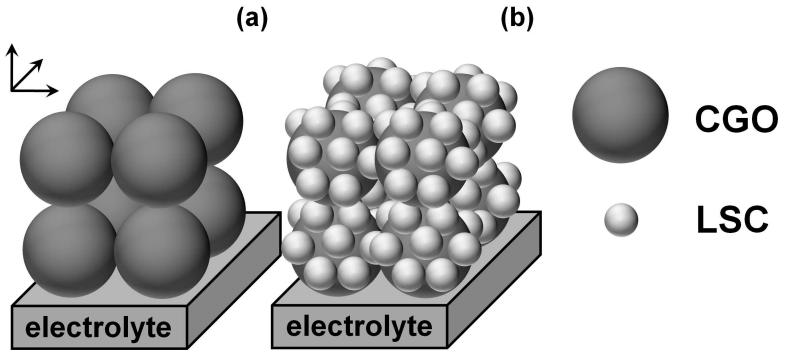

Figure 2.6: Schematic, depicting a simplified model using geometrical considerations to calculate the surface area of LSC particles after firing at $T_{max} = 700°C$ and $T_{max} = 900°C$. (a) part of the CGO backbone on top of the electrolyte (b) part of the cathode structure after firing showing the formed LSC particles on each CGO grain.

As seen in Fig. 2.7c, the goodness of fit is high at 400°C by fitting an equivalent circuit $R_0(R_1CPE_1)(R_2CPE_2)(R_3CPE_3)$. R_0 represents the resistance coming from the CGO electrolyte grain interior while R_1 represents the CGO electrolyte grain boundary resistance. The sum $R_0 + R_1$ is referred to as R_s in this study. The R_2CPE_2 and R_3CPE_3 elements represent electrode processes (CPEs are constant phase elements), thus the sum of R_2 and R_3 is the electrode polarization. These electrode processes are also labeled as high frequency (HF) and medium frequency (MF) electrode responses in Fig. 2.7b. Cathode polarization resistance values discussed below were obtained in this way. The equivalent circuit in Fig. 2.7b is the simplest circuit model that yielded a good fit to the data. While no attempt is made in this study to interpret the two elements representing the total electrode process, the validity of the assignment of each of the fitted processes in the equivalent circuit will be discussed and assessed in subsequent paragraphs.

The impedance spectra in Fig. 2.7a should be viewed together with the temperature program showed in Fig. 2.2b. The first impedance spectrum at 400°C (partly hidden) in Fig. 2.7a is taken after the sample had been fired at $T_{max} = 400°C$. The initial value of R_p was approximately 6.04 Ω cm^2. The sample was then heated to $T_{max} = 500°C$ and then ramped down to obtain impedance spectra at lower temperatures. The impedance spectrum at 400°C now gives a value of $R_p = 5.63$ Ω cm^2. The decrease in

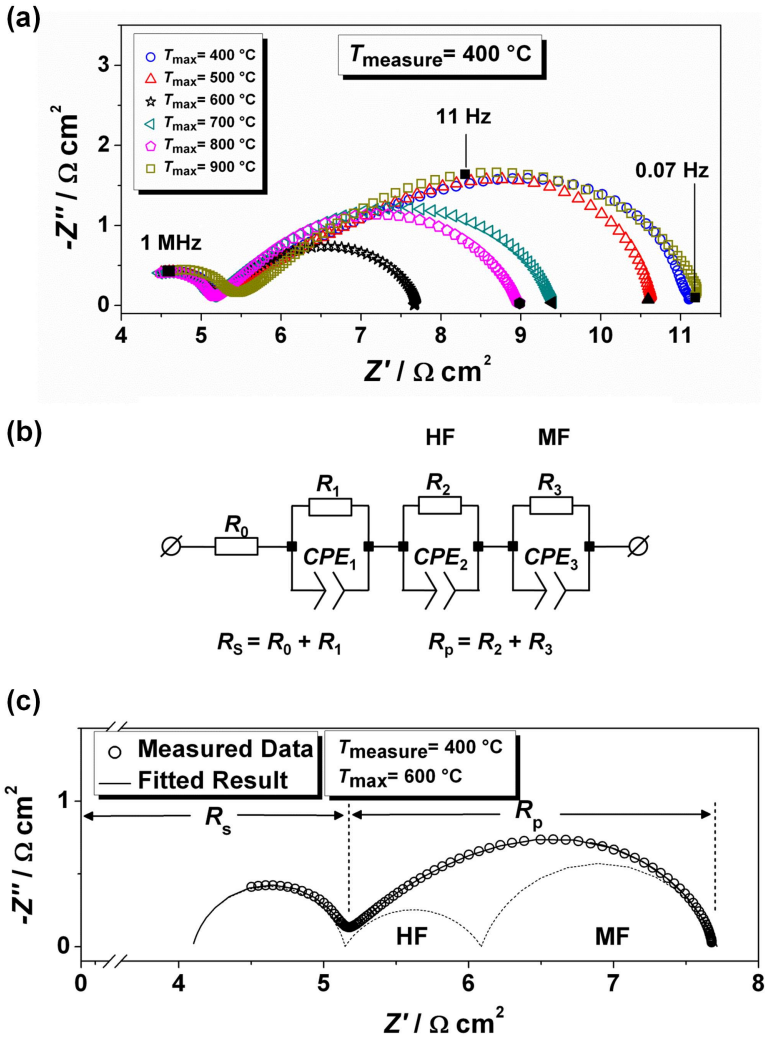

Figure 2.7: (a) Complex plane plots obtained at 400°C of LSC infiltrated CGO samples fired at different temperatures. The sample had been infiltrated 6 times. The lowest frequency data points (solid markers) correspond to 0.07 Hz. (b) The equivalent circuit used to fit the data. (c) Impedance data at 400°C where $T_{\max} = 600$°C. The solid line is the fit.

the cathode polarization resistance is clearly seen in Fig. 2.7a.

The process of heating and cooling was repeated until the sample had reached a maximum of 900°C. It is clear that the R_p at 400°C decreases until it reaches a

minimum of 2.57 Ω cm^2 at T_{max} = 600°C. Above this temperature, the R_p increases until at T_{max} = 900°C, where the measured R_p was 6.01 Ω cm^2 at 400°C. The decrease in R_p as the LSC is fired from 400 to 600°C indicates an improvement in the cathode processes. Likewise, firing above 600°C, the processes related to cathode performance increases R_p. The performance of a noninfiltrated CGO backbone painted with Pt paste was also examined as seen in the Appendix A. It was found that the R_p's and R_s's are significantly higher compared to LSC infiltrated - CGO cathodes suggesting that LSC, and not the Pt paste electrode that provides electrocatalytic activity and that sufficient electronic conductivity is imparted by the LSC infiltrate. Further the trends in R_p or R_s with Pt paste firing temperature does not reflect the behaviors observed for the LSC infiltrated - CGO cathodes considered in this study. This implies that the changes in these values can be mainly attributed to the changes in the LSC infiltrate with firing temperature.

To gain more insight on the processes reflected on the impedance spectra, the sample was tested in varying p_{O_2}. Fig. 2.8a shows representative complex plane plots measured at 600°C (T_{max} = 600°C) for several p_{O_2}'s. A low frequency arc which is highly sensitive to p_{O_2} was observed at high temperature. The arc is only immediately obvious starting from 0.21 atm. The arc is labeled by numbers in Fig. 2.8a. This low frequency behavior of the arc is reminiscent of an RC semicircle. Adler. et al [76] showed that in the case wherein the electrode impedance is dominated by gas phase diffusion, the impedance is given by

$$Z = \frac{R_{gas}}{1 - j\omega R_{gas} C_{gas}} \tag{2.1}$$

where R_{gas} and C_{gas} are the effective resistance and capacitance associated with gas-phase diffusion polarization. Equation 2.1 has the shape of an RC semicircle, with a characteristic resistance scaling as p_{O_2}-1. Having these in mind, a plotting of R_{gas} vs. the relation $1/p_{O_2} - 1$ was performed. Subtraction by 1 was only done to ensure that the plot would fall on the origin. A straight line is observed in Fig. 2.8b suggesting that indeed the process is related to gas diffusion. This was previously seen in the discussion of the amount of infiltration. Fig. 2.8c shows the partial pressure dependence of R_p. It is seen that the processes related to the total resistance of the electrode has $\sim p_{O_2}^{-1/4}$ dependence.

The measured R_p's in air for all T_{max} is plotted against inverse absolute temperature

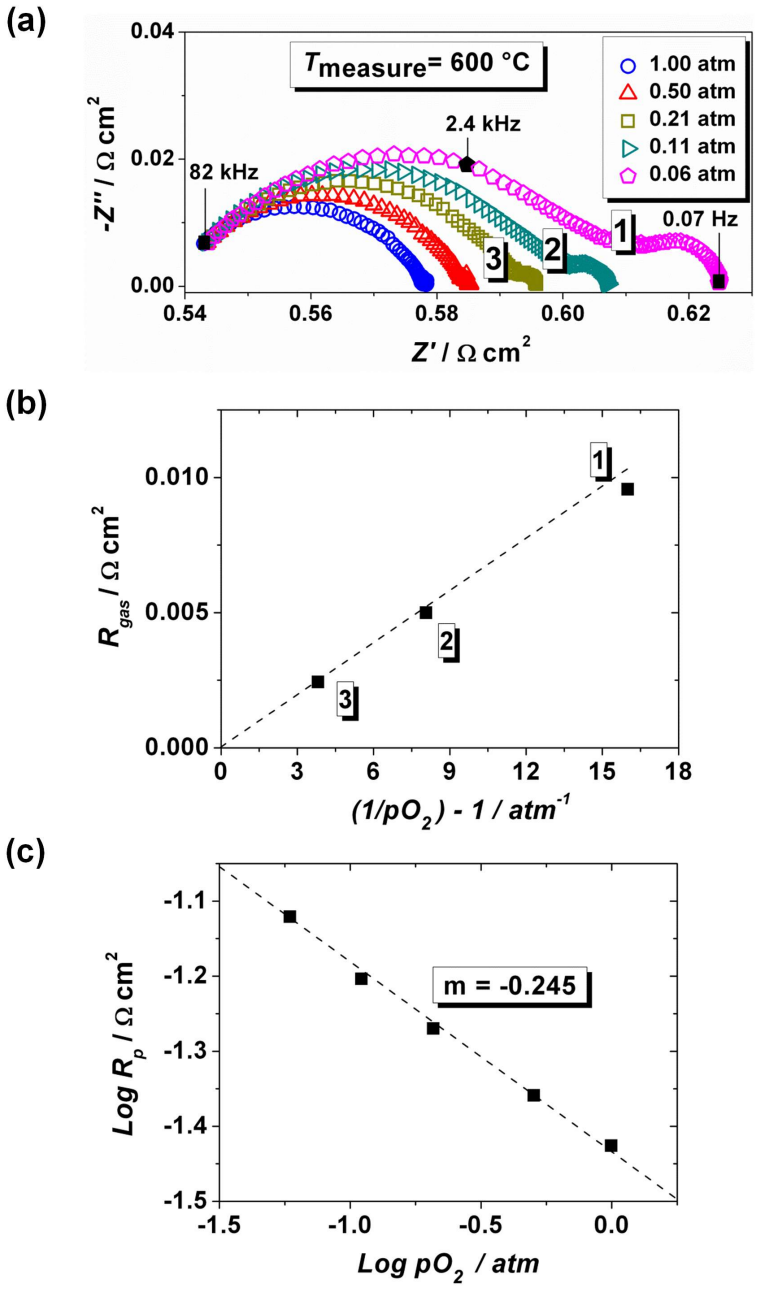

Figure 2.8: (a) Complex plane plots at 600°C of 6x LSC infiltrated CGO backbones at varying oxygen partial pressures. The LSC was fired at 600°C and the CGO backbone at 1050°C. (b) R_{gas} vs. $1/p_{\mathrm{O_2}} - 1$. (c) $p_{\mathrm{O_2}}$ dependence of R_{p}. The slope (m) is also shown.

and are summarized in Fig 2.9a. The R_p's for all temperatures generally increases with increasing firing temperature after $T_{max} = 600°C$. The activation energy obtained when $T_{max} = 600°C$ was 85 kJ mol^{-1}. This is significantly lower than the activation energy obtained from a recent work on nanoporous $La_{0.5}Sr_{0.5}CoO_{3-\delta}$ thin films deposited on YSZ and CGO (103 kJ mol^{-1})[77] and on a $La_{0.6}Sr_{0.4}CoO_{3-\delta}$ thin film deposited on YSZ (135 kJ mol^{-1}) [78]. The activation energy of the prepared electrode is constituted of a very complex interplay between different materials parameters such as the ionic conduction in the CGO phase, the ease of oxygen reduction on the catalyst, and gas transport. That a relatively low activation energy is observed in the present study indicates that the catalyst is highly effective and that the observed electrode activation energy is dominated by the relatively low activation energy for ionic conduction (65 kJ mol^{-1}) [43] in the CGO backbone. The reason for the good performance at T_{max} = 600°C is attributed to a balance of microstructure control and catalyst material formation. To achieve a very good performance, it is desired to scale the feature size of the catalyst phase to the nano-scale to have a very high surface area for oxygen exchange. This is usually achieved by low temperature preparation as in the case of infiltration. Aside from the high surface area, it is also important that the desired catalysts have a high electronic conductivity and that the amount is large enough to form a connective network through the electrode thickness. In the case of this study, although a seemingly very fine network of nanoparticles is already formed below 600°C as seen in Fig. 2.4a and 2.4b, it is evident from the diffractograms in Fig. 2.3a (or 2.3b) that the amount of LSC phase is relatively low. In addition, more undecomposed components such as $SrCO_3$ are present below 600°C (Fig. 2.3a or 2.3b). This entails an increased likelihood of discontinuity among the initially formed electronic and/or ionic conducting nanoparticles and thus the electrode performance is low. Above 600°C, although more LSC was formed, the performance worsened, which must be attributed to a decrease in the surface area for oxygen exchange, formation of phases that are not catalytically active and/or loss of percolation because of LSC grain coarsening. It is interesting to note that in the LSC thin film work of Januschewsky et al. [78], it was found that the surface exchange resistance, R_{surf}, (which dominates their electrode resistance) was smaller for films fired at 600°C, compared to higher temperatures. An intriguing possibility then is that at $T_{max} = 600°C$, the good performance may be due to both high LSC surface area and an R_{surf} value lower than that obtained at other firing temperatures. The idea of lowered R_{surf} has also been put forward in the work of Dieterle et al. [54] on nanoscaled $La_{0.6}Sr_{0.4}CoO_{3-\delta}$ prepared by dip coating. They have invoked an improved oxygen surface exchange after theoretical models involving

downscaled microstructure failed to explain the low R_p values they have obtained. They have suggested that the catalytic activity of the small Co_3O_4 precipates in the upper part of their layers have lead to an enhanced oxygen surface exchange. It is possible in the present study that the Co_3O_4 detected by HT-XRD could have contributed to the excellent performance of the infiltrated cathode. However, the existing data is not sufficient to provide support to this claim.

The observed shift in R_s from $T_{max} = 400°C$ to $T_{max} = 900°C$ in Fig. 2.7a may be related to the loss of electronic conduction in the backbone. As evident in Fig. 2.4, increasing the firing temperature causes the LSC particles to coarsen and grow. As the particles coarsen, they lose their connectivity and thus loss of overall percolation is highly likely to happen. This entails an increase in the length of ionic pathway, which is manifested by the increase in R_s. This increase in R_s is more clearly seen at higher temperatures (>600°C) when R_s is plotted as a function of inverse absolute temperature for all LSC firing temperatures as shown in Fig. 2.9b. For all LSC firing temperatures, the measured R_s values are slightly higher compared to the calculated values of resistance from a 180 μm CGO [43]. The slightly higher values of R_s may be attributed to additional contributions including the resistance of parts of the CGO backbone that are not percolated or that the thickness of the CGO electrolyte used was slightly uneven in some places.

2.3.2 Effect of the number of infiltrations

Representative impedance spectra at 400°C and 600°C for different number of infiltrations with LSC and LSC firing temperature are shown in Figs. 2.10a and 2.10b, respectively. The CGO backbone was sintered at 1050°C. The observed variation in R_s at $T_{max} = 400°C$ in Fig. 2.10a and at $T_{max} = 600°C$ in Fig. 2.10b with different number of infiltrations is most likely due to several of the contributions mentioned above. The lowest R_p's were obtained when the LSC was fired at 600°C irrespective of the number of infiltrations. In Fig. 2.10a, the same trends in R_p's as seen in Fig. 2.7a with varying LSC firing temperatures were observed irrespective of the number of infiltrations. This suggests a similarity of mechanisms among these samples. However, there are several other features in the impedance spectra at 400°C in Fig. 2.10a that are worth noting. First, at $T_{max} = 400°C$ the R_p's increase with the number of infiltrations. When the LSC is fired above 400°C, the lowest R_p's were obtained at 9× infiltration except at $T_{max} = 900°C$. Second, the emergence of a separate arc at

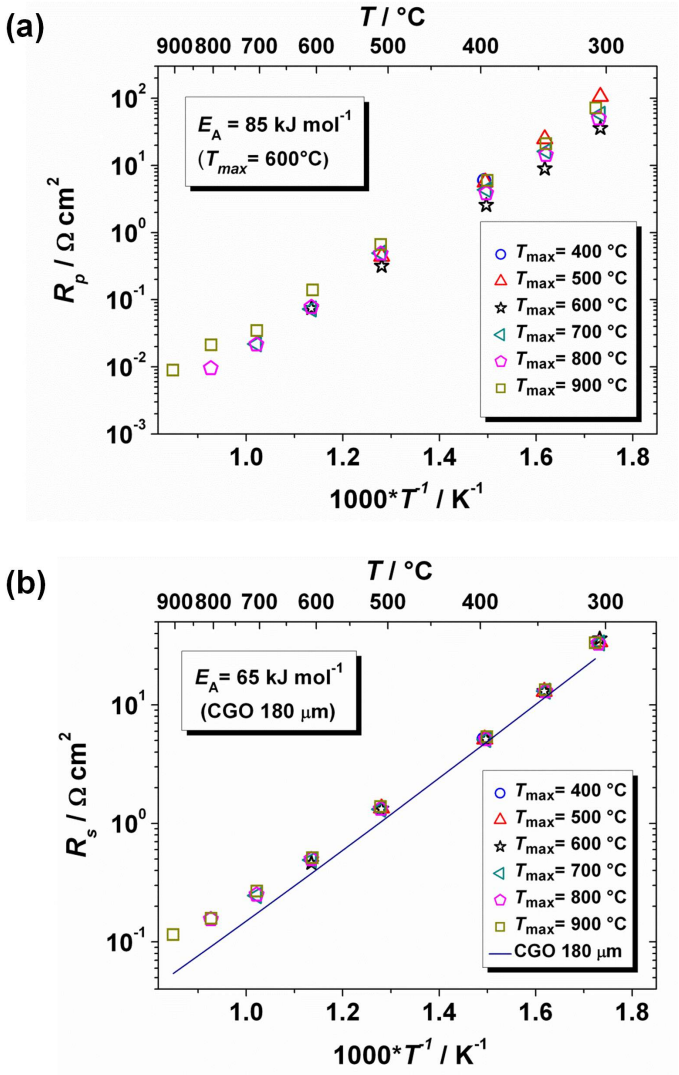

Figure 2.9: (a) Polarization resistance, R_p, and (b) series resistance, R_s, as a function of the reciprocal absolute temperature for different LSC firing temperatures. The straight line in (b) represents the calculated series resistance of a 180 μm CGO electrolyte [43].

low frequency (marked by arrows) is clearly seen for T_{max} = 900°C in both 9× and 12× infiltration. In Fig. 2.10b where the spectra at 600°C were taken, an increase in R_p with increasing firing temperatures were also observed, irrespective of the number of infiltrations. Noticeable changes in R_s are also observed with varying LSC firing temperatures within a certain number of infiltrations. When the sample is infiltrated 6

times, it is seen that R_s increases with LSC firing temperature. Interestingly, this trend is reversed with increased number of infiltration, i.e., R_s decreases with increasing LSC firing temperatures. The decrease is more pronounced when the sample is infiltrated 12 times. These changes in R_s can be explained by the amount of percolating LSC in the backbone. As discussed previously, the shift to higher R_s in the 6× infiltrated sample with increasing LSC firing temperature is brought about by the loss of electronic percolation due to grain growth at higher temperatures. This is not the case in the 9× and 12× infiltrated samples. Since the amount of material is large enough, the loss of percolation in these highly infiltrated samples due to grain growth is not a problem. In fact, as the firing temperature is increased, more LSC particles or particles with high electronic conductivity such as $LaCoO_3$ are formed. This entails a decrease in R_s as observed at 600°C for the 9× and 12× infiltrated samples. The changes in R_s were also observed in subsequent experiments.

The observations in R_p in Fig. 2.10 may be pointing to some other factors that affect the performance of the infiltrated cathodes. What is interesting to note is the slightly higher R_p's obtained for 12× infiltration. If electrode contributions other than the amount of percolated catalysts are disregarded for the moment, this behavior is contrary to what is expected. An increase in the number of infiltration should reduce the total polarization resistance by increasing the surface area of the oxygen reduction catalyst. However, for the case of 12× infiltration it is seen that R_p's have increased. It appears that an additional contribution is becoming more important that it limits the cathode performance. The present data is not sufficient to clearly identify which process(es) is/are involved that increases the R_p of the sample infiltrated 12 times. The observed behavior of increasing R_p at 400°C for $T_{max} = 400$°C is at present not clear. The lowest R_p's are obtained in the 9× infiltrated sample due to relatively larger amount of LSC. The reason for the high R_p's at 400°C (or at 600°C) for $T_{max} = 900$°C in the 9× and 12× infiltrated samples could not be established clearly as it could be an interplay of gas phase transport and microstructure.

The effect of the number of LSC infiltrations on R_p, R_s, and R_{total} is summarized in Fig. 2.11. Increasing the amount of infiltrated LSC decreased R_p until up to 9 times infiltration for CGO backbones sintered at 1050°C and LSC maximum firing of 600°C. Subsequent infiltrations made the R_p slightly higher. Meanwhile, there was no clear trend observed in R_s with the number of infiltrations owing to the varied contributions described previously.

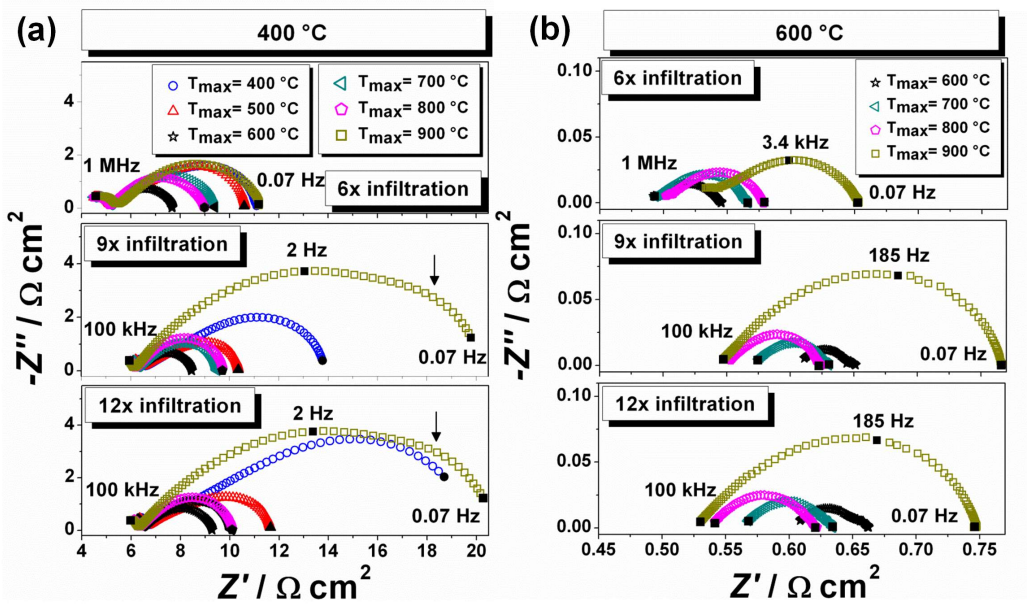

Figure 2.10: Representative complex plane plots (a) at 400°C and (b) 600°C versus the number of LSC infiltration and LSC firing temperature. The CGO backbone was fired at 1050°C. The emerging low frequency arc at 400°C for $T_{\max} = 900$°C in the 9× and 12× infiltrated sample in (a) are marked by arrows. The lowest and highest frequency data points (solid markers) correspond to 0.07 Hz and 1 Mhz (or 100 kHz in 9× and 12× infiltrated samples), respectively.

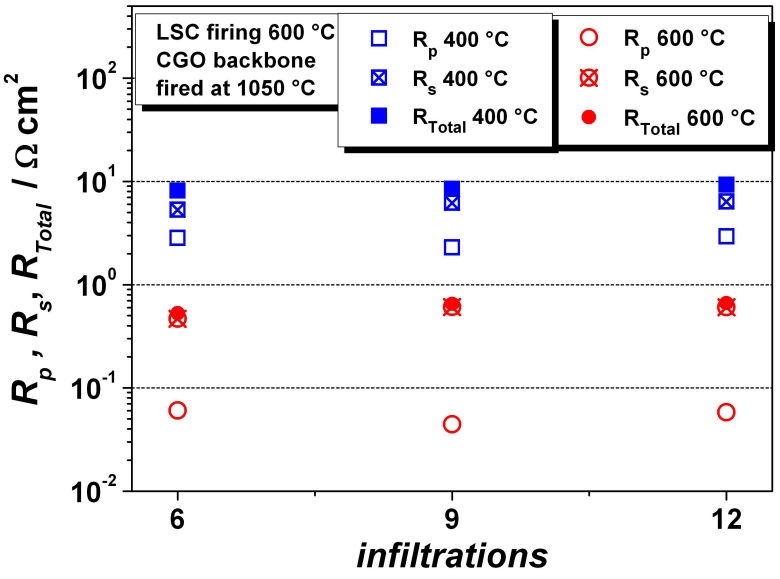

Figure 2.11: Cathode polarization resistance (R_{p}), series resistance (R_{s}) and total resistance (R_{total}) at 400°C and 600°C versus the number of infiltrations. The LSC particles were fired at 600°C. The CGO backbone was fired at 1050°C.

2.3.3 Effect of the CGO backbone firing

Complex plane plots of LSC infiltrated CGO backbone fired at 1150°C (not shown) revealed the same trends in R_{p} and R_{s} at 400°C and 600°C in all firing temperatures and number of infiltrations. This highlights the reproducibility of the method. The major difference using a CGO backbone fired at 1150°C is that overall R_{p}'s are slightly higher than what is obtained when a CGO backbone fired at 1050°C is used. This indicates that the CGO backbone firing temperature is another important factor which affects the performance of the infiltrated cathode.

Fig. 2.12 summarizes the effect of varying the CGO backbone firing temperature on R_{p}, R_{s}, R_{total} of the sample. The sample was infiltrated 6 times with LSC and was fired at 600°C. Like the trend in R_s values in Fig. 2.11, the differences in R_s with CGO backbone firing temperature cannot be explained unambiguously. The large value of R_{s} is due to the 180 μm thick electrolyte tape. The CGO backbones fired at 1050°C yielded the lowest R_{p} values at 400°C. The reason again has got to do with the compromise between microstructure and connectivity of the CGO particles. The finer and well connected backbone is preferred. Although a well-connected and well-sintered mi-

crostructure may result from CGO backbone firing temperature as high as 1250°C, it is expected that it would also produce coarser grains compared to that of CGO backbone fired at lower temperatures. The average grain size difference is confirmed by examining polished cross section of the CGO backbones fired at different temperatures which are shown in the SEM micrographs in Fig. 2.1. Identical results were seen by Shah and Barnett [59] in their work on LSCF infiltrated CGO backbones. While the increase in CGO grain size is obvious with increasing firing temperature, the connectivity and how well sintered the backbones are, are not immediately obvious. Differentiating the microstructures accurately in this case would require more appropriate techniques like focused ion beam (FIB) tomography [79]. In this study, it seems that firing the CGO backbone to a temperature of 1050°C produces finer yet sufficiently connected and sintered microstructure best suited for use as a backbone for infiltration.

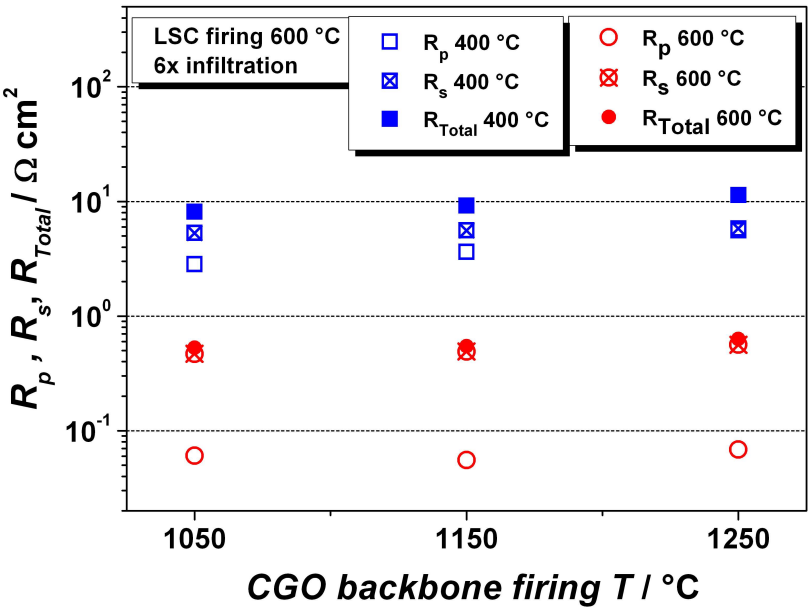

Figure 2.12: Cathode polarization resistance (R_{p}), Series resistance (R_{s}) and total resistance (R_{total}) at 400°C and 600°C versus CGO backbone firing temperature. The LSC was fired at 600°C.

The lowest R_{p} value obtained in this study was 0.044 Ω cm^2 and 2.3 Ω cm^2 at 600°C and 400°C, respectively when the number of LSC infiltrations was 9 times and fired at 600°C and the CGO backbone had been fired at 1050°C. The R_{p} value, particularly at 600°C where most intermediate temperature cathodes are of interest is exceptionally low in this study. At 600°C, the polarization resistance of a LSC in-

filtrated $Sm_{0.2}Ce_{0.8}O_{1.9}$ (SDC) cathode [61] was 0.29 - 0.31 Ω cm^2. By infiltrating $La_{0.6}Sr_{0.4}Co_{0.2}Fe_{0.8}O_{3-\delta}$ (LSCF) into porous CGO, Shah and Barnett [59] measured an electrode polarization resistance of 0.24 Ω cm^2, significantly higher than the present cathodes. It is important to note that the infiltrated cathode had a higher R_p at 600°C than the nanoporous $La_{0.6}Sr_{0.4}CoO_{3-\delta}$ thin films (150 - 200 nm) prepared by dip coating. The R_p was 0.023 Ω cm^2 at 600°C for the $La_{0.6}Sr_{0.4}CoO_{3-\delta}$ thin film using CGO as electrolyte [54]. However, significant degradation of performance reaching 0.069 Ω cm^2 at 600°C occurs after 100 h of annealing at 700°C. The activation energy and long term study at 600°C for this thin film was also not reported. The R_p obtained from the present study is also slightly higher at 600°C than the nanoporous $La_{0.25}Ba_{0.25}Sr_{0.5}Co_{0.2}Fe_{0.8}O_{3-\delta}$ (LBSCF) thin film (≤ 1 μm) prepared by spray pyrolysis. Using YSZ as electrolyte, they reported an R_p of 0.038 Ω cm^2 at 600°C for this material [55]. However, the activation energy of these LBSCF thin films was significantly higher than the LSC infiltrated cathode. The activation energy was 128 kJ mol^{-1} for the LBSCF thin film compared to only 85 kJ mol^{-1} of the LSC infiltrated cathode studied here. Furthermore, no report on degradation was given on the LBSCF thin film study. This suggests better applicability of the infiltrated cathode for SOFCs operating below 500°C. The differences of R_p's and activation energies could of course be attributed to the differences in processing conditions and different materials properties. A small degradation study on the infiltrated cathodes is discussed in the following.

2.3.4 Cathode degradation studies

Degradation studies of the infiltrated electrodes were also done and are shown in Fig. 2.13. The sample that was fired at 900°C and tested for 100 h at 600°C levels out after a short time (Fig. 2.13a). For the sample where the LSC was fired at 600°C, it was observed that it takes longer time to reach an apparent stable value of R_p (Fig. 2.13b). In both cases, a total degradation of ~ 0.03 Ω cm^2 was observed before reaching their apparent asymptotic value. Judging from Fig. 2.13, the values may increase but only slightly. It is evident that it takes relatively longer time for the electrode fired at a maximum temperature of 600°C to reach an apparent stable value. The more likely explanation would be that the equilibrium particle size for this temperature has not been reached yet and takes longer time to achieve. This explanation is supported by examining the resulting microstructure in SEM of the fracture surface of the sample after testing at 450 h. This is shown in Fig. 2.14. The CGO grain is marked by an

arrow. Clearly the LSC grains have grown much larger than the one shown in Fig. 2.4c ($T_{max} = 600°C$). The LSC microstructure and particle sizes closely resemble that of the SEM image in Fig. 2.4d, or the one fired at 700°C. It remains to be seen whether grain growth would continue had it been tested for even longer time. Extended degradation studies are needed to clarify this. Examination of the microstructure of the symmetrical cell tested for 100 h ($T_{max} = 900°C$) seems to have no difference with the one shown in Fig. 2.4f, or the one fired at 900°C. The R_s in both samples slightly increases in the beginning but reaches a stable value as expected. The slightly higher R_s value observed for the sample fired at 900°C might be due to either the loss of electrical conductivity by connectivity loss of LSC particles via grain coarsening as discussed previously.

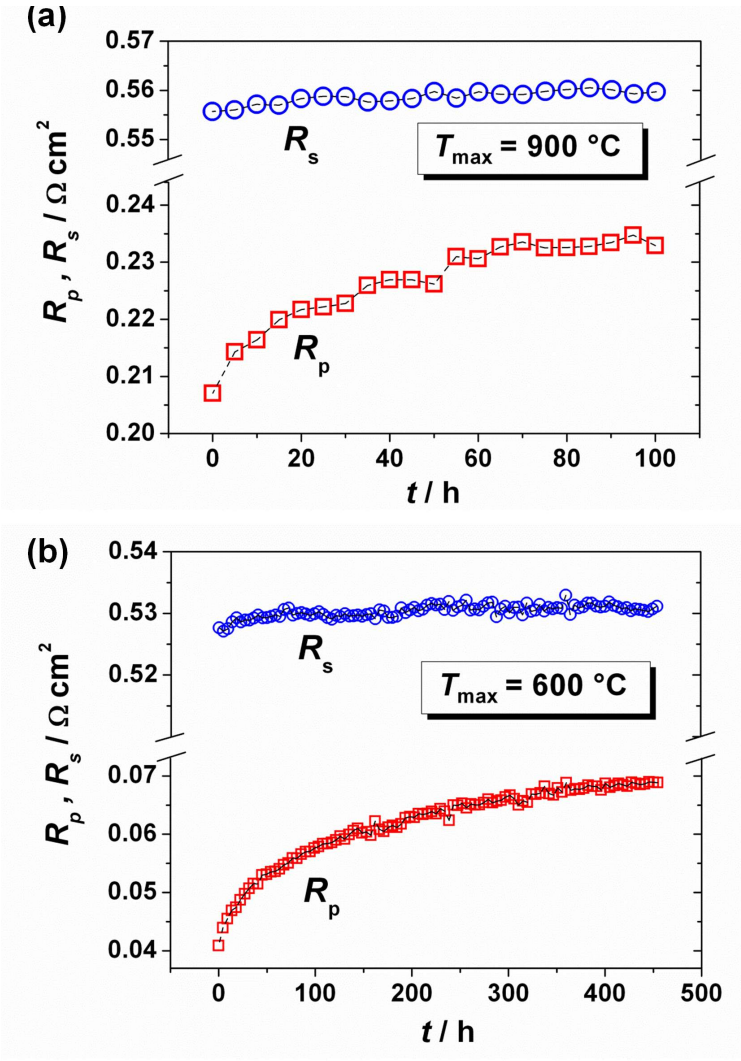

Figure 2.13: Degradation data for R_p and R_s during 100 h testing at 600°C after the LSC had been fired at 900°C (a) and (b) during 450 h testing at 600°C after the LSC had been fired at 600°C. The sample had been infiltrated 6 times. Data were collected every 4.5 h. Lines are guide to the eye.

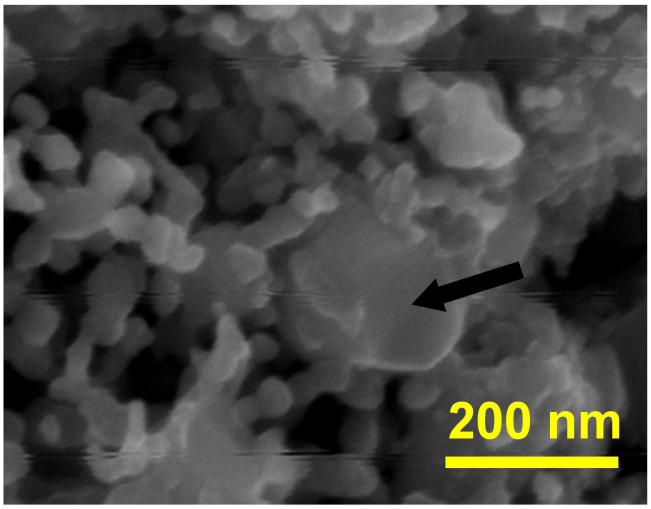

Figure 2.14: SEM micrograph of the LSC infiltrated CGO backbone after 450 h testing at 600°C after the LSC had been fired at 600°C. A CGO grain is marked by arrow.

2.4 Summary

High performance cathodes were fabricated by infiltration of LSC into CGO backbones. An optimum firing temperature of the LSC infiltrate was found to be at 600°C. It is found that at this temperature, a balance between nano-scaled microstructure and catalyst formation was reached. Other processing conditions including CGO firing temperature and LSC loading were also found to be important to achieve a high performance cathode. The lowest polarization resistances measured at 600 and 400°C were 0.044 and 2.3 Ω cm^2 in air, respectively and the activation energy was 85 kJ mol^{-1}. HT-XRD revealed the formation and decomposition of component oxides and secondary phases with infiltrate firing temperature highlighting the complexity of the material when employed with the infiltration method. At the optimal firing temperature of 600°C, a mixture of phases instead of phase pure LSC was obtained. The polarization resistance decreased with increased LSC loading up to 9$\times$ infiltration, or about 17 vol %. Subsequent infiltrations make the performance slightly worse. The results indicate the possibility of controlling separately the CGO backbone firing, LSC

loading, and most importantly the LSC firing to achieve exceptionally low polarization resistances. Degradation studies indicate stability up to 450 h suggesting reliability of the cathode for use in low temperature SOFCs.

Chapter 3

$LaCoO_3$ and Co_3O_4 infiltrated - CGO cathodes[†]

3.1 Introduction

Infiltration with doped $LaCoO_3$, specifically $La_{0.6}Sr_{0.4}Co_{0.2}Fe_{0.8}O_{3-\delta}$ (LSCF) [59] and $La_{0.6}Sr_{0.4}CoO_{3-\delta}$ (LSC) [61] has been widely popular in recent years. The role of strontium ions in these structures is to increase the electronic conductivity at lower temperatures, whereas at higher temperatures (>800°C) both Sr-doped and undoped $LaCoO_3$ has high and comparable electronic conductivity [80]. In addition, by substituting with Sr, oxygen vacancies are formed at lower temperatures. The increase in the concentration of vacancies leads to significant ionic conductivity and is also often linked with a high catalytic activity [81, 82]. Large particles of $LaCoO_3$ is therefore not believed to have a significant ionic conductance, nor oxygen reduction capabilities at the target operating temperature range of 500 - 700°C of the so-called intermediate temperature-SOFCs and should therefore only possess oxygen reduction capabilities close to the triple phase boundary (TPB) defined by the electrolyte/electrolyte particles, electrocatalyst, and the gas phase. Reducing the oxygen reduction reaction to only the vicinity of the TPB is generally believed to be associated with a significant increase in the cathode polarization resistance.

[†]Parts of this chapter has been published as A. J. Samson, M. Søgaard, and N. Bonanos,"Electrodes for solid oxide fuel cells based on infiltration of Co-based materials", *Electrochem. Solid State Lett.*, 15 (2012) B54-B56.

The excellent catalytic and transport properties of the Sr-doped materials are perceived to be maximized when these materials are formed as nanoparticles such as in the case of infiltration. Indeed, low electrode polarization resistances are obtained by infiltrating LSCF [59] into $Ce_{0.9}Gd_{0.1}O_{1.95}$ (CGO) (0.24 Ω cm^2 at 600°C) and LSC [61] into $Ce_{0.8}Sm_{0.2}O_{1.9}$ (SDC) (0.29 - 0.31 Ω cm^2 at 600°C). It has been demonstrated in Chapter 2 that excellent performance on "LSC" infiltrated - CGO cathodes (0.044 Ω cm^2 at 600°C) can be obtained even though the infiltrated material was not phase pure LSC at the optimum firing temperature of 600°C. The presence of $LaCoO_3$, $SrCO_3$ and Co_3O_4 and other phases was clearly evident in the high temperature X-ray diffraction (Fig. 2.3). Thus, it was not possible to discount that $LaCoO_3$ together with other phases, had contributed significantly to the electrochemical performance. This raises significant questions on the composition of the actual electrocatalyst, the way that these infiltrated nanoparticles act in SOFC cathodes and the role of Sr when LSC is introduced by infiltration. In past studies, the degradation of the cathode performance is almost always linked to the presence of Sr [83, 84, 85, 86]. It might, therefore, be expected that a Sr-free electrocatalyst could lead to cathodes with a higher stability under SOFC operating conditions.

In this chapter, the feasibility of employing undoped $LaCoO_3$ infiltrated into a CGO backbone as a cathode for SOFCs in the form of the constituent nitrates is investigated. Pure cobalt oxide, Co_3O_4, was also studied for comparison. Testing the electrochemical performance of Co_3O_4-containing cathode is also of great interest since there appears to be some discrepancies with regards to the performance of cobalt oxide-infiltrated cathodes. Yamahara et al. [87] and Imanishi et al. [88] reported significant improvements in cell performance when their cathodes, which consist of Sr-doped $LaMnO_3$ (LSM) - scandia doped yttria stabilized zirconia (ScYSZ) and LSM-YSZ, respectively, were infiltrated with cobalt oxide. On the contrary, Huang et al. [89] reported no enhancement in cell performance when CoO_x was added to a LSM-YSZ cathode. It is not difficult to see, however, that the discrepancies in these studies are most likely due to the differences in the formation of well-dispersed and percolated particles of Co_3O_4, brought about by the difference in the Co_3O_4 loading and firing temperatures, within the LSM-YSZ porous structure, especially in the region of the TPBs. By testing pure Co_3O_4 infiltrate in a CGO backbone in a symmetric cell configuration, more insight is gained on the electrocatalytic activity of Co_3O_4. Electrochemical impedance spectroscopy was employed to measure the electrochemical performance of the infiltrated cathodes. The resulting micro/nano-structures of the infiltrated cathodes were analyzed by scanning

electron microscopy. Based on previous studies [80, 90, 91], the electronic conductivity of the bulk materials can be arranged as LSC>LC>Co_3O_4, noting that the electronic conductivity of LSC is several orders of magnitude higher than that of Co_3O_4. To put it into perspective, the electronic conductivities of these materials at 600°C in air are approximately 2000 [90], 600 [80], and 2 [91] S cm^{-1} for LSC, LC, and Co_3O_4, respectively. Of these materials, LSC has a significant ionic conductivity at SOFC operating temperatures with typical values in the range 0.01 - 0.45 S cm^{-1} at temperatures 650 - 1000°C [92].

3.2 Experimental

The preparation of the backbones and the infiltration procedure has been outlined in Chapter 2. Precise amounts of nitrates are mixed to obtain the nominal compositions Co_3O_4, $LaCoO_3$ (LC), and $La_{0.6}Sr_{0.4}Co_{1.05}O_{3-\delta}$ (LSC). The number of infiltrations was fixed to six times. A precalcination step at 350°C for 1 hour was performed after each infiltration cycle. To estimate the amount of loading for each infiltrate, the weights of the samples were measured before and after the desired number of infiltrations. Considering that the desired infiltrates are not yet formed at 350°C, the measured weights were corrected for the relative weight loss associated with the formation of the corresponding compounds from dried infiltrate powders heated to 350°C. The relative weight loss, obtained by thermogravimetric analysis, after formation of seemingly stable LC and LSC compounds at 1000°C are 9.5 and 20 %, respectively. For Co_3O_4, the weight loss is 2.5 % after heating at 650°C. Assuming complete formation, infiltrating six times with Co_3O_4, LC, and LSC yields approximately 18, 14, and 12 vol % out of the total volume of one cathode side, respectively.

The cells are heated in situ in the electrochemical set up as described in Chapter 2, to a maximum of 600°C in air. As also discussed in Chapter 2, this temperature was found to be optimum for "LSC"' in terms of catalyst material formation and high surface area nanostructure. Electrochemical impedance spectroscopy at temperatures between 600 and 300°C was performed using a Hioki 3522-50 impedance analyzer in the frequency range from 0.1 Hz to 100 kHz under open circuit conditions with 50 mV amplitude AC signal. Microstructures of the infiltrated materials as well as the backbone structure were characterized using a Zeiss Supra 35 scanning electron microscope. X-ray diffraction (XRD) was performed on the infiltrate powders using a Bruker D8 Bragg - Brentano diffractometer with Cu Kα radiation in order to identify the phases

formed. These infiltrate powders were prepared by drying the corresponding precursor solution and heating to 600°C for 2 h in air.

3.3 Results and Discussion

The XRD patterns of the infiltrate materials are shown in Fig. 3.1. All the infiltrate powders are multi-phase except for the Co infiltrate (Fig. 3.1a) where it is found to be phase pure within the XRD detection limit and all the peaks can be indexed based on the JCPDS card of Co_3O_4 (PDF no. 00-043-1003). The multi-phase infiltrates (Fig. 3.1b and 3.1c) will hereafter be called according to their parent phase (precursor solution stoichiometry) namely "LC" and "LSC", even though they are composed of several phases. Notable in both the LC and LSC infiltrates is the presence of Co_3O_4. In addition, carbonate formation is prevalent in LSC but also found for LC. In the case of LSC, the dominant phase(s) appear to be a mixture of Sr- substituted lanthanum cobalt oxide phases. The dominant phase for LC is $LaCoO_3$ (PDF no. 00-048-0123). The formation of several secondary phases in the studied materials is conceivable considering the different thermal decomposition of the precursors. Apparently, the multiphase feature and the presence of carbonates in the infiltrates do not restrict the electrochemical performance of the infiltrated cathodes as discussed later.

Shown in Fig. 3.2 are SEM micrographs of fractured cross sections of the infiltrated cathodes that have been fired at 600°C for 2 h. The CGO particles are seen as interconnected grains of about 200 nm in diameter while the infiltrated materials are seen as a network of particles partially covering the CGO grains. The cobalt oxide particles (Fig. 3.2a) appear to be the largest particles (about 50 nm) of the three infiltrates. The microstructure of LC (Fig. 3.2b) is much like that of LSC (Fig. 3.2c), and the particle sizes for these two infiltrates are the same within the uncertainty (30-40 nm).

The complex plane plots of the infiltrated cells at 600°C in air are shown in Fig. 3.3. For easy comparison, the complex plane plots of infiltrated Co_3O_4 and LC cells have been shifted such that the real part of their impedance (Z') for the frequency 100 kHz coincides with the initial Z' value of the LSC infiltrated cell. The high frequency intercept or serial resistance (R_s) is discussed later. The area specific cathode polarization resistance (R_p) is defined here as the difference between the real part intercepts in the high and low frequency data points. From Fig. 3.3, it is seen that the highest R_p is obtained for the pure cobalt infiltrated cathode (0.27 Ω cm^2). It is also seen that

the values for LC (0.079 Ω cm^2) and LSC (0.062 Ω cm^2) are rather close. The R_p value (0.079 Ω cm^2) of the LC infiltrated sample is very low and within the range of values of LSC. Although LC has intrinsic p-type conductivity, the nonstoichiometry value, δ, in bulk LC which is often associated to oxide ion diffusivity and catalytic activity, is essentially undetectable at temperatures below 800°C [82].

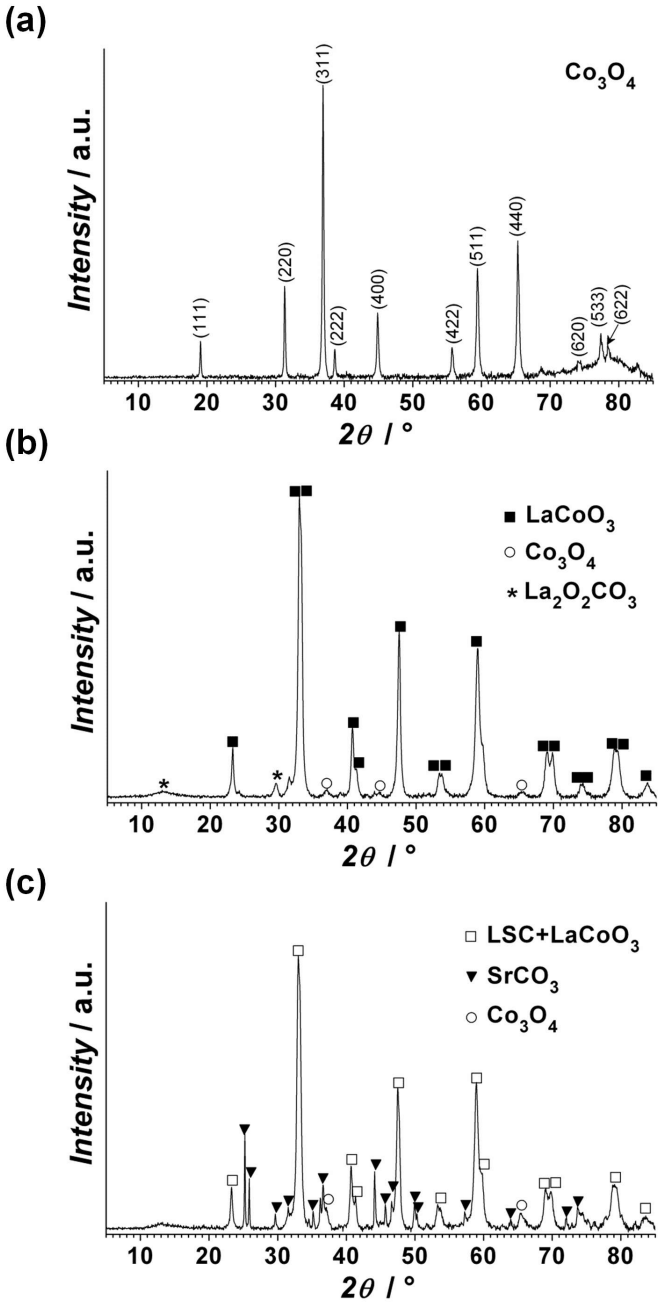

Figure 3.1: XRD patterns for the different infiltrates. (a) Co_3O_4 (b) "LC" and (b)"LSC"

Another interesting finding is the performance of the pure Co infiltrated cell. The

R_p value of 0.27 Ω cm^2 is comparable to the reported R_p values of LSCF [59] infiltrated - CGO and LSC [61] infiltrated - SDC cathodes. The performance of the Co_3O_4 infiltrated electrode can be compared to that of a non-infiltrated symmetric cell painted with the same Pt paste current collector used in testing the infiltrated cathodes. It can be confirmed by looking at the impedance spectra shown in the Appendix A that the performance of the Pt paste/CGO backbone cathode is greatly inferior to that of the Co_3O_4-infiltrated cathode. In principle, it could be speculated that CGO in the backbone may act as an oxygen reduction catalyst, however, tracer diffusion experiments [32, 93, 94] indicate a low surface exchange coefficient, therefore this is not considered likely. Thus, it appears that a reasonable performance even by using only Co infiltrate can be attained by the infiltration method. The result also supports the idea that the Pt paste/non-infiltrated CGO backbone cathode is less likely to perform well as a cathode. It is interesting to note that in previous studies [88, 95], performance enhancements were observed when LSM-YSZ composite cathodes were infiltrated with Co_3O_4. Also, in the recent study by Dieterle et al. [54] on LSC thin films, it was speculated that the catalytic activity of nano-scale Co_3O_4 precipitates in the cathode lead to an enhanced oxygen surface exchange consistent with the findings in this study. The R_p of all the infiltrated samples as a function of the reciprocal absolute temperature are shown in Fig. 3.4. It is seen that the activation energy for the Co_3O_4 infiltrated cathode is lower than that for LC and LSC, respectively. Very small differences are observed between the R_p values of LC and LSC.

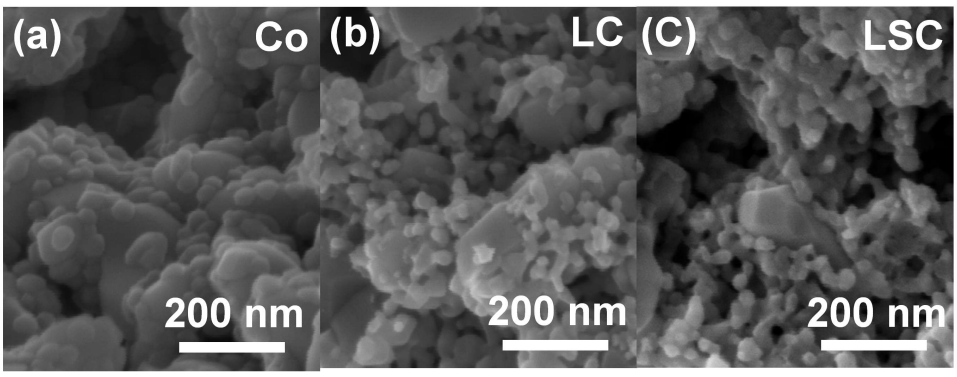

Figure 3.2: SEM micrographs of fractured cross sections of (a) Co_3O_4, (b) LC, and (c) LSC infiltrated - CGO cathodes fired at 600°C for 2 h in air.

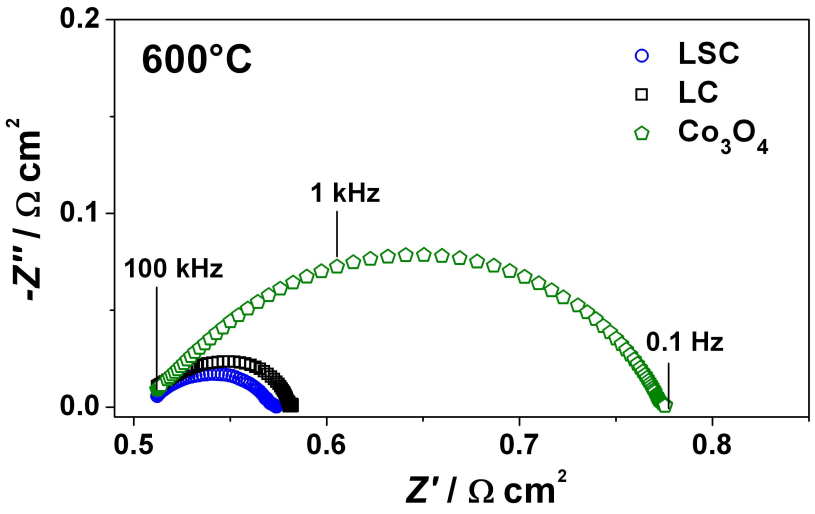

Figure 3.3: Complex plane plots of all the infiltrated cells at 600°C in air. The lowest frequency data points correspond to 0.1 Hz.

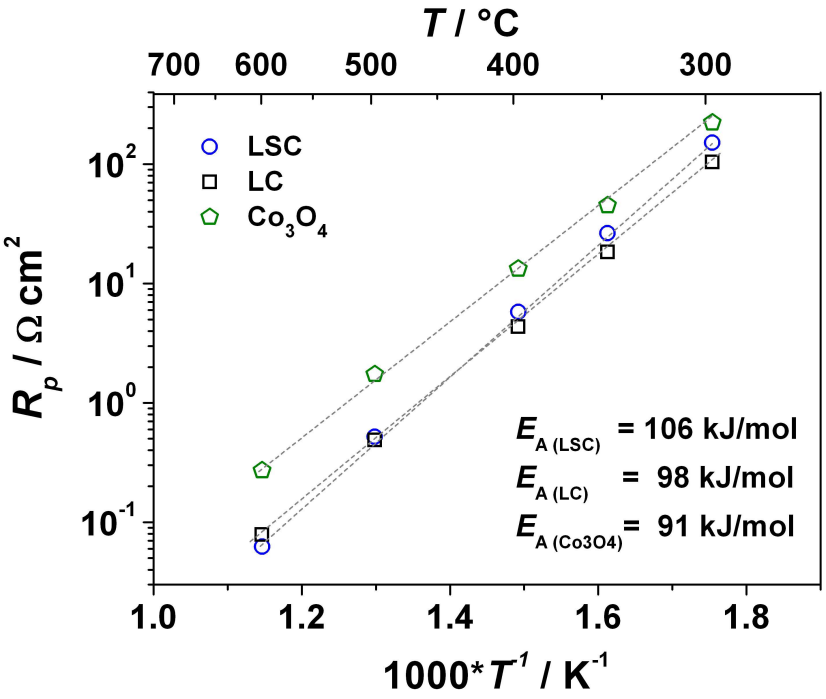

Figure 3.4: Polarization resistance, R_{p}, as a function of the reciprocal absolute temperature and the corresponding activation energies (E_{A}) for all the infiltrated cells tested in air.

A concern, especially for the Co_3O_4 infiltrate is its low electronic conductivity (2 S cm^{-1} at 600°C [91]). To provide an idea on the ohmic losses in each of the infiltrated cathodes, the R_{s} based on impedance spectra of each of the infiltrated cathodes are compared. It is found that R_{s} at 600°C for all the electrodes are comparable (0.5 - 0.6 Ω cm^2) within the uncertainty. These values are slightly higher than the calculated series resistance of the 180 μm CGO electrolyte [43] used in the study (0.41 Ω cm^2). This is reflected in Fig. 3.5 which shows a plot of R_{s} for all the cathodes as function of the reciprocal absolute temperature. This suggests that the electronic conductivity and the connectivity of all the infiltrates were sufficient to not have significant ohmic losses. It should also be remembered that the Pt paste used in this study as a current collector ensures that the resistance due to the in-plane conductance of the infiltrated cathode is maintained at a minimum.

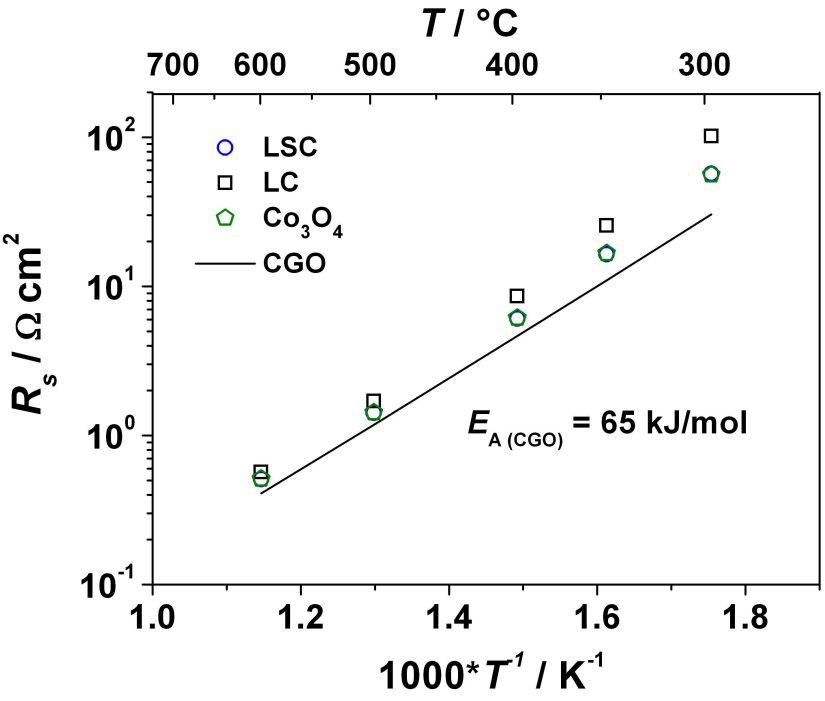

Figure 3.5: Serial resistance, R_s, as a function of the reciprocal absolute temperature. The straight line corresponds to the calculated series resistance of a 180 μm CGO electrolyte [43].

From the electrochemical and morphological results, it appears that the surface exchange properties of the materials played an important role on their electrochemical performance. This is especially true for LC infiltration where an almost comparable performance with the LSC infiltrated cathode is seen. Based on an almost comparable amount of loading and microstructure in the LC and LSC infiltrated cathode, it is reasonable to conclude that in the case of LC, its surface exchange properties allowed efficient oxygen surface exchange, even without Sr doping. Also, due to the small particle sizes, it is clear that even a very low ionic conductivity of the infiltrate will ensure that they work as a MIEC. Specifically, it is probably not unrealistic that the nano-sized LC has sufficient ionic conductivity to work as a MIEC, but the high oxygen exchange rates of the infiltrate is surprising. The extent of the influence of Co_3O_4 in the surface exchange properties of Co-containing infiltrates is still an open question and requires in depth studies. It is not unlikely that part of the electrode performance of both the LC and LSC in reality originates from nano-crystalline cobalt oxide. Using

undoped $LaCoO_3$ has some advantages as one does not risk the formation of carbonates from the dopants which could possibly enhance the long term stability of the infiltrated cathode.

3.4 Summary

The electrochemical performance of cobalt-based infiltrated cathodes was investigated. A very low electrode polarization resistance (0.079 Ω cm^2) at 600°C in air was obtained for a $LaCoO_3$ cathode prepared using the infiltration method. This value is comparable to that for a cathode prepared by infiltrating the nitrates corresponding to Sr-doped $LaCoO_3$. Good performance was obtained even for cathodes infiltrated with Co_3O_4 only (0.27 Ω cm^2). The high performance of the undoped $LaCoO_3$- and Co_3O_4-infiltrated cathodes are attributed to the enhanced surface exchange and hence, oxygen reduction properties of these materials at the nanoscale.

Chapter 4

LSC infiltrated - BICUVOX and BICUVOX-CGO cathodes[†]

4.1 Introduction

The compound $Bi_2V_{0.9}Cu_{0.1}O_{5.35}$ (BICUVOX) exhibits oxide ion conductivity about two orders of magnitude higher than that of other oxide ion conductors at temperatures below 500°C [38]. In a solid oxide fuel cell cathode where high ionic conductivity, high catalytic activity and high electronic conductivity are essential, it should be possible to use BICUVOX as the oxide ion conducting component in a composite cathode. Xia and Liu [44] have demonstrated this possibility by using silver as the electronic conducting phase to form a Ag (57 wt%) - BICUVOX composite cathode and showed remarkable performance at low temperatures (e.g. 0.53 Ω cm^2 at 500°C). Recently, a Ag - BICUVOX composite cathode has also been evaluated in a single chamber solid oxide fuel cell and showed promising characteristics such as low activity for propane chemical oxidation and good stability under relatively high propane partial pressures [39]. However, it was also shown that fuel cell operation was limited to furnace temperatures below 600°C as BICUVOX undergoes extensive sintering and loss of porosity [39]. In addition, detrimental reactions between the cathode and the samaria doped-ceria electrolyte occurs above 650°C [39]. Clearly, the use of BICUVOX in SOFC composite cathodes holds great promise if proper materials are selected and if the operating or

[†]Parts of this chapter has been published as A. J. Samson, M. Søgaard, and N. Bonanos,"Electrochemical characterization of infiltrated $Bi_2V_{0.9}Cu_{0.1}O_{5.35}$ cathodes for use in low temperature solid oxide fuel cells", *Solid State Ionics*, (2012) in press.

processing temperature is low enough to prevent structural degradation and reactivity with other cell components.

In the in the preceeding chapters, it has been shown that low calcination temperatures are needed to obtain effective $LaCoO_3$-based electrocatalysts. It is hypothesized that this low calcination temperatures involved in the infiltration method should minimize the unwanted reactions between the infiltrated material and the porous BICUVOX backbone. In this respect, it should be possible to prepare composites of BICUVOX and materials that have poor chemical compatibility with it, such as cobaltites.

Sr-substituted lanthanum cobaltites (LSC) is seen as one of the most promising materials for cathodes for solid oxide fuel cells due to its high electronic and oxygen ionic conductivity and good catalytic activity for oxygen reduction. To obtain a composite of these materials and bismuth - based oxides such as BICUVOX which possess very high oxygen ionic conductivity seems to be a very promising proposition for solid oxide fuel cell applications. The thermal expansion coefficients of the two materials can be matched by appropriate cation substitution and composition adjustment, e. g. by using $La_{0.8}Sr_{0.2}Co_{0.2}Fe_{0.8}O_{3-\delta}$ (LSCF, TEC $\sim 14.8 \times 10^{-6}$ K^{-1} [90]) instead of $La_{0.6}Sr_{0.4}CoO_{3-\delta}$ (LSC, TEC 20.5×10^{-6} K^{-1} [90]) to match BICUVOX (TEC $\sim 15 \times 10^{-6}$ K^{-1} [96]). However, it is known that interdiffusion of elements in the interface of cobaltite and Bi_2O_3-based materials is prevalent especially during processing at elevated temperatures ($> 750°C$), producing phases with inferior electronic/ionic conductivity and electrochemical activity [90]. Thus, to be able to employ these two materials, a processing temperature low enough to minimize or prevent the interaction of the two materials is necessary.

Another material that could potentially be used together with BICUVOX or bismuth-based materials in general, is doped-ceria. In terms of thermal expansion, the TEC of the two materials are rather close (BICUVOX TEC $\sim 15 \times 10^{-6}$ K^{-1} [96] and $Ce_{0.9}Gd_{0.1}O_{1.95}$ CGO TEC $\sim 12.5 \times 10^{-6}$ K^{-1} [97]). Thus, a contact between the two materials is expected to be mechanically robust up to a certain operating temperature. Several researchers have demonstrated good cathode performances using doped-ceria electrolytes in contact with bismuth-based materials [44, 39, 98, 99] and reported no compatibility issues when the operating temperature is below 650°C. However, above this temperature, it has been shown that detrimental reactions producing low ionic conductivity phases between a bismuth - based material containing - cathode and a doped ceria electrolyte occur [39]. In this chapter, a BICUVOX-CGO composite backbone is

prepared that may potentially enhance the contact between this composite backbone and the CGO electrolyte.

The goal is to prepare cathodes, employing infiltration as a low temperature processing method to introduce LSC into porous BICUVOX or BICUVOX-CGO composite backbones. By using infiltration, this study intends to stretch the limits of materials processing to combine BICUVOX and LSC - materials that are known to react at elevated processing and operating temperatures. LSC firing temperatures lower than 600°C were employed. It has been shown in Chapter 2 that introducing LSC into a CGO backbone and firing at 600°C produces the lowest cathode polarization resistances, R_p (e.g. 0.044 Ω cm^2 at 600°C) compared to those fired above 600°C. Interestingly, the infiltrate formed at this low firing temperature is multi-phased, which includes secondary phases such as $LaCoO_3$, Co_3O_4, and even $SrCO_3$. The low temperature firing should minimize or prevent unwanted reactions between the BICUVOX/BICUVOX-CGO backbone and the LSC infiltrate. Theoretically, the replacement of CGO with a much higher ionic conductivity material such as BICUVOX should result in a cathode with a significantly higher performance as the electrode reaction can spread out into the structure.

4.2 Experimental

The BICUVOX powder was prepared using conventional solid-state reaction method. Precise amounts of Bi_2O_3 (99.8%, Johnson Matthey, Germany) V_2O_5 (99.6%, Alfa Aesar, Germany) and CuO (99.7% Alfa Aesar, Germany) were mixed with ethanol and milled using zirconia balls for 24 h. After drying, the mixture was fired at 800°C in an alumina crucible for 8 h in air. To ensure complete reaction, the powder was ground and refired at 800°C for 4 h and then characterized using a Bruker D8 Bragg-Brentano diffractometer with Cu Kα radiation. Pellets for electrical conductivity measurements were formed by first, uniaxially cold pressing 2 g of the BICUVOX powder to a load of 1.2×10^8 Pa and then isostatically pressing to a load of 5.1×10^9 Pa. The pellets were subsequently sintered in air at 800°C for 20 h. Conductivity measurements were performed using an AC four wire two electrode impedance measurement technique using a Solarton 1260 impedance analyzer in the frequency range 0.01 Hz to 1 MHz with a 50 mV amplitude AC signal with no DC bias. Pt paste (Ferro GmbH, Germany) was painted on both sides of the pellet to act as electrodes and current collector. Impedance spectra were recorded during heating from 290 to 650°C and cooling from 650 to 290°C

at 10-50°C intervals. The measured conductivities were significantly higher than that of CGO in the range of temperatures studied. For instance, the conductivity at 500°C is about 0.057 S cm^{-1} which is about 7 times higher than CGO at this temperature (0.0079 S cm^{-1}) [43].

To prepare the backbones, pure BICUVOX and BICUVOX - CGO (Rhodia) (50 vol%) inks were screen printed onto both sides of a 5 × 5 cm^2, dense 180 μm thick CGO electrolyte (KERAFOL). The screen printed samples with pure BICUVOX were fired at 600, 700, and 800°C in air for 2 h to study the resulting microstructure of the backbone and the adhesion to the CGO electrolyte. It was found that firing below 800°C resulted in a powdery material with very poor adhesion to the dense CGO electrolyte such that the only available backbones for infiltration were those fired at 800°C. The samples with the BICUVOX - CGO composite were fired at 850°C in air for 2 h. All the backbones have thickness of approximately 20 μm. The symmetric cells were cut in squares with an approximate size of 6 × 6 mm^2 and used for LSC infiltration and subsequently, impedance measurements.

The procedure for preparing the LSC precursor solution and the infiltration method has already been outlined in Chapter 2. The backbones were infiltrated 6 times with LSC. The amount of infiltrated LSC is about 5 vol% out of the total volume of the electrode assuming complete formation of LSC. The procedure for estimating the amount of LSC is also described in Chapter 2. To investigate the performance with varying infiltrate firing temperature, the infiltrated cathodes were heated in-situ in an electrochemical setup at temperatures ranging from 350-600°C at 25 to 100°C intervals. The samples were heated for different maximum temperatures, T_{max}, starting from 400, 500, and finally 600°C, taking impedance measurements of temperatures in between. The heating profile is similar to that used in Chapter 2, only that the highest temperature in this case is 600°C. This is done in the hope of avoiding unwanted reactions from the infiltrated materials and the BICUVOX backbone. Further, the firing temperature of $T_{max} = 600$°C for LSC was, from Chapter 2 shown to produce the lowest area specific resistance in the infiltrated CGO backbones.

Microstructures of the infiltrated LSC as well as the backbone structures were characterized using a Zeiss Supra 35 scanning electron microscope. In-situ high temperature X-ray diffraction (HT-XRD) in air was performed on the BICUVOX-LSC powder mixture using a Bruker D8 Bragg-Brentano diffractometer with Cu Kα radiation in order to identify the phases formed with respect to firing temperature. The BICUVOX-LSC

powder mixture (1:1 mol ratio) was obtained by mixing the LSC precursor solution into the BICUVOX powder, which in turn had been prepared by heating part of the BICUVOX ink used in screen printing to 800°C . The mixture was then dried and heated to 350°C for 1 h in air. BICUVOX-CGO powder obtained from heating part of the ink used in the screen printing ink to 800°C was studied separately in XRD at room temperature.

4.3 Results and Discussion

4.3.1 Phase and microstructure analysis

Fig. 4.1 shows the XRD patterns of the BICUVOX powder synthesized by solid state reaction and the BICUVOX-CGO powder mixture fired at 850°C. The XRD crystalline peaks of the BICUVOX powder can be indexed as $Bi_2V_{0.9}Cu_{0.1}O_{5.35}$ according to JCPDS card PDF no. 01-070-9191. In the BICUVOX-CGO mixture, a minor amount of at least one unidentified secondary phase (marked by "?") is detected aside from the BICUVOX and CGO phase (PDF no. 01-075-0161). Whether the phase(s) is/are mainly composed of decomposed BICUVOX or reacted components of BICUVOX and CGO, it is most likely that these phases have ionic conductivities lower than BICUVOX. Thus, the presence of the phase(s) is most likely disadvantageous.

Shown in Fig. 4.2 are the in-situ HT-XRD of the BICUVOX - LSC powder mixture, presented in ascending order starting from room temperature (RT1) up to 600°C. An XRD pattern (RT2) was also taken at room temperature after it has been cooled down from 600°C. The XRD pattern of the BICUVOX powder is also shown for reference. The shift of the XRD peaks towards low reflection angles reflects lattice expansion. The platinum peaks (▲, PDF no. 00-004-0802) in the pattern originate from the heater material. The presence of $Sr(NO_3)_2$ (*, PDF no. 01-076-1375) and $SrCO_3$ (▼, PDF no. 00-05-0418) is consistent with the HT-XRD observations on the LSC infiltrate (Chapter 2). Other minor phases as such Co_3O_4, $La_2O_2CO_3$, and $LaONO_3$ which were observed in our previous study were more difficult to detect. The $Sr(NO_3)_2$ peaks decreases with increasing temperature indicating decomposition whereas the amount of $SrCO_3$ increases with increasing firing temperature. The presence of $La_{1-x}Sr_xCoO_{3-\delta}$ is only detectable at 600°C. The HT-XRD results provide no indication that formation of other phases involving either the decomposition of BICUVOX or the reaction of BICUVOX and "LSC" phases at temperatures 600°C and below has occurred.

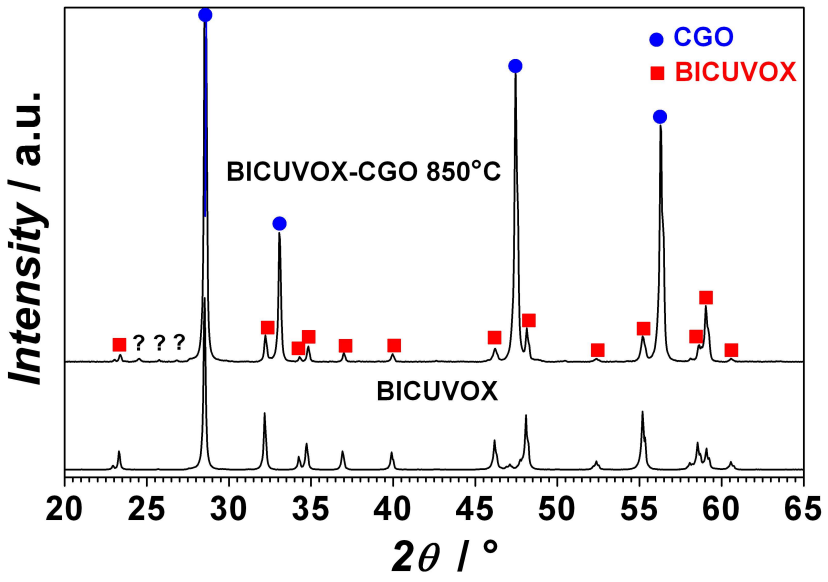

Figure 4.1: XRD patterns of the BICUVOX powder prepared by solid state reaction and the BICUVO-CGO screen printing ink fired at 850°C for 2 h in air.

The effect of firing temperature on the resulting BICUVOX backbone microstructure is shown in Fig. 4.3. It is seen in Fig. 4.3a that apparently, the connectivity between grains is achieved even at low firing temperature (600°C). However, the firing temperature is also insufficient to promote adhesion of the BICUVOX to the CGO electrolyte. A minimum firing temperature of about 800°C was necessary to ensure adhesion to the dense CGO electrolyte. At this high temperature, however, the BICUVOX looses porosity due to extensive grain growth as seen in Fig. 4.3c. It can also be seen that a layer in the BICUVOX backbone - CGO electrolyte exhibiting a typical intergranular fracture is clearly present for the backbone fired at 800°C. This suggests a diffusion or interdiffusion of elements from the BICUVOX backbone to the CGO electrolyte. Although the XRD results of the BICUVOX-CGO powder mixture fired at 850°C suggest no formation of new phases, one cannot exclude the possibility of a very thin reaction layer below the detection limit of XRD in the grain boundaries of CGO grains. To have at least, an information on the relative concentration of each of the elements in the diffusion/interdiffusion zone, an energy dispersive X-ray spectroscopy (EDS) line scan is performed along the length of the sample as shown in Fig. 4.4. The Cu signal was not included in the plots due to very low detection. The most noticeable feature is the increase in the Bi concentration near the BICUVOX layer. The exact

location of Bi is difficult to ascertain as well as the exact composition of the phases formed.

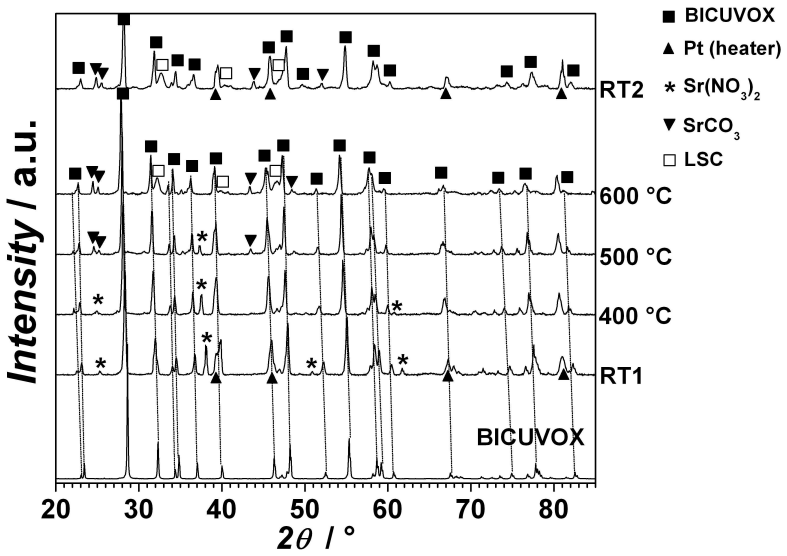

Figure 4.2: HT-XRD patterns of the BICUVOX-LSC powder mixture at RT≤T≤600°C. The BICUVOX powder was fired at 800°C. Identified phases are labeled.

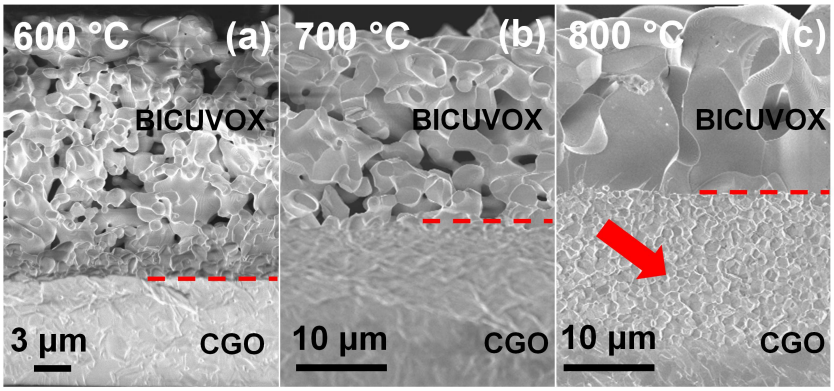

Figure 4.3: SEM micrographs of the BICUVOX backbone microstructure with firing temperature. (a) 600 (b) 700 and (c) 800°C. The diffusion layer between the BICUVOX backbone and the CGO electrolyte is marked by a red arrow. The dashed line marks the backbone-electrolyte interface.

The resulting microstructure of the BICUVOX - CGO composite screen printed and fired at 850°C on top of the dense CGO electrolyte is shown in Fig. 4.5. The relatively large BICUVOX grains are covered with interconnected grains of CGO about 200 nm in size. Disregarding other factors, this microstructure would have been advantageous since the BICUVOX grains could act as columns of fast ionic pathways, accepting oxygen ions from the high surface area CGO backbone and transporting them to the electrolyte. However, the electrochemical performance of this backbone infiltrated with LSC was greatly inferior to that of a pure CGO backbone infiltrated to the same degree with LSC, pointing to other factors that limit the effectiveness of this backbone. As in the case of pure BICUVOX, a diffusion layer between the composite backbone and the dense CGO electrolyte is seen.

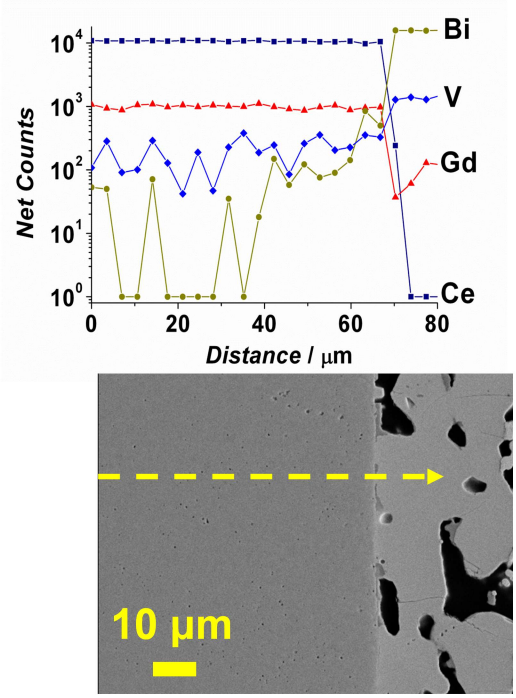

Figure 4.4: EDS line scans for Ce, Gd, V, and Bi taken along the yellow line running from the CGO electrolyte, CGO - BICUVOX interface, and the BICUVOX backbone. The plot is logarithmic in net counts to show the differences in low signal elements.

SEM micrographs of the BICUVOX backbone infiltrated with "LSC" and fired at 400 and 600°C are shown in Figs. 4.6 (a) and (b), respectively. It is not feasible in this case to distinguish between the desired Sr-doped $LaCoO_3$ and other phases. Although

the size of each LSC grain is difficult to discern, it is clear that the increase in firing temperature made the infiltrate densify. This is evidenced by the reduced thickness and greater density of the infiltrate, as seen in Fig. 4.6b. It is noteworthy that, due to the relatively large grain size of BICUVOX, its surface area able to accept the LSC infiltrate is low. Additional infiltration only adds to the layer of the infiltrate already deposited on the BICUVOX grain. In the case of the BICUVOX-CGO backbone (not shown), most of the LSC are distributed in the interconnected grains of CGO as expected.

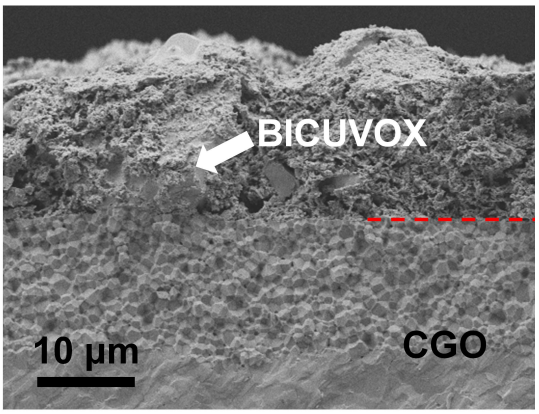

Figure 4.5: SEM micrograph of the BICUVOX-CGO composite backbone. A BICUVOX grain is marked by white arrow. The CGO is seen as fine particles covering the larger BICUVOX grains. The dashed line marks the backbone-electrolyte interface.

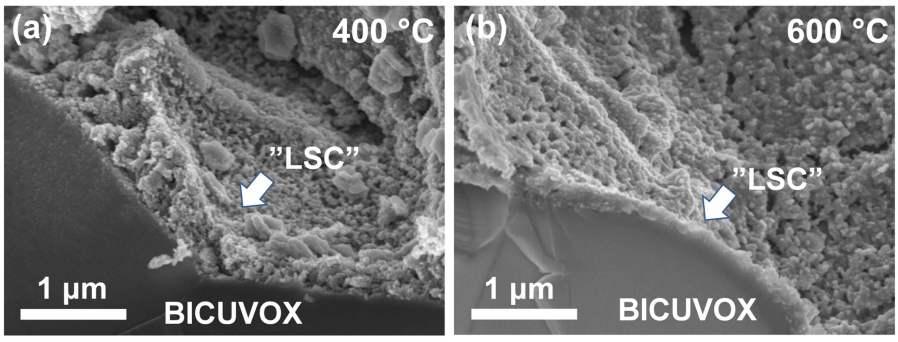

Figure 4.6: SEM micrographs of the LSC infiltrated BICUVOX backbone fired at (a) 400 and (b) 600°C.

4.3.2 Electrochemical performance

Fig. 4.7 compares the complex plane plots at 400°C in air of representative samples from all the infiltrated backbones fired at varying temperatures (T_{max}). Figs. 4.7a and 4.7b shows that of a pure BICUVOX backbone and a BICUVOX - CGO composite backbone both infiltrated with LSC, respectively. A pure CGO backbone infiltrated the same number of times with LSC and fired at $T_{max} = 600$°C is shown in Fig. 4.7c for comparison. Whenever possible, the impedance spectra in Fig. 4.7a and 4.7b are fitted by a series of resistors (R) and constant phase elements (Q) in parallel such as the equivalent circuit shown in Fig. 4.7d. No attempt was made to fit the cathode polarization resistance, R_p, at $T_{max} = 600$°C in Fig. 4.7a as the uncertainty associated with the low frequency process would be unacceptably large. Spectra at lower temperatures which do not show clear arcs were also not fitted. Correspondingly, the data points were excluded in the calculation of the activation energy. The small high frequency arc in all the spectra at 400°C is attributed to an electrolyte process. The same arc is not seen at higher temperatures but only manifested as a high frequency intercept of the spectra. This total resistance is referred to as R_s in this study. The remaining RQ elements represent electrode processes. The total resistance associated with these elements is the cathode polarization resistance (R_p). The R_p values are used as a gauge for the electrochemical performance of the infiltrated cathodes.

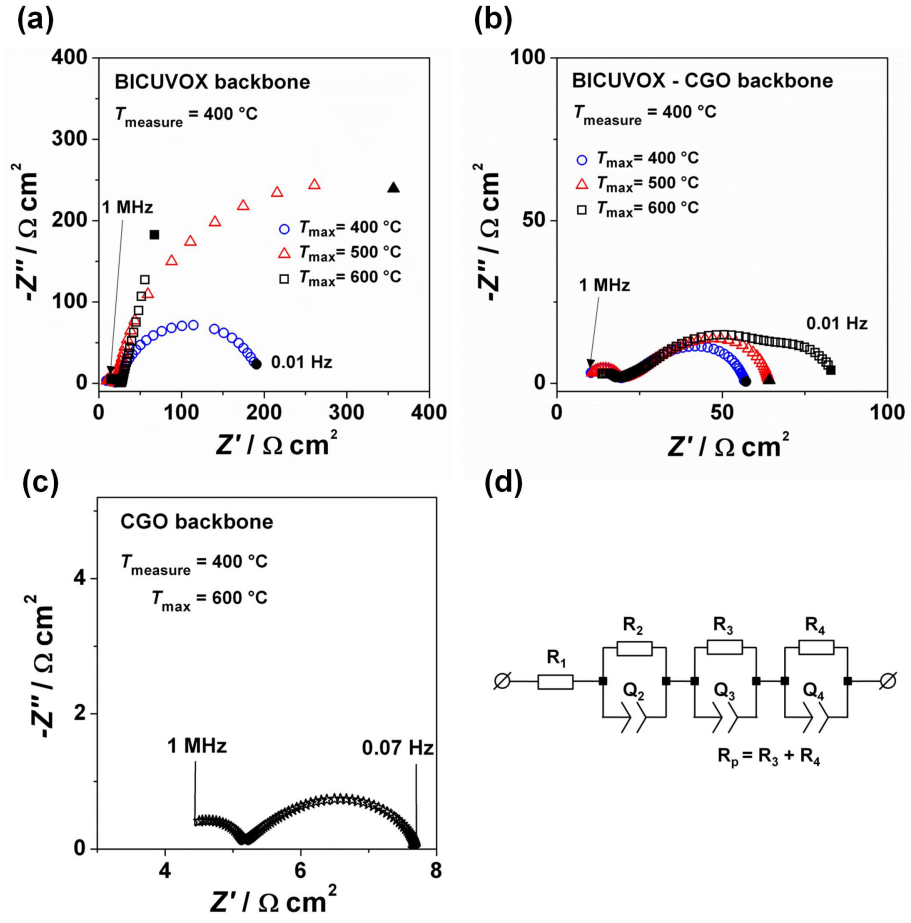

Figure 4.7: Representative impedance plots obtained at 400°C for the infiltrated BICUVOX-based samples fired at different temperatures. (a) BICUVOX backbone infiltrated 6 times with LSC (b) BICUVOX-CGO backbone infiltrated 6 times with LSC. (c) LSC infiltrated CGO cathode from Chapter 2. (d) The equivalent circuit used to fit the data in (a) and (b). The electrode contribution in the impedance spectra at T_{max} = 600°C in (a) is not fitted.

Although the R_p values vary across samples, a similar trend is observed in all the samples - R_p increases with increasing LSC firing temperature up to 600°C. This was seen for all measuring temperatures and is summarized in Fig. 4.8 which shows a plot of R_p against reciprocal absolute temperature. Figs. 4.8a and 4.8b shows that of a pure BICUVOX backbone and a BICUVOX - CGO composite backbone both infiltrated with LSC, respectively. The behaviour of increasing R_p with increasing LSC

firing temperature is different from the findings on CGO backbones infiltrated with LSC and tested in the same LSC firing temperature range (see Chapter 2). It was found in that the increase in LSC firing temperature up to 600°C decreases R_p due to increasing electrocatalyst formation. In this case, it is clear that the firing temperature intended to form the LSC electrocatalyst made the R_p higher. There are several factors that could contribute to this behaviour. One is the morphological change in the LSC material as the firing temperature is increased. As seen in the SEM micrographs in Fig. 4.6, the increased LSC firing has caused the infiltrated material to densify, decreasing the available area for oxygen surface exchange and consequently increasing R_p. Although plausible, it is suspected that this contribution is of minor significance considering that the effect was not seen in the LSC infiltrated CGO backbones where the same morphological changes were observed as the LSC was fired from 400-600°C. Another possible reason for the poor performance of the BICUVOX based samples is the formation of a very thin reaction layer (below the detection limit of XRD) in the LSC infiltrate-BICUVOX backbone interface. This is supported, as when the infiltrate firing temperature is increased, the interfacial resistance slightly increased. Although this requires confirmation with transmission electron microscope (TEM), the higher activation energies obtained at $T_{max} = 500$°C of the LSC infiltrated BICUVOX and BICUVOX-CGO backbones, 107 kJ mol^{-1} and 114 kJ mol^{-1}, respectively, compared to a LSC infiltrated CGO backbone (100 kJ mol^{-1}, 4.8b) provides a very strong indication that an interface effect is at play.

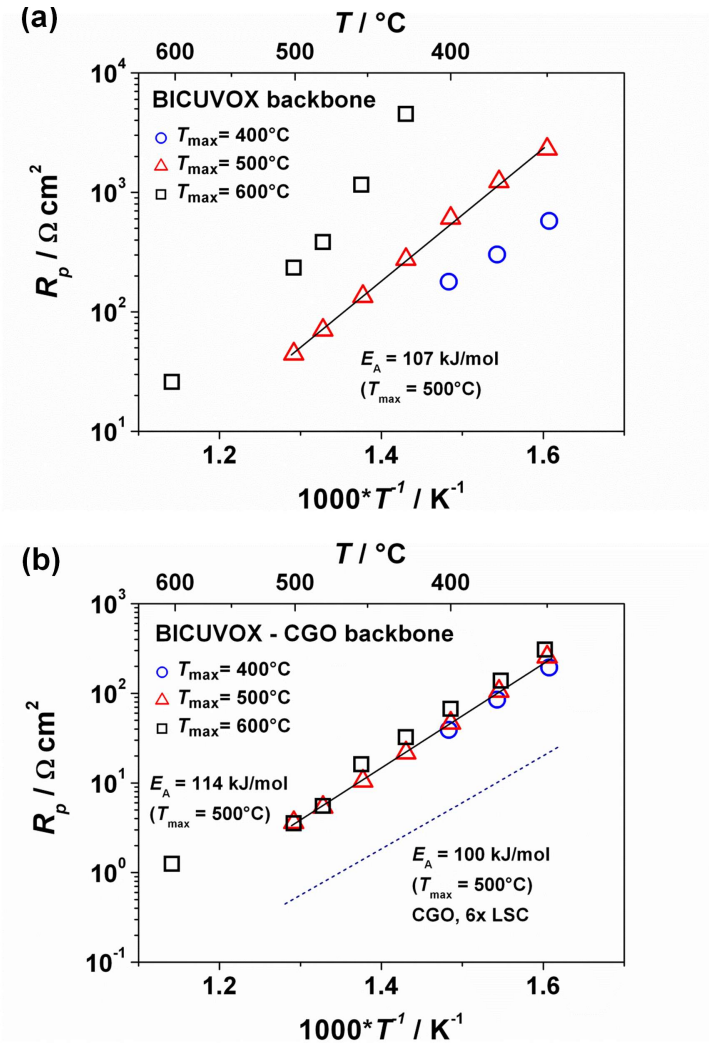

Figure 4.8: R_{p}, as a function of the reciprocal absolute temperature at varying LSC firing temperatures for (a) BICUVOX backbone and (b) BICUVOX-CGO backbone infiltrated 6× with LSC. The dashed line in (b) represents the R_{p} values of the LSC infiltrated - CGO cathode fired at T_{max} =500°C.

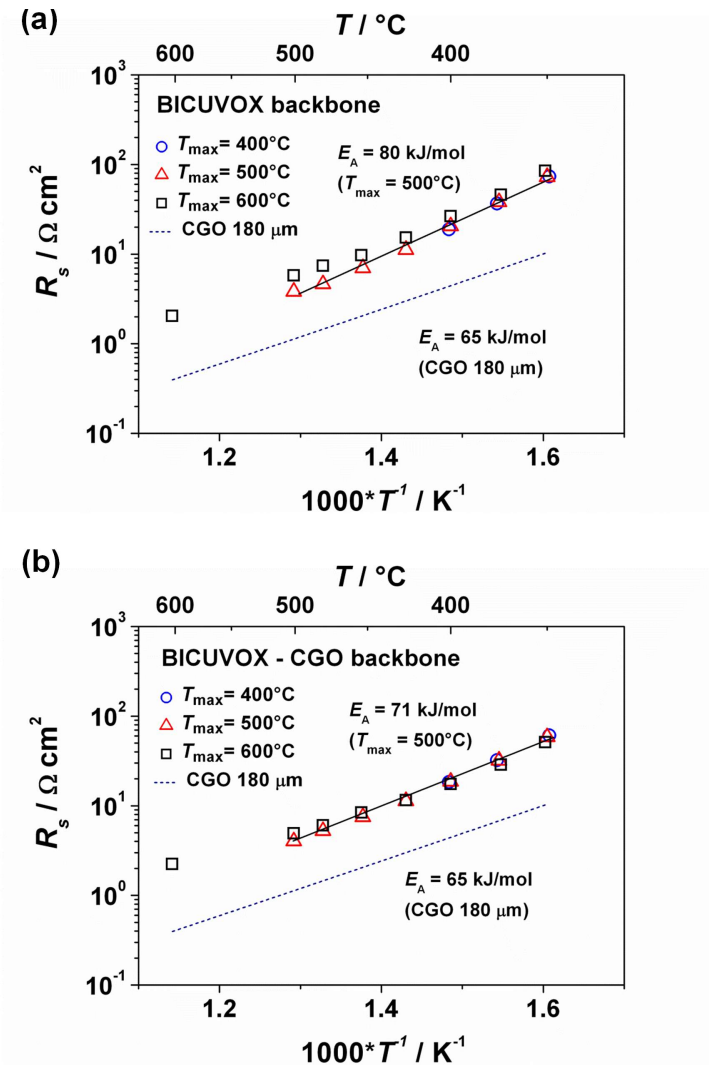

Figure 4.9: R_s, as a function of the reciprocal absolute temperature at varying LSC firing temperatures for (a) BICUVOX backbone and (b) BICUVOX-CGO backbone infiltrated 6× with LSC. The dashed lines represent the calculated series resistance of a 180 μm CGO electrolyte [43].

Looking back at Fig. 4.7 and Fig. 4.8, it is clear that the R_p values of the infiltrated BICUVOX-CGO cathode were much lower compared to the infiltrated BICUVOX cathode. This is not surprising considering the increased surface area added to accept the LSC electrocatalysts when the very fine CGO particles were mixed with the BICUVOX backbone. However, the polarization resistance values of this cathode are still much

higher than corresponding cathodes prepared using a pure CGO backbone as shown in Fig. 4.7c. At 500°C, the BICUVOX backbones infiltrated 6 times with LSC has an R_p = 44 Ω cm^2. This is ca. 100 times higher than the one obtained for a CGO backbone subjected to the same number of infiltrations of LSC even though the total conductivity of BICUVOX at 500°C (0.057 S cm^{-1}) was 7 times higher than CGO at this temperature. It can be speculated that given the very high values of R_p, the role of Pt paste current collector may be significant considering that the "LSC" is a multiphase mixture containing $SrCO_3$. However, as seen in Appendix A, the performance of a cell containing only the Pt paste current collector is strongly inferior to that of an LSC infiltrated - BICUVOX cathode.

Another point that must be addressed here is the relatively high measured R_s especially at low temperatures in all the BICUVOX infiltrated cathodes. The effect is clearly seen on the plots of R_s as a function of inverse absolute temperature as seen in Fig. 4.9. The relatively high ionic conductivity of the BICUVOX backbone as verified by impedance measurements of the BICUVOX pellet rules out the possibility that this is due to a low oxide ion conductivity in the backbone. Thus, it is conceivable that a charge transfer step in either or both the interfaces of the electrocatalyst/backbone and backbone/electrolyte is limiting the exchange of oxide ions. It is beyond the scope of this study to differentiate the two contributions. What is clear is that these exhibit a significant increase in the activation energy (Fig. 4.9). The activation energies range from 71 to 80 kJ mol^{-1}. This is higher when compared to the calculated series resistance of the CGO electrolyte used in the infiltrated cathodes (65 kJ mol^{-1}) [43].

4.4 Summary

Electrochemical characterization of BICUVOX and BICUVOX-CGO backbones infiltrated with LSC was carried out to evaluate these materials as possible cathodes for SOFCs. It was found that the lowest possible firing temperature (400°C) for the infiltrates was necessary in order to obtain the lowest cathode polarization resistance. Although HT-XRD indicate no formation of new phases involving the BICUVOX backbone and the LSC infiltrate material as the firing temperature is increased, the electrode polarization resistance increased indicating an unfavorable interface effect at the backbone-infiltrate boundary. The lowest polarization resistance at 500°C for BICUVOX backbones infiltrated 6 times with LSC was 44 Ω cm^2. This value is approximately 100 times higher than the one obtained for a CGO backbone subjected to

the same number of infiltrations of LSC even though the total conductivity of BICUVOX at 500°C (0.057 S cm^{-1}) was approximately 7 times higher than that of CGO at this temperature. The addition of CGO in the BICUVOX backbone minimized the negative effects of the BICUVOX backbone by increasing the amount of available surface area to accept the infiltrate material and by enhancing the compatibility of the BICUVOX-CGO backbone and CGO electrolyte. It was also found that the high processing temperature required for the BICUVOX backbone to attain adhesion to the dense CGO electrolyte severely restricts any favorable microstructure that can be obtained for this material and thus limits the amount of electro-catalytic material that it can accommodate through the infiltration method. The restriction in attaining a favorable microstructure due to the low melting point of BICUVOX based backbone and its poor compatibility with LSC even at processing below 600°C in the infiltration method, far outweigh its perceived advantage as a high oxide ion conducting backbone in Co-based infiltrated cathodes.

Chapter 5

Anode supported cells with LSC infiltrated - CGO cathode[†]

5.1 Introduction

The advantages of employing infiltration to prepare cathodes for SOFCs have already been described in Chapter 1. Despite the advantages over their conventionally prepared counterparts, the use of infiltrated cathodes in complete fuel cells is so far limited. As a consequence, so is the knowledge of the lifetime of infiltrated electrodes under long term operation. Possible reasons for not implementing this type of cathode in SOFCs are among others: (*i*) the need for multiple number of infiltrations to achieve the desired amount of electrocatalysts, and (*ii*) the perceived instability of nanoparticulate infiltrates during long term operation. Specifically, the high surface area-nanoparticles are highly prone to coarsening and grain growth which increase R_{p}.

Studies on long term stability of infiltrated cathodes have been very limited to date, despite its importance for the application of fuel cell technology. The problem of coarsening in an infiltrated cathode has been demonstrated by Wang et al. [100] on a cathode consisting of $La_{0.8}Sr_{0.2}FeO_{3-\delta}$ (LSF) infiltrated onto a yttria-stabilized zirconia (YSZ) backbone, where a symmetrical cell fired at 850°C shows a linear increase in R_{p} from 0.15 to 0.55 Ω cm^2 after testing for 2500 h at 700°C. As also seen in Chapter 2, SEM observations on LSC infiltrated - CGO symmetrical cathodes also demonstrated a certain degree of particle coarsening depending on the maximum infil-

[†]Co-authors: Per Hjalmarsson, Martin Søgaard, Johan Hjelm, and Nikolaos Bonanos.

trate firing temperature and operation time. In other studies, however, it appears that other infiltrated cathodes possess a high degree of stability for long term operation. For example, no increase in R_p was observed for a LSC infiltrated - $Sm_{0.2}Ce_{0.8}O_{1.9}$ (SDC) symmetrical cathode upon thermal cycles and holding at 600°C for 2000 h [64]. However, the R_p obtained in the aforementioned study was already fairly high (0.3 Ω cm^2) from the beginning of the test where the electrode was fired at maximum temperature of 800°C. High stability was also reported for a cathode with $La_{0.6}Sr_{0.4}MnO_{3-\delta}$ (LSM) infiltrated into scandia stabilized zirconia (SSZ) and fired at a maximum temperature of 900°C. The infiltrated cathode with Ni-SSZ anode and SSZ as electrolyte showed no significant changes in the electrochemical performance or microstructure after testing for 500 h at 650°C under relatively low, near-constant applied current of 0.15 A cm^{-2} [101]. Long term stability of infiltrated cathodes is still an open issue and requires a more comprehensive study to understand the effects of several factors such as the operating temperature, infiltrate firing temperature, and infiltrate - backbone combination. Another important consideration is on how these infiltrated cathodes perform, when integrated into an actual SOFC and tested under high current densities.

In Chapter 2, an exceptional initial performance of a symmetric cell of an LSC infiltrated - CGO cathode (0.044 Ω cm^2 at 600°C) was presented. The infiltrated cathode also showed satisfactory stability during long term operation, with R_p leveling out at 0.07 from 0.04 Ω cm^2 after 450 h at 600°C. In the present chapter, such a cathode has been integrated onto an anode supported, thin electrolyte SOFC and tested for long term stability. The anode supported half cell consists of a Ni-YSZ anode support, a Ni-ScYSZ anode, where ScYSZ is scandia-doped yttria-stablized zirconia, a ScYSZ electrolyte, and a CGO barrier layer. A schematic cross section of the cell is shown in Fig. 5.1. A long-term test running over 1500 h under constant operating conditions was performed on the cell. Scanning electron microscopy was employed to analyze the microstructures of the cathode after long term testing. The in-plane electronic conductivity of the infiltrated cathode was also investigated to estimate the extent of its contribution to the ohmic loss in the cell.

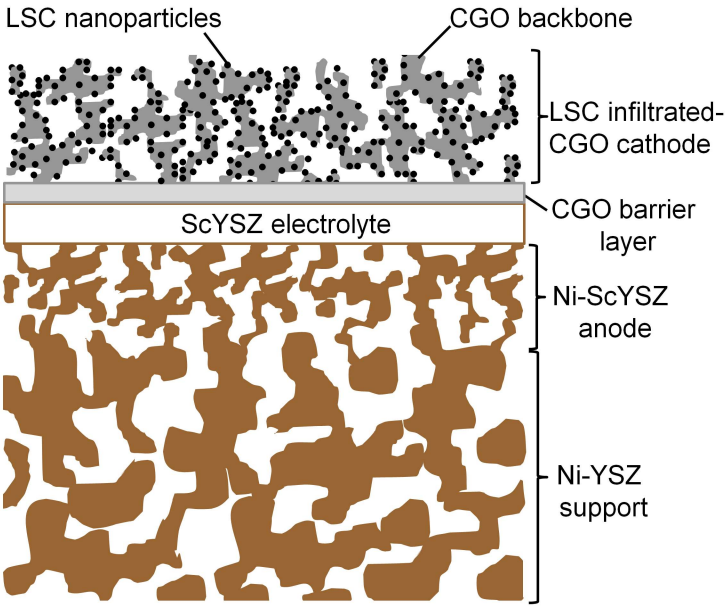

Figure 5.1: Schematic of the anode supported cell used in the study. The relative thicknesses and microstructures are not drawn to scale.

5.2 Experimental

The electronic conductivity of the infiltrated cathode in a symmetrical cell configuration was studied as a function of LSC loading and LSC firing temperature. The preparation of the infiltrated cathodes were as described in Chapter 2. The in-plane electrical conductivities of samples infiltrated 6, 9 and 12 times with LSC were measured using a 4-probe direct-current (DC) method. A schematic of the set up for one symmetric cell is shown in Fig. 5.2a. Platinum wires were wound near the end sides of the sample and additionally painted with Pt paste to ensure a negligible contact resistance of the wire to the infiltrated cathode. Current was passed through the sample and the voltage drop was measured across a distance, l, in the middle of the sample. The samples were placed in series together with a 1 Ω resistor to monitor the current, as shown in Fig. 5.2b. The resistance obtained (R_{eq}) corresponds to that of the two cathodes in parallel. Although the electrolyte and porous backbone also carry some of the current in the form of oxide ions, this is estimated to be much smaller than that carried by the

cathodes. This can be argued from the fact that the measured R_{eq}'s are significantly smaller[†] than that of the resistance calculated for dense CGO using literature values for its conductivity [43] and dimensions used in the experiment. The R_{eq}'s from each of the samples are calculated from the measured current running through the circuit and the voltage drops from each sample. The conductivity at each LSC firing temperature is then calculated using the equation, $\sigma = l/RA$, where A is the cross-sectional area of the infiltrated cathode, and $R = 2R_{eq}$.

A 53 mm × 53 mm large anode supported half cell that consisted of a Ni-YSZ support/NiScYSZ anode/ScYSZ electrolyte/CGO barrier layer was manufactured by tape-casting and lamination and co-fired above 1200°C. Before screen printing the CGO backbone, a CGO precursor solution was spin coated on top of the CGO barrier layer and fired at 350°C to further enhance the connectivity of the barrier layer and the CGO backbone. To integrate the infiltrated cathode, an in house CGO ink was screen printed onto the half cell and fired at 1050°C for 2 h to serve as a backbone. The backbone was subsequently infiltrated nine times with a precursor solution of metal nitrates corresponding to the nominal composition $La_{0.6}Sr_{0.4}Co_{1.05}O_{3-\delta}$.

The cell was tested in a SOFC test setup as described in Ref. [102]. Custom glass sealant frames with glass softening and glass transition temperatures of approximately 670°C and 790°C, respectively, were used to seal the anode and cathode gas flow compartments. Gold and nickel meshes were used as current collector components on the cathode and anode side, respectively. Eight kilograms of weight was applied on top of the cell house to ensure gas tight sealants and electrical contact. The flow compartments were sealed at 850°C for 2 h prior to anode reduction in 9% H_2 in N_2 for 2 h and 4% H_2O in H_2 for 1 h. The cell was tested starting from 850°C down to 650°C in 50°C increments using $i - v$ polarisation and electrochemical impedance spectroscopy (EIS) measurements. The stability of the cell was investigated in a galvanostatic durability experiment carried out at 700°C and 0.5 A cm^{-2} with fuel and oxygen utilisation of 60% and 20% respectively. The cell was also characterized under different partial pressures of oxygen on the cathode side and of water vapour on the anode side.

[†]e.g. $R_{eq} = 11.5\ \Omega$ and $R_{\text{dense CGO}} = 1000\ \Omega$ at 600°C, 6× infiltration

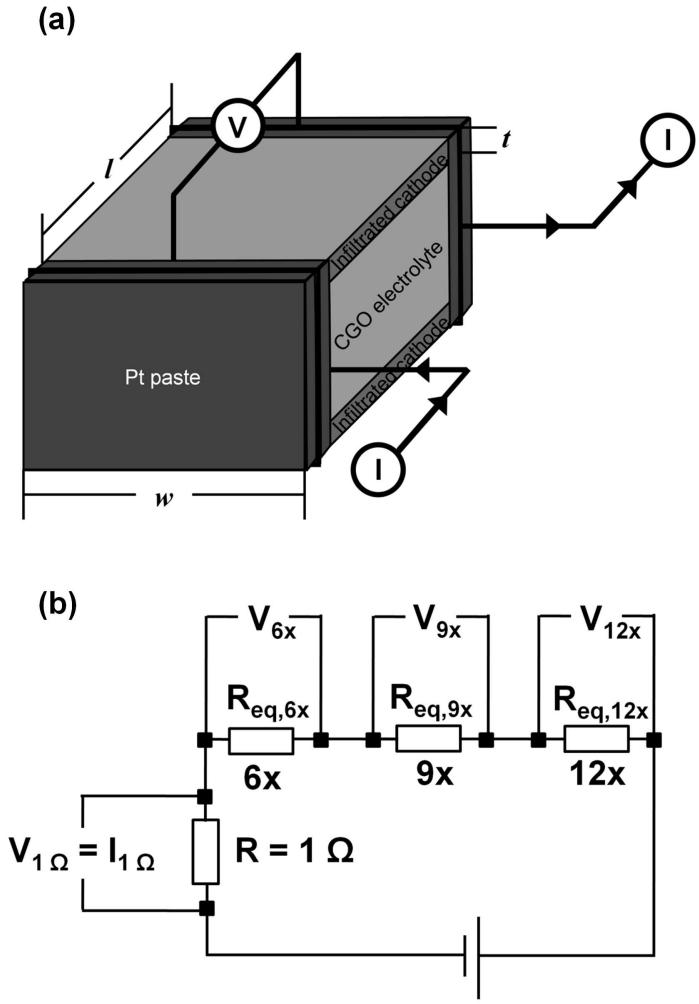

Figure 5.2: (a) Schematic of the in-plane conductivity measurement set-up for one symmetric cell. (b) The equivalent circuit used to measure the in-plane conductivity of the three symmetric cells (labeled 6×, 9×, and 12×). Voltage drops, $V_{\mathrm{n}\times}$, are recorded for each sample as a function of the LSC firing temperature.

Post-test microstructural analysis was carried out using a Zeiss Supra-35 scanning electron microscope on the infiltrated cathode and cell and on a nominally identical counterpart. The counterpart had been heated to 850°C for 6 h in air at a heating rate of 60°C h^{-1} in order to prepare a sample that is representative of a not long term tested SOFC.

5.3 Results and Discussion

5.3.1 Electrical conductivity of LSC infiltrated cathodes

Shown in Fig. 5.3 is the dependence of the total conductivity of the symmetric cells at 600°C with the number of LSC infiltrations and maximum LSC firing, T_{max}. It is important to point out that the "LSC" infiltrate discussed in this chapter is multi-phased as seen in Chapter 2. Hence, in reality the calculated conductivity originates from a mixture of these phases. It should also be noted that polished cross sections (not shown) of the samples infiltrated 9 and 12 times reveal a porous LSC residue layer with thicknesses between 500 nm - 1 μm on top of the LSC infiltrated - CGO backbone. In principle, the residue layer may interfere with the measurement of the in-plane electronic conductivity especially if the infiltrate has a very high electronic conductivity. Thus, the measured in-plane conductivity values for these samples will only be treated as maximum values. As the 6× infiltrated sample appear to not have a residue layer, the measured in-plane conductivity values for this sample will serve as a minimum for the 9 and 12× infiltrated samples. In practice, removing only the residue layer by polishing poses a challenge as it is difficult to ascertain that the infiltrated porous backbone has also not been removed.

From Fig. 5.3, it is clear that the conductivity increases with increasing number of infiltrations irrespective of T_{max}. This is most probably due to increasing connectivity among the LSC nanoparticles as the LSC loading is increased. For all the infiltrations, it is observed that the increase in T_{max} from 600 to 900°C causes a decrease in the total conductivity. For the 6× infiltrated sample, it has been shown in Chapter 2 that the increase in T_{max} above 600°C causes an increase in grain growth and coarsening. Thus, the trend observed in Fig. 5.3 for the 6× infiltrated sample with increasing T_{max} is most probably due to a loss of percolation due to grain growth and coarsening. For the 9 and 12× infiltrated samples, it was postulated in Chapter 2 that the loss of percolation due to grain growth and coarsening with increasing LSC firing temperature is not a problem in these samples. Thus, it is expected that the conductivity would remain almost constant or, as was suggested by the decrease in R_s in Chapter 2 for these samples, that the conductivity would increase with increasing firing temperature. As this is clearly not the case in Fig. 5.3, other factors have to be considered.

From the conductivity values, it is possible to estimate the ohmic loss contribution of the LSC-infiltrated cathode if it is integrated to an anode supported SOFC. The

number of infiltrations used in this study is fixed to 9× as this produces the lowest R_p's. Assuming that the conductivity is comparable to that of a 6× infiltrated sample and is isotropic, the ohmic loss contribution at 600°C for a 35 μm thick cathode and infiltrated 6× with LSC is only 0.59 - 3.4 mΩ cm^2 depending on T_{max}. For comparison, the ohmic loss from the combined thicknesses of the ScYSZ electrolyte and the CGO barrier layer based on SEM images is 112 mΩ cm^2 at 600°C. Thus, it appears that the electronic conductivity of the infiltrated cathode will not limit the performance of a common anode supported SOFC in terms of electronic ohmic loss, provided that proper current collection on the cathode side is in place.

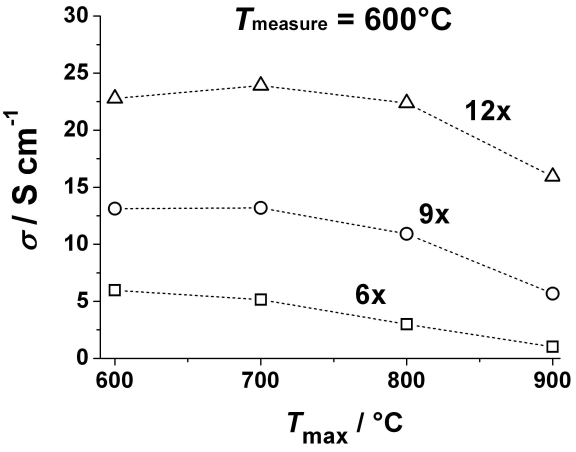

Figure 5.3: Dependence of the total conductivity of the LSC infiltrated cathodes with number of infiltrations and maximum firing temperature, T_{max}.

5.3.2 Cell performance and degradation

Figure 5.4a shows the impedance at open circuit voltage (OCV) of the anode supported cell (ASC) at 650, 700 and 750°C after heating the cell at 850°C. For comparison, the impedance spectra of a nominally identical cathode at OCV measured on a symmetric cell at 700°C is also shown in Fig. 5.4b. There were no impedance spectra at 650 and 750°C collected from the impedance measurements of the symmetric cell. Note that in this case, the symmetric cell was fired at T_{max} = 900°C. The serial resistance, R_s, which mainly originates from the 180 μm CGO electrolyte was subtracted from the impedance to focus only on R_p. It is seen that the R_p of the symmetric cell is 0.05 Ω cm^2. It is expected that the R_p for the symmetric cell will be slightly lower had it been

fired at 850°C as seen from relationships of R_p and T_{max} in Chapter 2. The impedance spectra of the ASC at 700°C in Fig. 5.4a indicate a total area specific resistance (ASR) of 0.73 Ω cm^2. From the thickness of the ScYSZ electrolyte estimated from SEM images and the ionic conductivity data of ScYSZ [103], the electrolyte ohmic loss contribution to the total ASR is 0.028 Ω cm^2 at 700°C. The other major contributor to the ohmic losses is most probably the CGO barrier layer. In general, the number of components and interfaces in an ASC and the factors during its operation makes it difficult to precisely distribute the ohmic loss contributions. What is clear, as pointed out in the conductivity calculations, is that the ohmic loss contribution of the LSC infiltrated - CGO cathode is not significant. Although the data are not sufficient to ascertain the polarization loss contributions of each of the electrodes, it is clear from Fig. 5.4 that the impedance contribution of the infiltrated cathode is probably not above 7 % out of the total impedance of the cell. Fig. 5.4c shows a comparison of the impedance spectra of the ASC with LSC infiltrated - CGO cathode and an ASC with a screen printed LSC - CGO (50:50 wt%) composite cathode at 750°C. The two cells have identical anode supports. The ASC with LSC infiltrated - CGO cathode exhibits a higher ASR. It is not clear why this is the case, considering that in symmetrical cell testing, the LSC infiltrated cathodes fired at a maximum 900°C show comparable R_p's with that of screen printed LSC-CGO (50:50 wt%) composite cathodes at high temperatures (> 600°C). This is shown in Fig. 5.5. The lower activation energy of the LSC infiltrated - CGO cathode is associated to a larger amount of CGO phase compared to the LSC-CGO composite cathode. CGO has lower activation energy for oxide ion conduction than LSC as pointed out in Section 1.4.1. Future studies involving low temperature maximum firing for the LSC infiltrate and low temperature operation, where it is found to have lower R_p's than a conventional LSC-CGO composite cathode, and extended long term testing involving thermal cycling could provide a more comprehensive assessment of the advantages and disadvantages of LSC infiltrated cathodes.

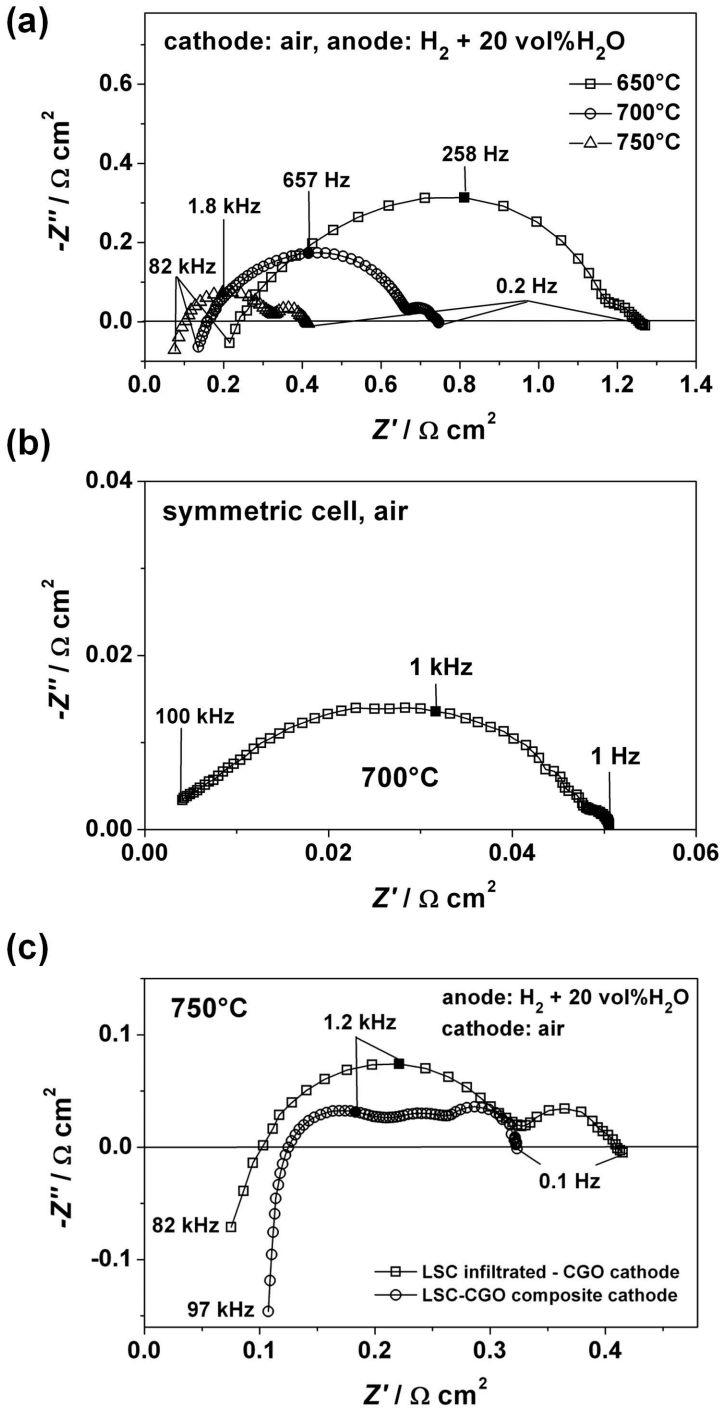

Figure 5.4: Impedance spectra at OCV. (a) ASC at 650, 700 and 750°C (b) Symmetric cell with LSC-infiltrated cathode at 700°C (c) ASC with LSC infiltrated - CGO cathode compared to an identical ASC with screen printed LSC-CGO cathode at 750°C.

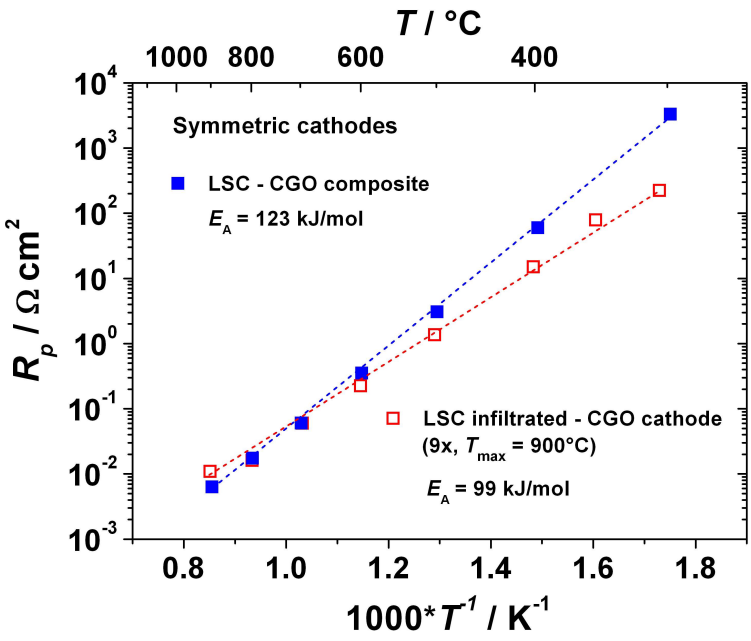

Figure 5.5: R_p as a function of the reciprocal absolute temperature for an LSC-CGO cathode and an LSC infiltrated - CGO cathode. The number of infiltrations is 9× and the LSC infiltrate is fired at 900°C.

The comparatively small contribution of the infiltrated cathode to the overall R_p can be seen in the Distribution of relaxation times (DRT) analysis of the cell as shown Fig. 5.6 for different oxygen and fuel partial pressures on the cathode and anode side, respectively, at 700°C. A DRT analysis of a symmetric LSC infiltrated - CGO cathode is also shown for comparison. The impedance response is seen to consist of two main regions in different frequency ranges, 100 - 1000 Hz and 1 - 10 Hz. The region 1 - 10 Hz can be attributed to conversion and gas diffusion at both the anode and cathode side. This response is not related to the electrochemical characteristics of the cell and is thus of less interest from an electrochemical point of view. It will therefore not be discussed further in this chapter. The main interest is the major impedance response at 100 - 1000 Hz. No considerable shift in this response is seen when the p_{O_2} at the cathode side is changed from 0.06 to 0.6 atm. However, when the $p_{\mathrm{H_2O}}$ is lowered from 0.20 to 0.04 atm while keeping the p_{O_2} in the cathode side to 0.21 atm, a shift in peak frequency and magnitude is observed. This suggests that the major contributor to the R_p in the range 100 - 1000 Hz is related to the anode. This agrees well with the comparatively low resistance for this type of cathode when measured in a symmetrical

cell configuration.

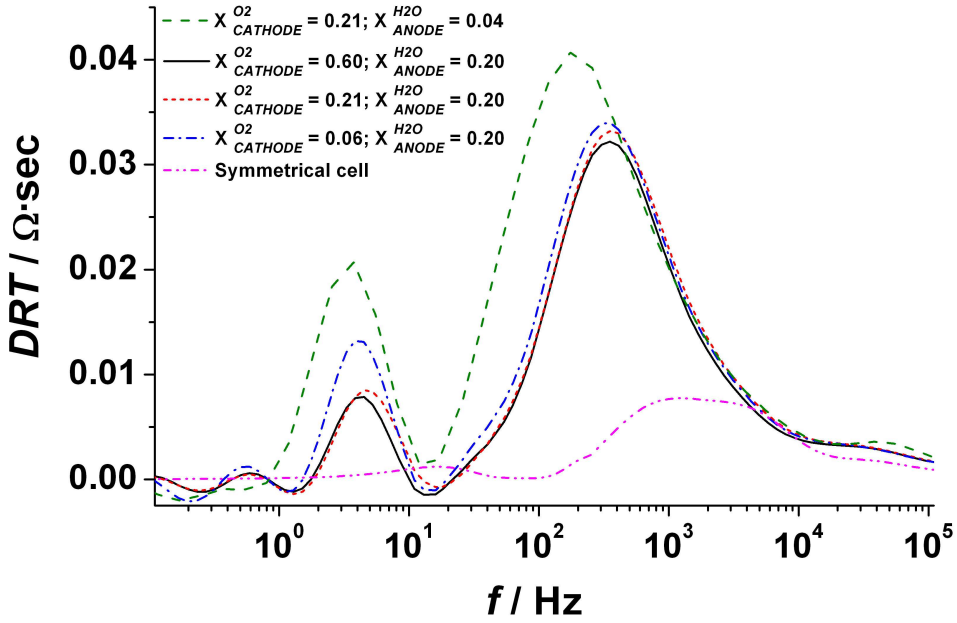

Figure 5.6: DRT analysis of the impedance measured at OCV after 1500 h testing at 700°C for different cathode p_{O_2} and anode p_{H_2O}.

Fig. 5.7 shows the cell voltage of the ASC, recorded at a constant applied current density of 0.5 A cm^{-2} for 1500 h at 700°C. This long term galvanostatic test was started after an initial characterization of the cell , which means that the infiltrated cathode has been heated to 850°C for several h. It is evident from Fig. 5.7 that the cell exhibits excellent stability with no measurable loss in cell voltage over 1500 h. The stability is also evident in Fig. 5.8 showing no measurable change in the impedance recorded *in situ* during the test. Also, from Fig. 5.8, it is obvious that no noticeable changes in both the serial resistance, R_s, and polarization resistance, R_p, can be observed. The impedance spectra in Fig. 5.8 indicate a total area specific resistance (ASR) of 0.52 Ω cm^2. The present data is insufficient to deconvolute the contributions of each of the electrodes to the polarization resistance. However, as explained earlier, symmetric cell characterizations of the LSC infiltrated cathode at OCV indicates that the cathode contribution to the overall R_p does not exceed 10 %. This approximation assumes that the cathode impedance does not increase under current loading. There is reason to

believe that this could be the case as a recent study on the current-static, cathodic polarization behavior of an LSC electrode on a samaria-doped ceria electrolyte does not yield any considerable effect on the performance of the LSC electrode [104]. It is clear from Fig. 5.7 and 5.8 that no significant degradation of the infiltrated cathode has occurred. The results also indicate stability of the other cell components during continuous operation.

Shown in Fig. 5.9 are the $i-v$ and power characteristics at 750°C of the ASC after long term testing. Similar data for an ASC with a screen printed LSC-CGO cathode and nominally identical anode support and electrolyte is also shown for comparison. The power density of the ASC with a LSC infiltrated - CGO cathode reached 0.79 W cm^{-2} at 750°C at a cell voltage of 0.6 V. The ASC with LSC - CGO composite cathode is clearly superior in terms of power characteristics, but as mentioned previously, more studies are required to assess the advantages of an LSC-infiltrated cathode.

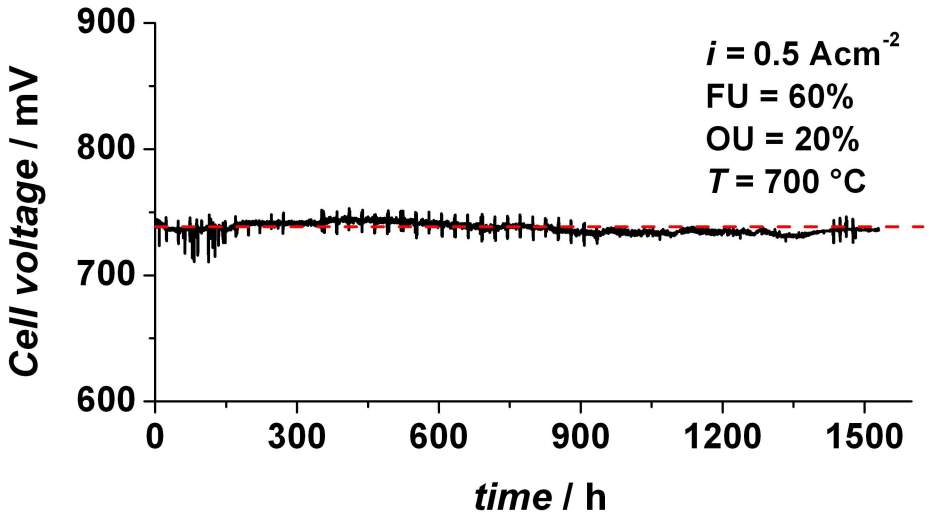

Figure 5.7: Cell voltage as function of operating time at 700°C under a constant applied current of 0.5 A cm^{-2}. The red dotted line indicates the cell voltage at the start of the test. The fuel utilization (FU) is adjusted to 60% on the anode side and 20% oxygen utilization (OU) on the cathode side. Spikes indicate impedance measurements.

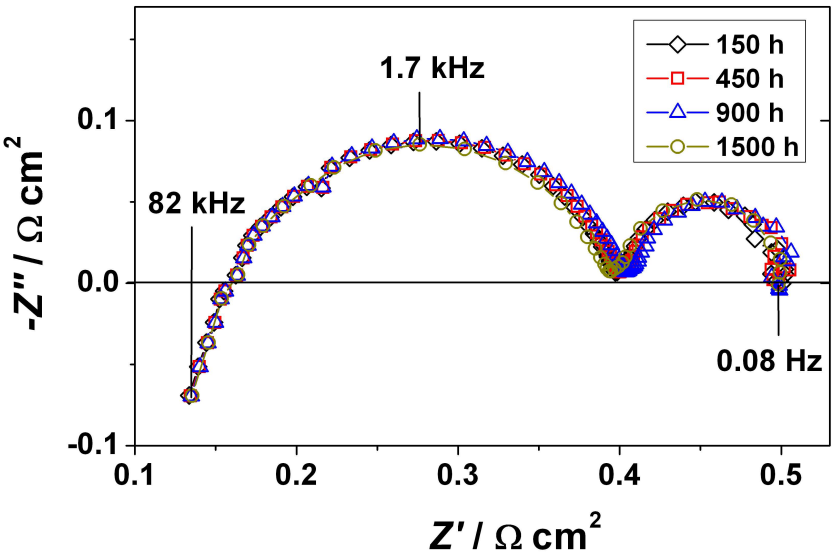

Figure 5.8: Impedance spectra during testing at 700°C under constant applied current of 0.5 A cm^{-2}. Impedance spectra recorded at selected times are shown.

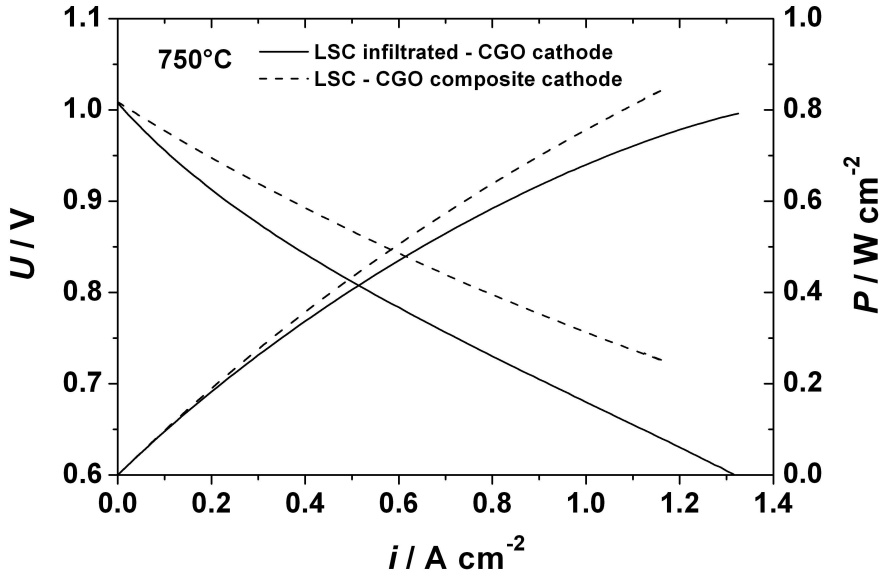

Figure 5.9: Current-voltage and power curves for the anode supported cell with LSC infiltrated - CGO cathode and LSC-CGO composite cathode at 750°C.

5.3.3 Post test characterization

The SEM micrographs in Fig. 5.10 provide an overview of the cross section of the cell after long term testing. The magnified image shows in greater detail the anode, electrolyte, and cathode interfacial regions. No sign of significant microstructural damage such as cracks are observed in any of the components. Another noticeable feature is the layer between the infiltrated cathode and the Sr-doped lanthanum manganite (LSM) current collector. This layer is composed of LSC that has not been completely infiltrated into the porous CGO backbone. Clearly, this residue layer, which is about 15 μm is much thicker than what is usually obtained for a symmetric cell as discussed previously (500 nm - 1 μm). The much larger area of the CGO backbone in the ASC collects much more residue and is harder to remove than in the symmetric cell case. The microstructure, electrochemical performance, and in-plane electronic conductivity of this LSC residue layer have been investigated and the results are shown in Appendix B. It is found that this layer can, in itself, function as a cathode with an $R_{\mathrm{p}} = 0.19$ Ω cm^2 at 600°C in air when fired at 600°C. However, as the firing temperature is increased, the R_{p} drastically increases ($T_{max} = 900$°C, 10.5 Ω cm^2 at 600°C), which is most probably due to a decreasing surface area for oxygen surface exchange as the layer starts to densify. It is not difficult to see that the presence of a CGO backbone is important, as it not only spreads the active surface area, but also provides a support to the LSC infiltrate which can limit the grain growth and densification of the infiltrate. As also discussed in Section 1.4.1, one important role of the CGO backbone is that, due to its lower activation energy for oxygen ion conduction than LSC, the R_{p} for an LSC infiltrated - CGO cathode does not drastically increase with decreasing temperature (see Appendix B). This makes the composite structure a much more feasible choice for operation at low temperatures.

In terms of electronic conduction, the layer was found to have a very high effective in-plane electronic conductivity. Thus, the LSC residue layer seen in Fig. 5.10 could have not possibly limited the transport of electrons from the current collector to the LSC infiltrated - CGO cathode. Poor electronic conduction could have led to a significantly higher ohmic loss.

Fig. 5.11 shows the SEM micrographs of the infiltrated cathode before and after long term test. The LSC phase is seen as interconnected particles of approximately 50 - 100 nm in size, coating the larger ($\sim$ 200 nm) CGO particles. Several regions were examined in both cases but as seen in Fig. 5.11b, the microstructure of the

infiltrated cathode after 1500 h of testing did not change in a clear visible way. Thus, it appears that the firing (during testing) performed at 850°C was sufficiently high to induce a relatively stable LSC particle size and microstructure suited for a lower operating temperature (700°C) even for a prolonged period of operation. These results are consistent with the very stable electrochemical performance measured on the ASC.

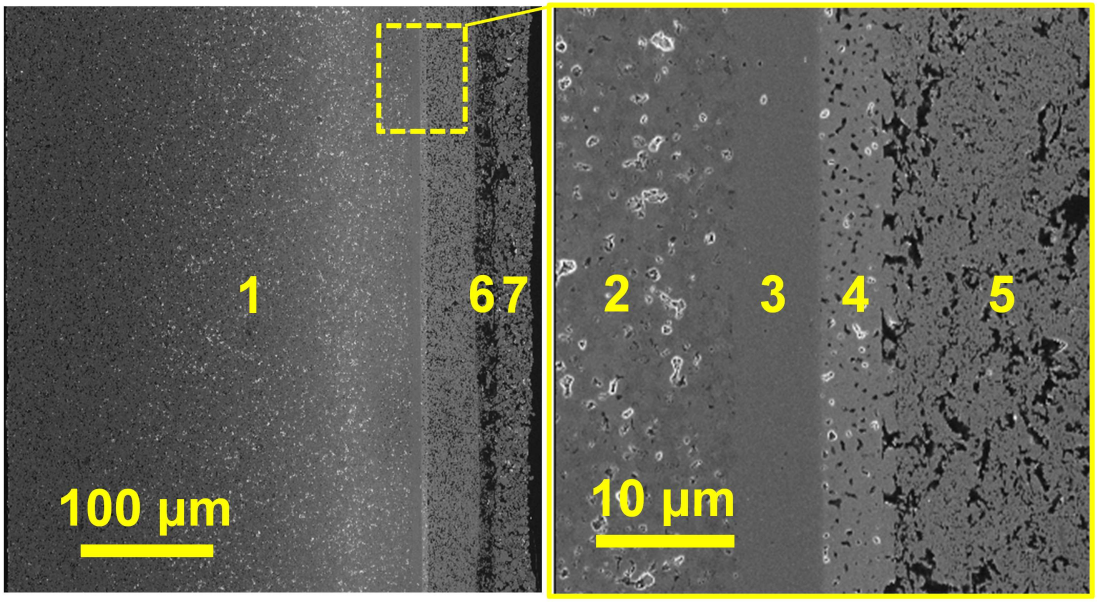

Figure 5.10: Post mortem SEM micrographs of the cross section of the cell. A magnified image showing the anode, electrolyte, CGO barrier layer, and cathode is also shown. 1 - Ni-YSZ anode support, 2 - Ni-ScYSZ anode, 3 - ScYSZ electrolyte, 4 - CGO barrier layer, 5 - LSC infiltrated-CGO cathode, 6 - LSC residue layer, and 7 - Sr-doped lanthanum manganite (LSM) current collector.

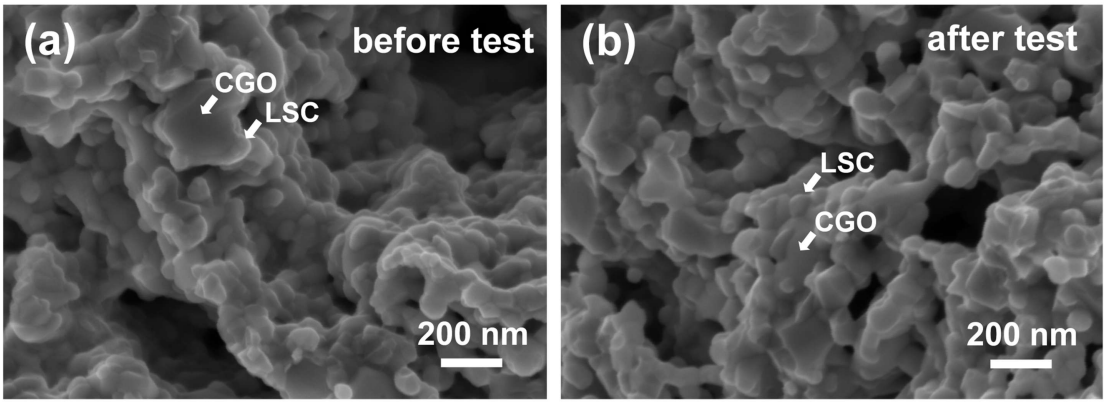

Figure 5.11: SEM micrographs of the LSC infiltrated - CGO cathode (a) before and (b) after testing for 1500 h at 700°C under constant applied current of 0.5 A cm^{-2}. CGO and LSC particles are identified.

5.4 Summary

An anode supported cell with a LSC infiltrated - CGO cathode has been developed which showed high electrochemical stability. The cell was found to be electrochemically very stable with no measurable degradation during a 1500 h long operation at 700°C and 0.5 A cm^{-2}. The power density of the ASC reached 0.79 W cm^{-2} at 750°C at a cell voltage of 0.6 V. Impedance spectra recorded *in situ* during the test found no changes in the electrochemical behavior of the cell. Post test microstructural investigation by SEM on the cathode side revealed no significant change in grain size and microstructure of the LSC infiltrate when compared to an untested counterpart fired at the same maximum temperature. The apparent stability of the anode supported cell with an LSC infiltrated - CGO cathode should provide a motivation to explore the integration of a cathode prepared by infiltration into SOFC technology.

Chapter 6

$Ca_3Co_4O_{9+\delta}$ as cathode for SOFCs[†]

6.1 Introduction

Most of the reported candidate materials for IT-SOFCs consists of mixed-ionic electronic conductors (MIECs) and are of the perovskite type (LnSr)(CoFe)$O_{3-\delta}$, (Ln=La-Yb) [30], typically (LaSr)(FeCo)$O_{3-\delta}$ (LSCF) [105, 63, 106, 90]. As also pointed out in Chapter 1, these materials have been investigated intensively because of their good catalytic activity for oxygen reduction, high oxide ion conductivity, and high electronic conductivity. However, the disadvantages of these types of materials are their known chemical reactivity with zirconia-based electrolytes and their thermal expansion mismatch (e.g. $La_{0.6}Sr_{0.4}CoO_{3-\delta}$, TEC $\sim 20 \times 10^{-6}$ K^{-1} [107]) with that of commonly used SOFC electrolytes such as yttria stabilized zirconia (TEC $\sim 10 \times 10^{-6}$ K^{-1} [13]), gadolinia doped ceria (TEC 12.5×10^{-6} K^{-1} [97]), and $La_{1-x}Sr_xGa_{1-y}Mg_yO_3$ (TEC 10×10^{-6} K^{-1} [108]).

The misfit-layered cobaltite $Ca_3Co_4O_{9+\delta}$, which are extensively used as a thermoelectric material [109] has also been investigated as a candidate cathode material for IT-SOFCs [110, 111]. In addition to its matching thermal expansion coefficient (9-10 $\times$ 10^{-6} K^{-1}) and its good chemical stability with standard CGO IT-electrolyte, the com-

[†]Parts of this chapter has been published as A. J. Samson, M. Søgaard, N. V. Nong, N. Pryds, and N. Bonanos,"Enhanced electrochemical performance of the solid oxide fuel cell cathode using $Ca_3Co_4O_{9+\delta}$", *J. Power Sources*, 196 (2011) 10606-10610.

posite of $Ca_3Co_4O_{9-\delta}$ and CGO was found to exhibit an electrochemical performance not prohibitively high for use in IT-SOFCs [110]. This misfit-layered structure can be described as $[Ca_2CoO_3]_{b1/b2}[CoO_2]$ consisting of alternate stacking of a rocksalt-type Ca_2CoO_3 layer and a CdI_2-type CoO_2 layer with two different periodicities b_1 and b_2 along the b axis, respectively [112]. The perceived mixed ionic and electronic conductivity of this material originating from the electronic conduction in CoO_2 blocks and ionic conduction in rock-salt blocks has been initially demonstrated by Nagasawa et al. [110]. Electrochemical tests on symmetrical cells at 700°C in air showed a very high electrode polarization resistance, R_p, of 4 Ω cm^2 for the 40 μm thick layers. This was, however, improved with the addition of 30 wt % CGO leading to an $R_p \sim 1$ Ω cm^2 [110]. Continuous work by Rolle et al. [111] has focused on cathode processing optimization in order to decrease the cathode polarization resistance. While some interesting findings such as the effects of sintering temperatures and including various current collectors have been demonstrated in the said work, the R_p was still higher than those reported for common SOFC cathode materials such as LSCF in Refs. [105, 63, 106, 90] which have R_p values in the range 0.19 - 1 Ω cm^2 at 600°C in air depending on the LSCF volume fraction and the microstructure. Thus, there is still a need for new and improved cathode materials for IT-SOFCs.

This chapter discusses a study on the misfit-layered cobaltite $Ca_3Co_4O_{9+\delta}$ ($\delta > 0$) as a candidate material for SOFC cathodes. The effects of sintering conditions for the pure $Ca_3Co_4O_{9+\delta}$ cathode as well as the addition of CGO on the electrochemical performance were investigated in detail. Cathode symmetric cells were fabricated on a dense CGO electrolyte by screen printing followed by firing. The microstructure of the cathodes was analyzed by scanning electron microscopy while the polarization resistances at various temperatures were measured using electrochemical impedance spectroscopy.

6.2 Experimental

$Ca_3Co_4O_{9+\delta}$ was synthesized by solid state reaction. Precise amounts of $CaCO_3$ (99.5%, Johnson Matthey A/S) and Co_3O_4 (99.7%, Alfa Aesar) powders were mixed by ball milling with ethanol for 36 h. The resulting mixture was dried and then calcined at 950°C for 24 h in air. CGO/$Ca_3Co_4O_{9+\delta}$ composites were prepared by adding commercially available $Ce_{0.9}Gd_{0.1}O_{1.95}$ (Rhodia). In this study, pure $Ca_3Co_4O_{9+\delta}$ and two composite compositions, $Ca_3Co_4O_{9+\delta}$ mixed with 22 vol % of CGO (22CGO/$Ca_3Co_4O_{9+\delta}$)

and 50 vol % of CGO (50CGO/$Ca_3Co_4O_{9+\delta}$) were selected to compare with the reported investigations on the same and the state of the art materials e. g. LSCF. The 22 vol% CGO corresponds to about 30 wt % CGO, the composition reported by Nagasawa et al. [110] and Rolle et al. [111]. Also, with the increased amount of CGO up to 50 vol%, it is possible to have a comparative look on the difference in the electrochemical performance of 50CGO/$Ca_3Co_4O_{9+\delta}$ with that of the commonly used composite cathode in SOFCs - LSCF/CGO where the amount of CGO is 40-50 vol%. Composition calculations are based on the theoretical densities of $Ca_3Co_4O_{9+\delta}$ and CGO, 4.68 g cm^{-3} [112] and 7.29 g cm^{-3} [113], respectively. $Ca_3Co_4O_{9+\delta}$ and CGO/$Ca_3Co_4O_{9+\delta}$ composite inks consisting of powder-dispersant-binder mixture were prepared and screen printed onto both sides of a 5 x 5 cm^2, dense 290 μm thick CGO electrolyte (KERAFOL). The screen printed samples were sintered at 700, 850, 900 and 950°C in air for 2 h in order to determine the optimum sintering conditions. The resulting layer thickness after sintering is about 60 μm as determined from scanning electron microscope images.

Electrochemical measurements of the $Ca_3Co_4O_{9+\delta}$ and CGO/$Ca_3Co_4O_{9+\delta}$ composite cathodes were performed in air at various temperatures on square samples with an approximate size of 6 $\times$ 6 mm^2 by electrochemical impedance spectroscopy on symmetric cells using a Hioki impedance analyzer in the frequency range 70 mHz to 100 kHz under open circuit conditions with 50 mV amplitude AC signal. In all cases, Pt paste (Ferro GmbH) and Pt mesh were used for current collection. The impedance arising from the series inductance of the rig (80 - 100 nH), determined by measurements with samples removed was subtracted from the data. The measured data were normalized to the geometrical area of the cell and were divided by two to account for the symmetric structure of the cell. The microstructures of the cathodes were analyzed using a Zeiss Supra 35 scanning electron microscope (SEM). The powders and the deposited layers on dense CGO electrolyte were characterized using a Bruker D8 Bragg-Brentano diffractometer with Cu Kα radiation. The absolute oxygen content of the pure $Ca_3Co_4O_{9+\delta}$ powder was determined by iodometric titration. The titration method is based on dissolution of the sample (45-50 mg) in acidic solution (1 M HCl) and subsequent reduction of Co III and Co IV with I^- ions. The experimental details were as described in Ref. [112].

6.3 Results and Discussion

6.3.1 Phase and microstructure

Fig. 6.1 shows the XRD analysis of the as prepared powders and deposited layers. As showin in Figs. 6.1a and b, the pure material powder and deposited layer and show phase purity within the XRD detection limit corresponding to the JCPDS card PDF no. 21-0139 for $Ca_3Co_4O_{9+\delta}$ material. For the CGO/$Ca_3Co_4O_{9+\delta}$ mixture (Fig. 6.1c), no reaction products between CGO and $Ca_3Co_4O_{9+\delta}$ are found from the XRD patterns irrespective of the CGO content. This is in agreement with previous reports [110, 111]. The titration results for our prepared powder revealed that δ is determined to be 0.25. The misfit layered cobaltite can be more accurately described by the formula $[CoO_2]_{1.62}[Ca_2CoO_{3-x}]$, where the oxygen nonstoichiometry takes place in the rock-salt blocks [112]. Based on the titration measurements this formula can therefore be written as $Ca_3Co_4O_{9.25}$ which gives $[CoO_2]_{1.62}[Ca_2CoO_{2.93}]$. Shimoyama et al. [114] have shown that the smallest composition tolerated by this system is $Ca_3Co_4O_{9.15}$ corresponding to $x = 0.14$ in the formula $[CoO_2]_{1.62}[Ca_2CoO_{3-x}]$.

SEM images of fracture cross sections of $Ca_3Co_4O_{9+\delta}$ sintered at various temperatures are shown in Fig. 6.2. The areas examined were focused near the cathode layer - CGO electrolyte interface. It is clear from Fig. 6.2 that the morphology of the films changed with increasing sintering temperature from 700, 850, 900 to 950°C. For the film, which was sintered at 700°C, the morphology looks as if the grains have just begun to sinter, i.e. some large grains surrounding with many small ones, which are separated and poorly faceted (Fig. 6.2a). Moreover, it appears as if the adhesion between the dense CGO and the deposited layer is very poor as illustrated by the air gaps (Fig. 6.2a). Poor adhesion of the $Ca_3Co_4O_{9+\delta}$ to the CGO electrolyte when the sample was heated at 700°C was also clearly evidenced as the cathode layer delaminated when the symmetric cell was fractured. Interestingly, Nagasawa et al. [110] have reported a good adherence between CGO and $Ca_3Co_4O_{9+\delta}$ interface when the cathode layer is heated at a maximum of 700°C. The consequences of this disparity will be assessed in the following discussion on the electrochemical performance of the tested cells. With increasing sintering temperature e.g. to 850°C, the grains started growing forming a plate-like morphology (Fig. 6.2b). The evolution of the microstructure became more pronounced with increasing sintering temperature at 900°C (Fig. 6.2c) and 950°C (Fig. 6.2d). All investigated films exhibit a similar porous structure, and the films sintered

at 950°C show some lamella-like grains, particularly the grains at the region close to the substrate surface.

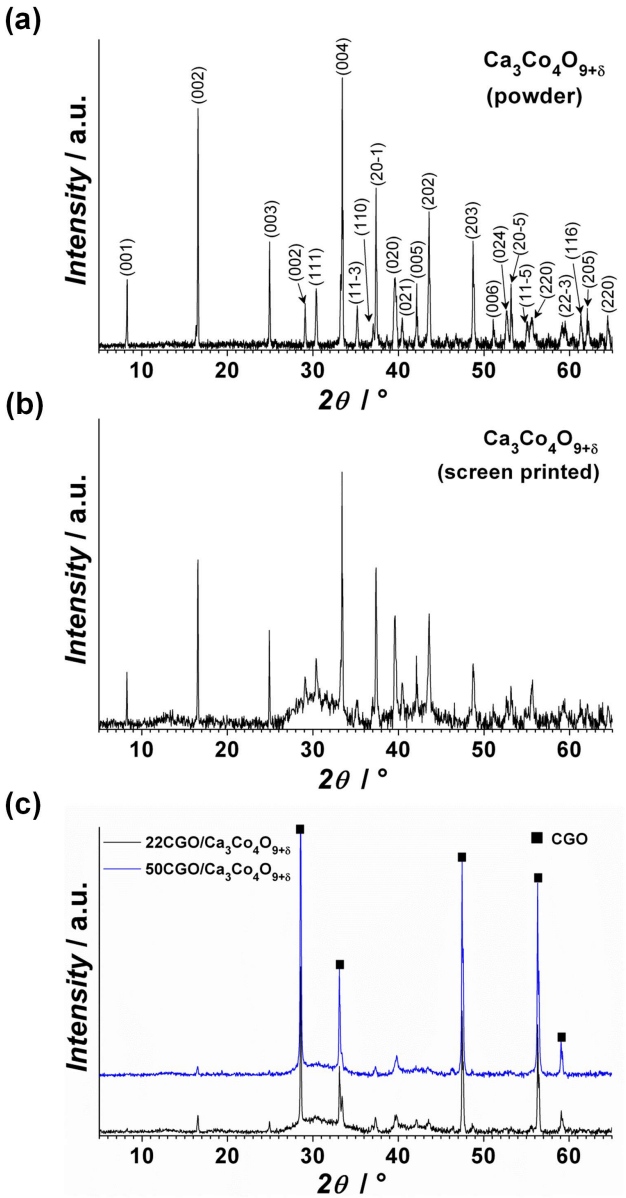

Figure 6.1: XRD patterns of (a) $Ca_3Co_4O_{9+\delta}$ powder (b)$Ca_3Co_4O_{9+\delta}$ cathode layer screen printed onto dense CGO electrolyte and (c) CGO/$Ca_3Co_4O_{9+\delta}$ composite cathode layer screen printed onto dense CGO electrolyte

In addition to the evolution of morphology, for the film sintered at 950°C, it seems that the $Ca_3Co_4O_{9+\delta}$ grains began to be sintered together forming a connective structure (Fig. 6.2d). This entails better connectivity compared to the samples sintered at lower temperatures. Good connectivity is a necessity for efficient transfer of ions and electrons. It is important to note that only those heated at 950°C were tested since the adhesion to the dense CGO electrolyte of the other samples sintered at lower temperatures was insufficient to allow them to be mechanically cut. No suitable sample sintered below 950°C was left for testing due to extensive delamination.

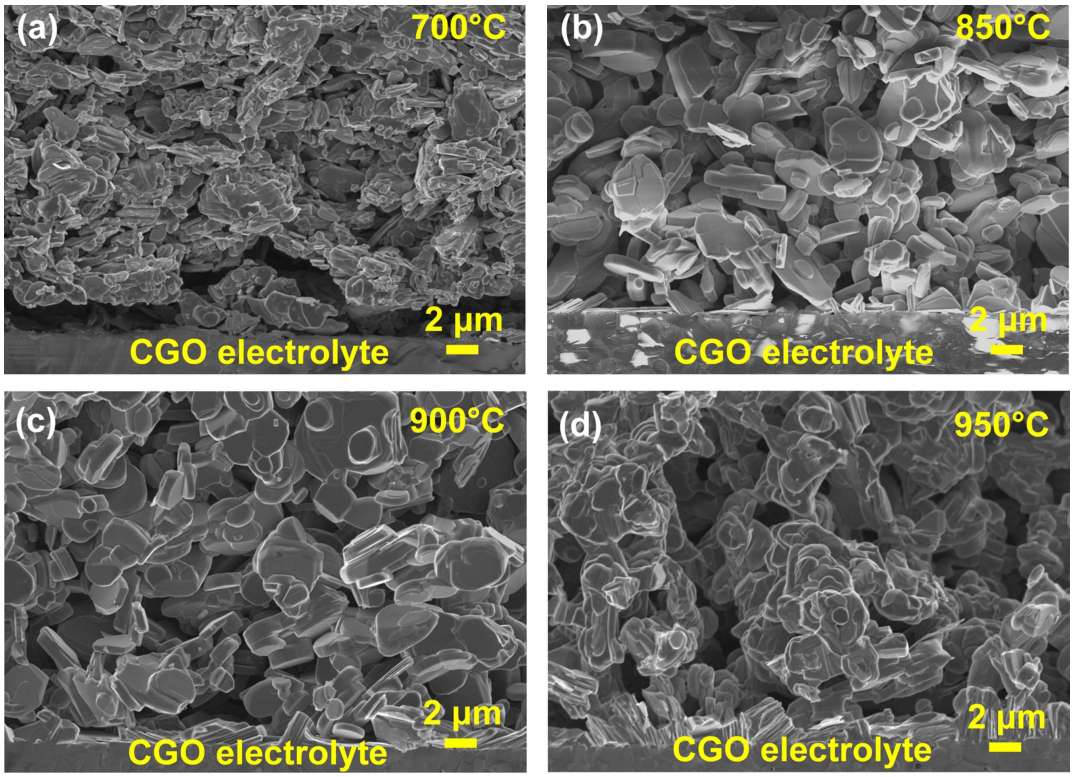

Figure 6.2: SEM micrographs of the fractured cross sections of $Ca_3Co_4O_{9+\delta}$ layer screen printed on the dense CGO electrolyte and sintered at various temperatures. (a) 700, (b) 850, (c) 900, and (d) 950°C.

Figs. 6.3 (a) and (b) show SEM micrographs of the fractured surfaces of the 22CGO/$Ca_3Co_4O_{9+\delta}$ and 50CGO/$Ca_3Co_4O_{9+\delta}$ composites sintered at 950°C, respectively. In both cases the CGO grains are about 200 nm in diameter and are covering the surface of the $Ca_3Co_4O_{9+\delta}$ network. For the 22CGO/$Ca_3Co_4O_{9+\delta}$, a large number

of CGO grains end up as isolated particles in the $Ca_3Co_4O_{9+\delta}$ network (Fig. 6.3a). If the amount of CGO is larger, i. e. in the case of 50CGO/$Ca_3Co_4O_{9+\delta}$, (Fig. 6.3b), the CGO grains form a more continuous network. This structure is preferred as the oxide ions can be transported in the CGO phase without a significant associated increase in the polarization resistance.

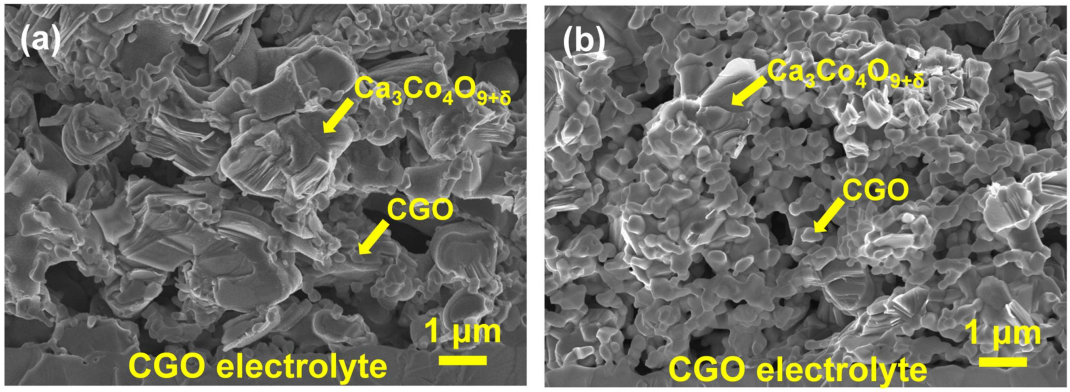

Figure 6.3: SEM micrographs of the fractured cross sections of (a) 22CGO/$Ca_3Co_4O_{9+\delta}$ and (b) 50CGO/$Ca_3Co_4O_{9+\delta}$ deposited on the dense CGO and fired at 950°C. $Ca_3Co_4O_{9-\delta}$ and CGO grains are labeled.

6.3.2 Electrochemical performance

The complex plane plots at 600 and 700°C in air of the symmetric cells of pure $Ca_3Co_4O_{9+\delta}$ and CGO/$Ca_3Co_4O_{9+\delta}$ composites are shown in Fig. 6.4. We have adopted the equivalent circuit model previously reported by Nagasawa et al. [110] with the inductance subtracted to fit the impedance spectra. The series resistance, R_s, consists of mainly the electrolyte resistance with additional contributions from the interfacial resistance at the electrode/electrolyte and electrode/current collector interfaces. The cathode polarization resistance,R_p, consists of the resistance, W_R, associated with the high frequency electrode response represented by a Warburg element, and R_1 associated with the low frequency electrode response represented by a constant phase element (Q). No attempt was made to attribute the equivalent circuit elements to their respective electrode process. Nagasawa et al. [110] have provided explanation on the designation of the circuit elements to the corresponding electrode processes. The present data, however, is insufficient to verify the claims of the said work. The total

value, R_p, is only used to compare with previous works.

The shape of impedance arcs in Fig. 6.4 of the composite materials seems to remain similar to that of pure $Ca_3Co_4O_{9+\delta}$. This suggests that the addition of CGO affected both the high and low frequency processes associated with the electrode. In a SOFC cathode, oxygen reduction is generally perceived to be confined close to the electrode/electrolyte interface, where the gas has simultaneous access to both the electronically and ionically conductive phases [9]. It is conceivable that the addition of CGO mainly extended this electrochemical reaction zone from the electrode/electrolyte interface. At 600°C, The addition of 22 vol % CGO to $Ca_3Co_4O_{9+\delta}$ decreased R_p from 12.4 Ω cm^2 for the pure $Ca_3Co_4O_{9+\delta}$ to 2.63 Ω cm^2. Particularly, R_p was further reduced to 0.64 Ω cm^2 with the addition of 50 vol % CGO in the case of the 50CGO/$Ca_3Co_4O_{9+\delta}$. This reduction in R_p could be attributed to the formation of a CGO network that conducts oxide ions with a very low resistance. In the case of 22CGO/$Ca_3Co_4O_{9+\delta}$, it can be clearly seen that the amount of CGO was insufficient to promote connectivity among the CGO phase in the entire electrode. It is important to note that even with this amount, the decrease in R_p of the pure material was significant. It is highly probable that although many of the CGO particles are disconnected within the electrode structure, some of the CGO phase near the electrolyte could still be percolated up to a certain length inside the electrode structure. These high ionic conducting percolated areas serve to increase the electrochemical reaction zone and enhance the oxide ion transport towards the electrolyte thus decreasing the R_p. With further addition of CGO, a point will be reached such that the entire CGO phase in contact with the $Ca_3Co_4O_{9+\delta}$ is percolated in the entire electrode structure. In this case, the sites for oxygen reduction reaction are more available thereby decreasing R_p. This is most likely the case in 50CGO/$Ca_3Co_4O_{9+\delta}$.

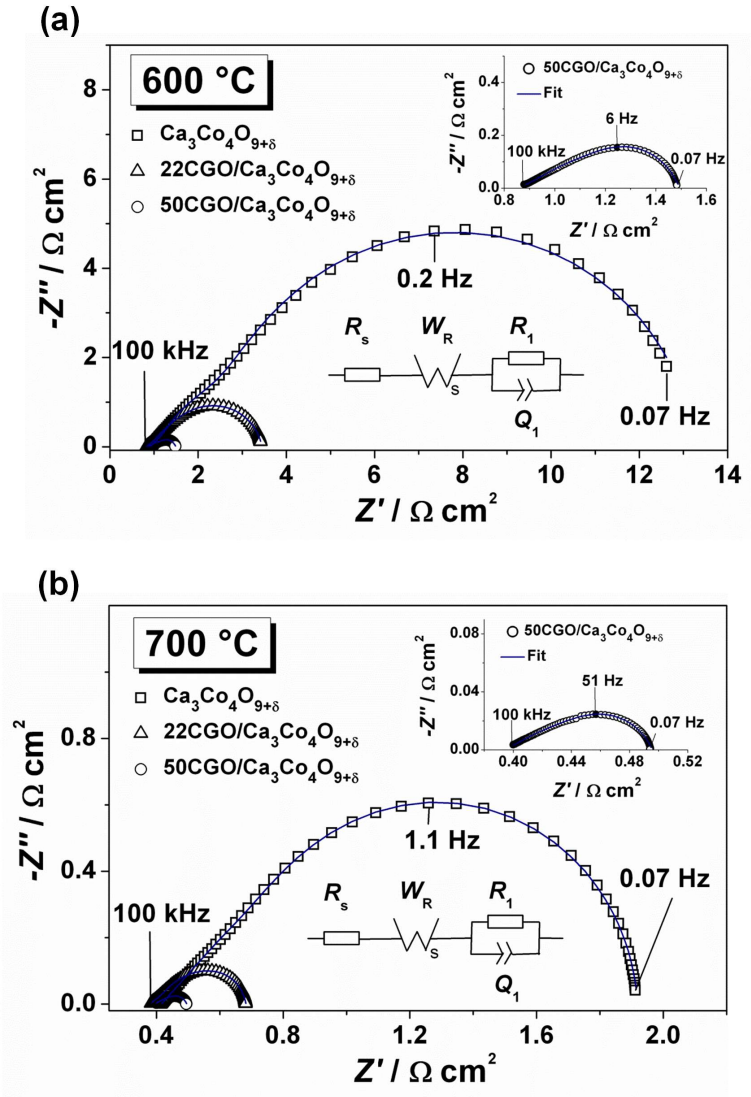

Figure 6.4: Complex plane plots at (a) 600 and (b) 700°C in air of the symmetric cells of pure $Ca_3Co_4O_{9+\delta}$ and $CGO/Ca_3Co_4O_{9+\delta}$ composites. The insets show the impedance spectra of the $50CGO/Ca_3Co_4O_{9+\delta}$. The equivalent circuit models to fit all the data are also shown. The solid lines are the fit. The lowest frequency data points correspond to 0.07 Hz.

The measured polarization resistances in air plotted against inverse absolute temperature are shown in Fig. 6.5. Data from previous works are also plotted for com-

parison. The activation energy of the pure $Ca_3Co_4O_{9+\delta}$ was determined to be about 1.50 eV, which is in good agreement with the previous investigation in this family of materials [110]. The activation energy was only lowered to 1.31 eV with the addition of 50 vol % CGO. The key results from this study are the remarkable performance compared to that of previous work and the promising R_p values obtained. The difference in R_p values at 600°C of the present study from that of the work of Nagasawa et al. [110] for the pure $Ca_3Co_4O_{9+\delta}$ is about a factor of two and about a factor of three for the 22CGO/$Ca_3Co_4O_{9+\delta}$. These results also indicate that the microstructure and processing are important parameters when preparing electrodes with this material. The measured R_p values for the 50CGO/$Ca_3Co_4O_{9+\delta}$ can be compared to the standard SOFC cathodes, particularly LSCF-CGO composite cathodes, although it is understood that it is not entirely correct to compare cathodes of different (or even the same) materials with different microstructures. R_p only serves as a measure of performance. The R_p value of 0.64 Ω cm^2 for 50CGO/$Ca_3Co_4O_{9+\delta}$ at 600°C is an order of magnitude lower than the values reported in Ref. [110]. The value is comparable to the composition 36CGO/LSCF (<1 Ω cm^2 at 590°C) reported by Dusastre and Kilner [105] but higher than the 50CGO/LSCF (0.33 Ω cm^2 at 600°C) reported by Murray et al. [63]. The lowest reported R_p values for an LSCF-CGO composite are those by Wang and Mogensen [106] for the composition 47CGO/LSCF (0.19 Ω cm^2 at 600°C) which are also shown in Fig. 6.5 for comparison. Certainly, the CGO/$Ca_3Co_4O_{9+\delta}$ composite cathode is open for optimization. This study only demonstrates a significant step in processing route that can be adopted in making the $Ca_3Co_4O_{9+\delta}$ material a viable cathode for IT-SOFCs.

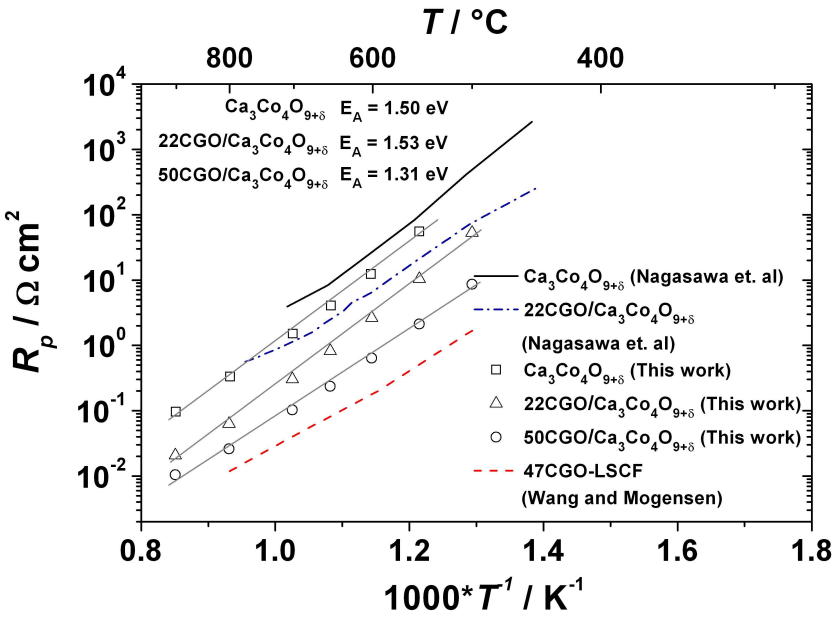

Figure 6.5: Polarization resistance (R_p) as a function of the reciprocal absolute temperature and the corresponding activation energies (E_A) for all the symmetric cells tested in air. Data from Nagasawa et al. [110] of the same material and data from Wang and Mogensen [106] for the 47 vol % LSCF-CGO cathode are also shown for comparison.

For the pure $Ca_3Co_4O_{9+\delta}$ and the 22CGO/$Ca_3Co_4O_{9+\delta}$, the sintering temperature is most likely the main difference between the present study and that of Nagasawa et al. [110] (or Rolle et al. [111]). Although low sintering temperature is usually preferred for grain size reduction/surface area maximization, it should not be low such that the adhesion and connectivity between grains is compromised. Examination of the SEM micrographs in Fig. 1 showed that sintering the $Ca_3Co_4O_{9-\delta}$ layer at 950°C may have not only enhanced the adhesion of the $Ca_3Co_4O_{9+\delta}$ to the CGO electrolyte but also promoted a well sintered structure that entails connectivity of the $Ca_3Co_4O_{9+\delta}$ grains. We speculate that this sintering temperature might already be the optimum for this cathode system since sintering at higher temperatures, e.g. 1000°C, promotes the decomposition of $Ca_3Co_4O_{9+\delta}$ into $Ca_3Co_2O_6$ which has significantly lower electronic conductivity than the parent phase [115].

A way to examine the quality of the electrode/electrolyte and electrode/current collector interfaces is through the R_s. From the reported values of CGO electrolyte conductivity [43], we have calculated R_s and compared it with the experimental values

as shown in Fig. 6.6. In all the cases, the R_s values are only slightly higher than the calculated values of resistance from a 290 μm CGO suggesting that sufficient adhesion and connectivity between the CGO grains was attained.

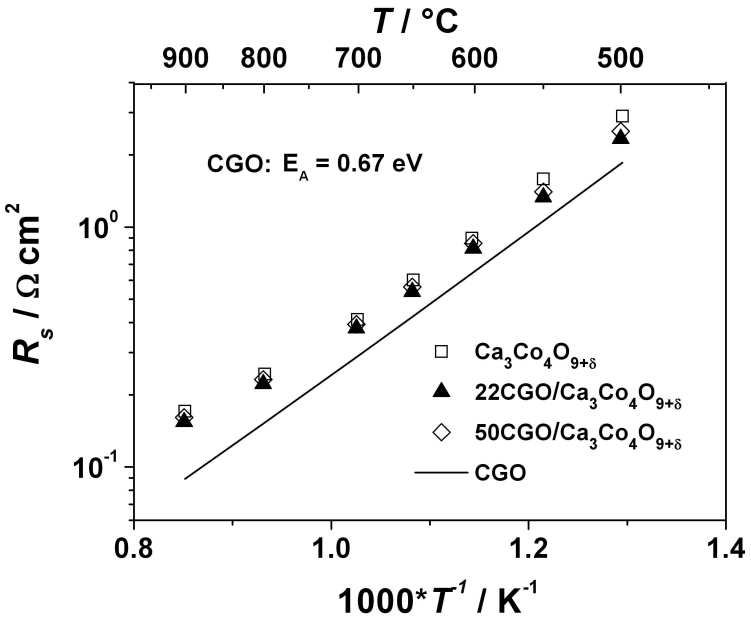

Figure 6.6: Series resistance (R_s) as a function of the reciprocal absolute temperature for all the symmetric cells tested in air. The straight line represents the calculated series resistance of a 290 μm CGO electrolyte [43].

6.4 Summary

Pure $Ca_3Co_4O_{9+\delta}$ and CGO/$Ca_3Co_4O_{9+\delta}$ composite cathodes with enhanced electrochemical performance are presented as viable candidates for an IT-SOFC cathode. By improving the processing conditions, specifically by optimizing the sintering temperature of the screen printed layers, the present $Ca_3Co_4O_{9+\delta}$ based cathodes show a significant improvement comparing to that of previous works reported on the same material. The sintering temperature at 950°C resulted in a well adhering cathode layer into the CGO electrolyte with well connected grain microstructure. Notably, the addition of 50 vol % CGO to $Ca_3Co_4O_{9+\delta}$ resulted in a remarkable reduction of R_p to about 0.64 Ω cm^2 which is the lowest value reported so far for this family of materials. The excellent performance is attributed the high ionic conducting CGO phase which extended the electrochemical reaction zone from the electrode/electrolyte inter-

face. These findings together with the reported thermal expansion match and chemical stability of $Ca_3Co_4O_{9+\delta}$ with CGO should encourage further work on this material.

Chapter 7

Modeling the performance of infiltrated cathodes[†]

7.1 Introduction

To develop cathodes, whether by conventional means, or as used extensively in this dissertation, by the infiltration method, is very costly and/or time-consuming. Moreover, the factors and processes which affect the electrochemical performance of cathodes are not fully understood. In this aspect, mathematical models are highly useful to predict the performance of electrodes from material properties and microstructure. Combined with reliable experimental data, modeling can be a powerful technique, as it allows one to perform full parametric variations including those which are impractical for experiments.

A considerable number of models that focus on porous composite electrodes for solid oxide fuel cells are already available in literature. Using simple electrode geometries, Kenjo et al. [116] and Tanner et al. [117] were able to predict the performance of porous composite cathodes with changing parameters and provide analytical expressions of the potential distribution in the composite electrode. Although insightful, these simplified models fail to address percolation in real composite cathodes and the effect of porosity on the gas diffusion. The percolation aspects have since then been addressed by several groups. Microstructural models which consider random packing, percolation limits, and triple phase boundary lengths of two types of spherical particles, typically LSM

[†]Co-authors: Martin Søgaard and Peter Vang Hendriksen.

and YSZ, are common [118, 119, 120, 121]. Most of these models also consider the gas transport in the porous structure of the composite electrode. These models generally recommend a small particle size for the electrocatalyst in order to increase the surface area or the triple phase boundary length, thus leading to the use of nanoparticles in electrodes.

In the case of infiltrated SOFC cathodes, several modeling studies based on simple geometries have also been developed. Bidrawn et al. [122] extended the work of Tanner et al. [117] to investigate rate limiting cases[†] in a dense, infiltrate material coating in SOFC cathodes prepared by infiltration. Although the model captures the essential features of adsorption and diffusion of oxygen into the infiltrate material, the applicability on infiltrated cathodes is limited to those only forming a dense thin film coating on the backbone. Consideration of the gas diffusion in the porous structure was also neglected. Using a simple surface resistance (SR) model, Shah et al. [123] were able to model and predict the R_{p} of an $La_{0.6}Sr_{0.4}Co_{0.2}Fe_{0.8}O_{3-\delta}$ infiltrated - $Ce_{0.9}Gd_{0.1}O_{1.95}$ (LSCF/CGO) cathode where the surface exchange kinetics dominate the cathode performance. The calculated polarization resistances were within 40% of reported values despite having only the LSCF area specific resistance and the total LSCF surface area as inputs. However, the model overlooks the ionic and electronic conductivity limitations of the components. Further, the gas transport was not considered.

This chapter presents a model that addresses the geometrical and material property aspects that affect the performance of infiltrated cathodes. The developed model is an extended version of the 1-dimensional microstructural model including gas diffusion proposed by Nam and Jeon [118] and Søgaard et al. [124] previously used for ionic conductor (IC)/electronic conductor or mixed ionic and electronic conductor (MIEC) composite cathodes prepared by conventional means. The present model takes into account the IC backbone with a modified description of the geometrical characteristics of the infiltrated MIEC material, which is distributed as a thin film with hemispherical caps (referred to hereafter as *thin coat model*). The gas transport in the porous structure is also taken into account by using the dusty gas model combined with a pressure driven flow. The effective ionic conductivities are calculated from the geometrical characteristics of the microstructure and the ionic conductivites of the constituent phases. The work is divided in several parts. In the first part, a conventional $La_{0.6}Sr_{0.4}CoO_{3-\delta}/Ce_{0.9}Gd_{0.1}O_{1.95}$ (LSC/CGO) composite cathode is analyzed using the binary sphere model [124] to extract an expression for the resistance associated with

[†]oxygen ion diffusion through the infiltrate film or reactive adsorption of O_2 at the infiltrate surface

oxygen reduction at the LSC surface, r_p. In the second part, the expression for r_p is used to model the LSC infiltrated CGO cathode discussed in Chapter 2, obtaining an expression for the total area specific polarization resistance associated with the electrode process, R_p, of the infiltrated cathode. A comparison is then made between the simulated and experimentally determined values of R_p. The findings are then discussed in terms of geometrical parameters and material properties. In the last part, the thin coat model is used to perform parameter variations with the goal of designing a high performance cathode.

7.2 Theory

The theory behind the model is based on random packing of spheres consisting of electronic or MIEC and IC particles has already been described by several authors, e.g. Nam and Jeon [118] and Søgaard et al. [124]. A short summary of the said models will be reproduced and extended here. The models will be used on a LSC/CGO composite cathode and modifications are applied to accommodate the observed microstructure in an infiltrated cathode. It is important at this point to make a distinction of the two composite systems that are modeled here. The LSC/CGO composite cathode prepared by conventional means (screen-printing) will be referred to as *conventional composite cathode* while the LSC infiltrated-CGO cathode will simply be referred to as *infiltrated cathode*. Figs. 7.1a and b show scanning electron micrographs of a fracture surface and polished cross sections of a conventional LSC/CGO composite cathode, respectively. Figs. 7.1c and d show scanning electron micrographs of a fracture surface and polished cross sections for that of the infiltrated cathode where the infiltrate is LSC (fired at 600°C), and the backbone is CGO, respectively. Figs. 7.1e and 7.1f show nominally identical samples but heated to 900°C. It is clear from the SEM micrographs that the nanoscale size of LSC electrocatalyst in the infiltrated cathode provides a much higher surface area for oxygen surface exchange than the conventional composite cathode. Further, it appears that the LSC in the infiltrated cathode coats the CGO backbone.

The corresponding illustration for both conventional composite and infiltrated cathodes are shown in Fig. 7.2. Fig 7.2a shows the corresponding schematic of the conventional composite cathode represented as random packing of spheres. Fig. 7.2b shows the geometry of contact, defined by the contact angle (θ_c) between two spheres with diameters d_{IC} and d_{MIEC}. The two spheres represent the particles of the ionic conducting (IC) phase and the mixed ionic and electronic conducting (MIEC) phase in contact.

The average microstructural properties are estimated using particle coordination number and percolation theory [125, 126, 127]. Depending on the volume fraction, the size of each phase, etc., the individual phases may form partial (presence of percolated clusters) or complete percolation. Fig. 7.2c shows a schematic for an infiltrated cathode. Unlike in the case of the conventional composite cathode, the IC phase forms complete percolation. In the case of the MIEC, it is clear from Fig. 7.1 that the microstructure may not be represented simply as an assembly of randomly positioned spheres. Instead, the MIEC can be better visualized as a corrugated covering for the IC particles. Fig. 7.2d simplifies this observed feature by representing the MIEC as a thin coating with attached spheres or hemispheres. One could infer, from this representation that the volume fraction of the MIEC that is needed to establish complete percolation can be much lower than in the case of the conventional composite cathode. This can be easily appreciated from simple geometrical considerations. Consider two spheres, IC and MIEC of equal diameters, $d_{\mathrm{IC}} = d_{\mathrm{MIEC}} = 500$ nm, enclosed in a fixed rectangular box. The volume fraction among solid volume is 50 vol % for each of the two phases. For an infiltrated cathode with $d_{\mathrm{IC}} = 500$ nm and MIEC coating with thickness, $t_{\mathrm{coat}} = 10$ nm, the volume fraction of the percolated MIEC coating among the solid volume is only 5.5 vol %. The volume fraction of the MIEC coating would change with the IC particle radius and thickness of the coating, but the resulting vol % of MIEC is, in realistic cases, always significantly lower than that of a conventional cathode. Indeed, there are experimental evidences that the infiltrated electrocatalyst material is still well connected even at loadings well below those necessary for percolation in random media [122, 123, 128]. In practice, the amount of MIEC can be increased to increase the available surface area for oxygen reduction. The increase in surface area is mainly due to the formation of nanoparticles. The resulting microstructure of the infiltrated MIEC will also depend on the infiltrate or backbone material and processing conditions such as the firing temperature but in general it can be described by the geometry shown in Fig. 7.2c. This peculiar configuration of the electrocatalyst particles, therefore, invalidates the direct use of percolation theory in an infiltrated cathode.

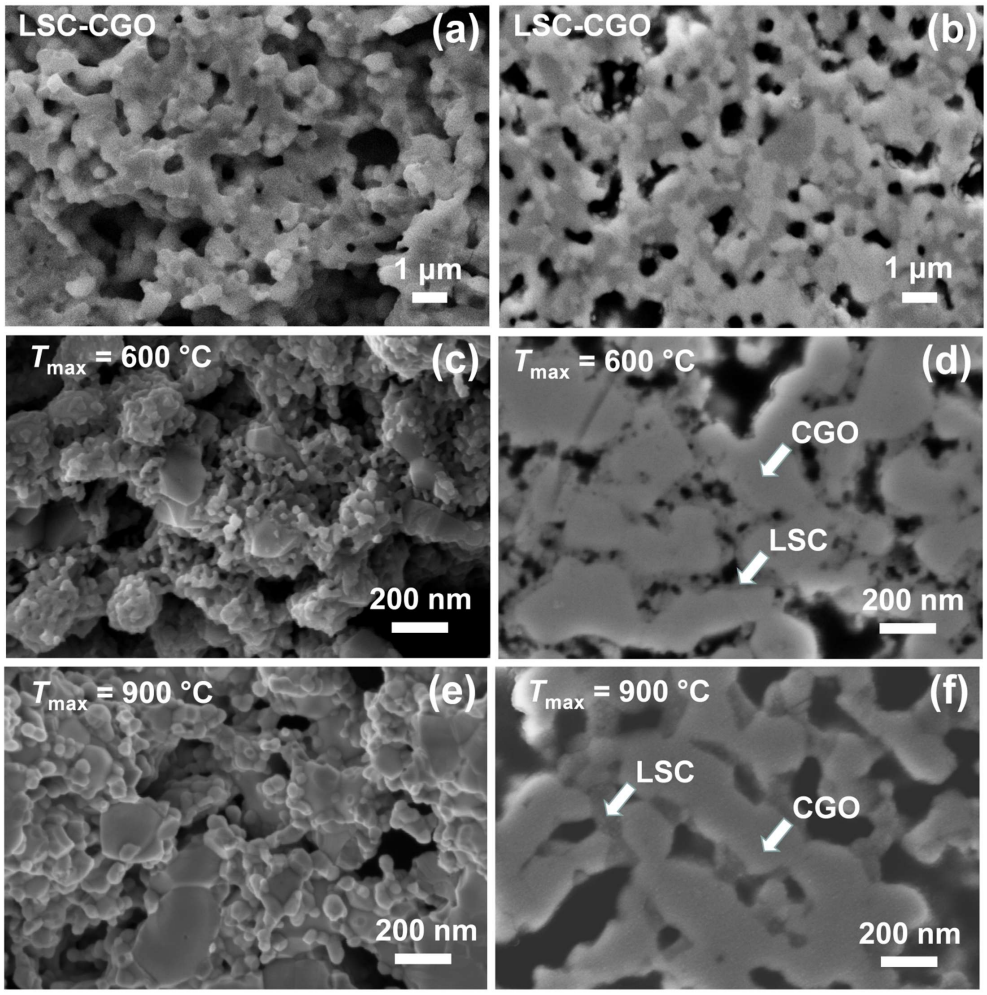

Figure 7.1: SEM micrographs of fractured and polished cross-sections of (a),(b) a conventional LSC/CGO composite cathode (c),(d) a CGO backbone infiltrated with LSC and fired at 600°C and (e),(f) a CGO backbone infiltrated with LSC and fired at 900°C. Corresponding phases are identified. Note the different scale used in (a) and (b) compared to (c), (d), (e), and (f).

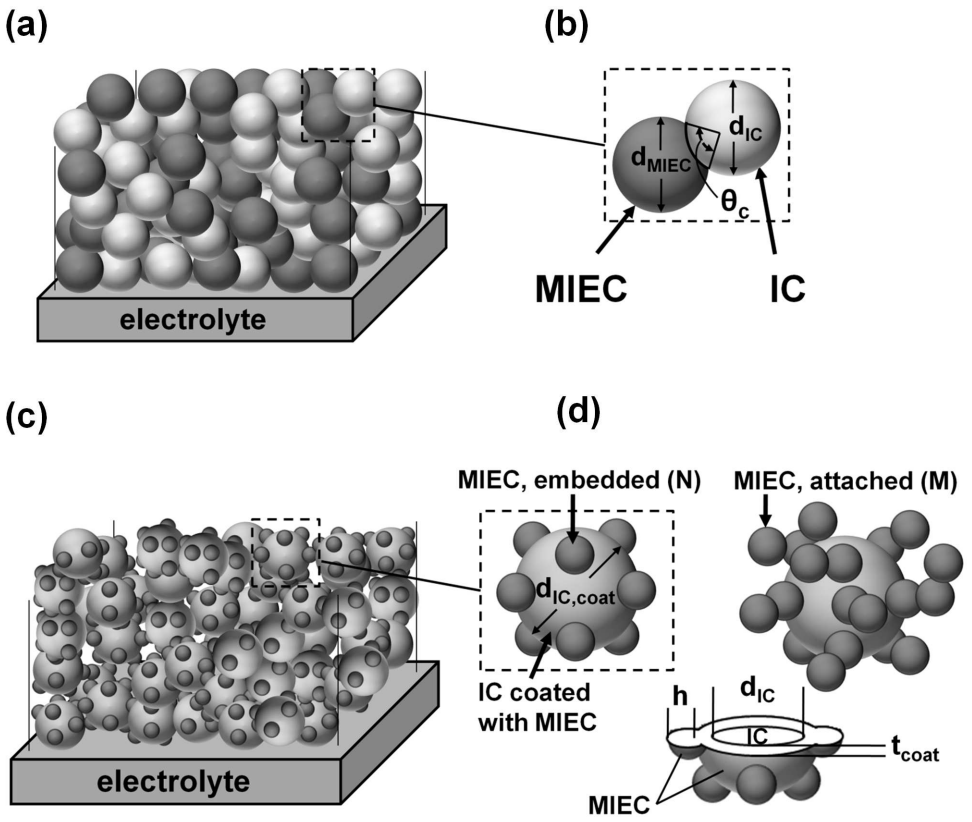

Figure 7.2: Schematic showing the microstructural models for a composite electrode and infiltrated electrode. (a) porous composite electrode represented as a random packing of binary spherical particles (b) magnified geometry of the MIEC/IC contact showing the diameters of the particles, d_{MIEC} and d_{IC}, and the contact angle, θ_{c} . (c) infiltrated electrode consisting of an IC backbone represented as a random packing of spherical particles and the MIEC infiltrate represented as a coating on the IC backbone with additional spherical caps. (d) magnified geometry of the MIEC coated IC particle showing the total diameter of the IC particle with the coating, $d_{\mathrm{IC,coat}}$, together with the sliced particle that shows the thickness of the coating, t_{coat}, and depth of embedding of the MIEC particle (referred to as N particle), h. A variation of the microstructure with additional MIEC particles attached (referred to as M particle) is also shown.

The geometrical description as shown in Fig. 7.2c and 7.2d are adopted for the modeling of the infiltrated cathodes. The infiltrated electrocatalyst is characterized by a thickness, t_{coat}, on the ionic conducting backbone. As seen in the SEM investigations,

LSC particles partly form a spherical cap with height, h, is added to the coat (called N particles). The very large size difference between the CGO particles and the LSC particles makes the spherical cap assumption adequate for modeling the infiltrated cathode. A variation of the microstructure of the infiltrated cathode is also shown in Fig. 7.2d. In this case, particles of LSC are attached to the coating (called M particles). This microstructure is commonly seen in cases of infiltrated cathodes with increased amount of electrocatalyst. Apparently, these particles provide additional surface area for oxygen exchange. The schematics in Fig. 7.2 serve as frameworks for the microstructure of the modeled cathodes.

The model formulation is divided into two parts. The first part deals with the composite cathode and follows the formulation described by Nam and Jeon [118] and Søgaard et al. [124]. The second part presents an extended geometrical formulation of the random packed spheres model to accommodate the microstructure of the infiltrated cathode. In both parts, the derivation of the microstructural parameters is presented first. The goal is to derive expressions for the surface area of the percolated part of the MIEC, the effective ionic conductivities of the MIEC and the IC phase, and the pore size which is used for gas transport calculations. This is followed by the mathematical formulation of diffusion through the porous structure. The last part in both cases describes the governing equations for the flow of mass and charged species in the cathode and the numerical procedures.

7.2.1 Binary sphere model

The cathode is modeled as a random packing system made up of mixed ionic and electronic conducting (MIEC) particles and ionic conducting (IC) particles with interstitial pores for transport of gas species. The number fraction of MIEC particles, n_{MIEC}, is determined as [126]

$$n_{\mathrm{MIEC}} = \frac{\alpha^3 \phi_{\mathrm{MIEC}}}{1 - \phi_{\mathrm{MIEC}} + \alpha^3 \phi_{\mathrm{MIEC}}} \tag{7.1}$$

where α is the ratio between the diameters IC to MIEC particles ($\alpha = d_{\mathrm{IC}}/d_{\mathrm{MIEC}}$) and ϕ_{MIEC} is the volume fraction of the MIEC phase (solid volume fraction). The number fraction of the IC particles, n_{IC}, can be found as $n_{\mathrm{MIEC}} = 1 - n_{\mathrm{IC}}$ and similarly $\phi_{\mathrm{MIEC}} = 1 - \phi_{\mathrm{IC}}$. The average total coordination number for MIEC particles is [126]

$$Z_{\mathrm{MIEC}} = 3 + \frac{Z-3}{n_{\mathrm{MIEC}} + (1-n_{\mathrm{MIEC}})\alpha^2} \tag{7.2}$$

and that for IC particles is

$$Z_{\mathrm{IC}} = 3 + \frac{(Z-3)\alpha^2}{n_{\mathrm{MIEC}} + (1-n_{\mathrm{MIEC}})\alpha^2} \tag{7.3}$$

where Z is 6 for the binary random packing of spheres. The coordination number between an i-phase particle and a j-phase particle, $Z_{\mathrm{i-j}}$, can be calculated as [126]

$$Z_{\mathrm{i-j}} = n_{\mathrm{i}} \frac{(Z_{\mathrm{i}} Z_{\mathrm{j}})}{Z} \tag{7.4}$$

Suzuki and Oshima [125] proposed the expression to calculate the probability of an i-phase belonging to a percolated network of the same phase as

$$P_{\mathrm{i}} = \left[1 - \left(\frac{4.236 - Z_{\mathrm{ii}}}{2.472}\right)^{2.5}\right]^{0.4} \tag{7.5}$$

which has zero probability at the percolation threshold ($Z_{\mathrm{ii}} \leq 1.764$). Conversely, $P_{\mathrm{i}} = 1$ if $Z_{\mathrm{ii}} \geq 4.236$. The effective conductivity of the i-phase, $\sigma_{\mathrm{i}}^{\mathrm{eff}}$, can be approximated as [118]

$$\sigma_{\mathrm{i}}^{\mathrm{eff}} = \sigma_{\mathrm{i}}^{0} \left((1-\epsilon)\, \phi_{\mathrm{i}} P_{\mathrm{i}}\right)^{m} \tag{7.6}$$

where σ_{i}^{0} is the bulk conductivity of phase i, ϵ is the porosity of the electrode, ϕ_{i} is the solid volume fraction of phase i, and P_{i} is the percolation probability. The exponent m is called the Bruggeman factor. This accounts for tortuous conduction pathways and is typically assumed to be 1.5 [118, 129]. The expressions used for the bulk ionic conductivities of the MIEC phase (LSC [92]) and the IC phase (CGO [43]) are listed in Table 7.1 while the microstructural parameters used in the model of conventional composite cathode are listed in Table 7.2. These parameters are estimated from scanning electron microscopy and FIB tomography performed by Jørgensen et al. [130, 131]. The volume fractions of LSC and CGO are known from the ink preparation.

Material	Ionic Conductivity / S m^{-1}	Reference
CGO	$\frac{1.34 \times 10^7}{T} \exp\left(-\frac{64799}{RT}\right)$	[43]
LSC	$\frac{4.26 \times 10^9}{T} \exp\left(-\frac{121659}{RT}\right)$	[92]

Table 7.1: Bulk conductivity expressions used in modeling the conventional composite cathode.

Parameter	Value
d_{LSC}	400 nm
d_{CGO}	800 nm
L_{C}	20 μm
ϵ	0.16
ϕ_{LSC}	0.52
ϕ_{CGO}	0.48
θ_{c}	30°

Table 7.2: Microstructural parameters used in modeling the conventional composite cathode.

Essential to the estimation of the polarization resistance is the surface area of the percolated part of the MIEC. The surface area of the percolated MIEC phase per unit volume, $A^{\mathrm{sp}}_{\mathrm{MIEC}}$, can trivially be calculated as

$$A^{\mathrm{sp}}_{\mathrm{MIEC}} = \frac{\pi d^2_{\mathrm{MIEC}}}{2}\left(2 - Z_{\mathrm{MIEC}}\left(1 - \cos\left(\frac{\theta_{\mathrm{c}}}{2}\right)\right)\right) n_{\mathrm{MIEC}} P_{\mathrm{MIEC}} N_{\mathrm{t}} \tag{7.7}$$

where N_{t} (#/m^3) is the number density of all particles given as

$$N_{\mathrm{t}} = \frac{1-\epsilon}{\left(\frac{\pi}{6}\right) d^3_{\mathrm{MIEC}}\left(n_{\mathrm{MIEC}} + (1 - n_{\mathrm{MIEC}})\alpha^3\right)} \tag{7.8}$$

In Equation 7.7, θ_{c} is the contact angle between MIEC and IC particles. A contact angle of 30° is usually assumed [118, 119, 121, 124] as this represents closely the physical situation after sintering of SOFC electrodes. The pore diameter, d_{p}, for the gas transport calculations, is set equal to the hydraulic diameter, d_{h}, which is expressed as

$$d_{\mathrm{h}} = \frac{4}{A_0}\frac{\epsilon}{1-\epsilon} \tag{7.9}$$

where A_0 is the specific surface area based on the solid volume expressed as

$$A_0 = \frac{6}{d_{\mathrm{MIEC}}}\frac{n_{\mathrm{MIEC}} + (1-n_{\mathrm{MIEC}})\alpha^2}{n_{\mathrm{MIEC}} + (1-n_{\mathrm{MIEC}})\alpha^3} \tag{7.10}$$

In the modeling, the cathode is divided into segments [118, 124] as shown schematically in Fig. 7.3 and the microstructural parameters discussed above are specified individually in each of these segments. Fig. 7.3 will be discussed in more detail when describing the governing equations. The model only considers a single composite electrode with a total thickness L_{C} divided into $i_{\max}$ elements. The partial pressures ($p_{\mathrm{O_2}}(gas)$, $p_{\mathrm{N_2}}(gas)$) outside of this cathode structure is constant. The modeling involves solving the transport equations for gaseous oxygen, oxide ions and electrons under the requirement of conservation of mass and charge. The expressions in Fig. 7.3 are described in the succeeding paragraphs.

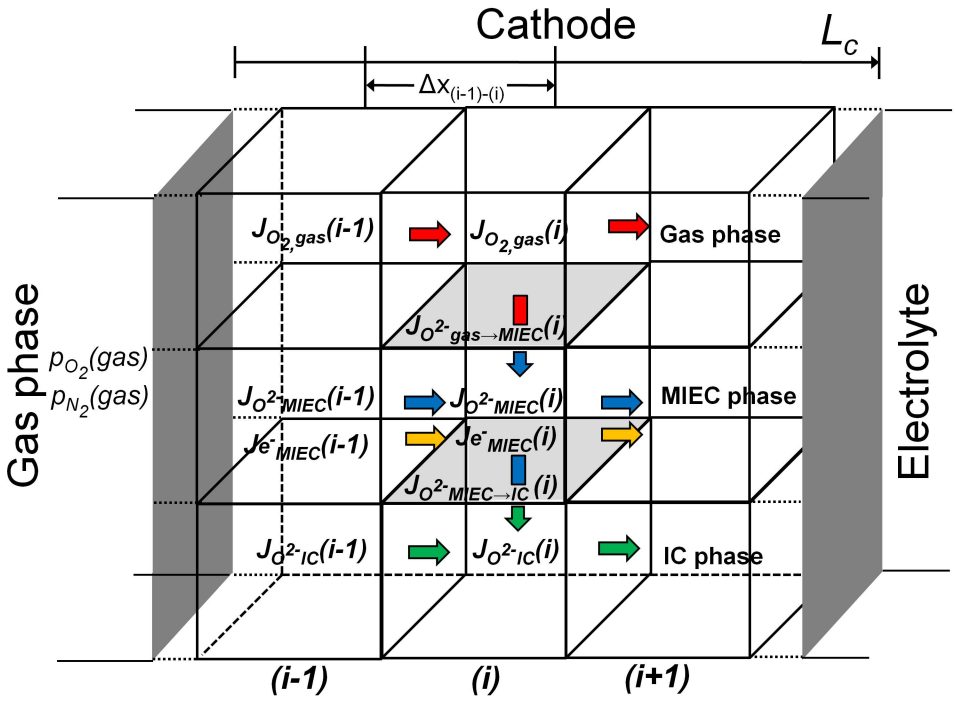

Figure 7.3: Schematic of the composite cathode showing the flux and conservation of ionic current and gas species between segments. The total thickness of the cathode is L_C. Note that due to the assumption of zero resistance associated with the transfer of oxide ions between IC and MIEC phase, the net flux $J_{O^{2-},MIEC\rightarrow IC}(i)$ can be reversed i. e. $J_{O^{2-},IC\rightarrow MIEC}(i)$ depending on the ionic conductivity of the materials.

Fig. 7.4 shows the equivalent circuit showing the resistances associated with the processes (surface exchange and transport of species) in each of the segments for the schematic shown in Fig. 7.3. The transport path of the species can be represented as rails where the O^{2-} rail is separated from the electron and gas phase rail by the surface exchange process represented by $r_{p,MIEC}$.

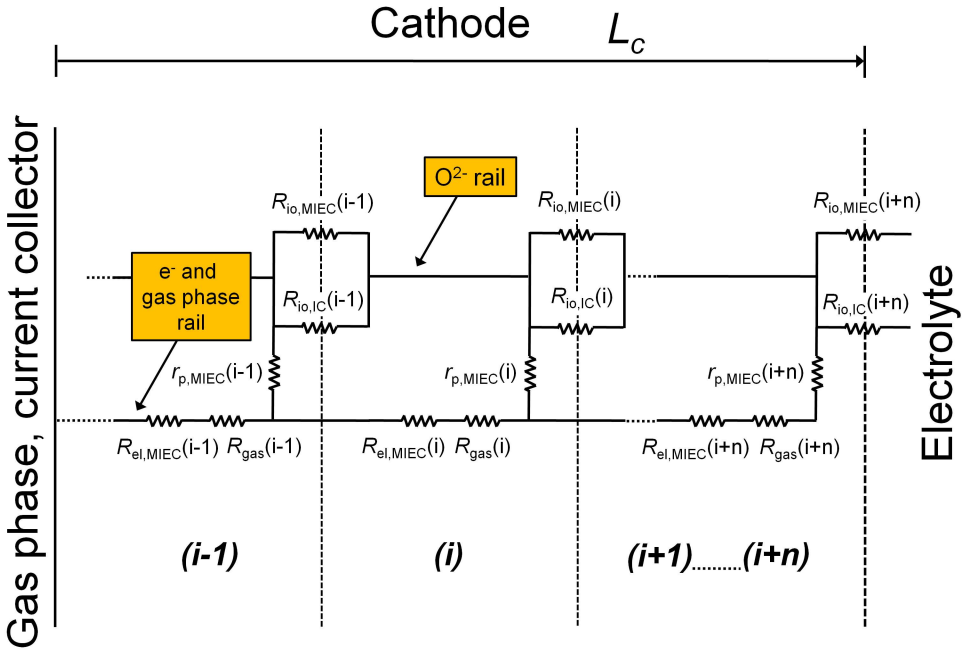

Figure 7.4: Illustration of the resistances associated with the different processes in the composite cathode.

The calculation of the diffusion through the porous structure uses the dusty gas model [132, 133] and the procedure follows that of Nam and Jeon [118] and similarly, that of Søgaard et al. [124]. The molar fluxes of oxygen, $J_{O_2}(i-1)$ (mol m^{-2} s^{-1}), and nitrogen, $J_{N_2}(i-1)$, from segment $(i-1)$ to segment (i), which are separated by the distance $\Delta x_{(i-1)-(i)}$ as shown in Fig. 7.3 in the gas phase component are calculated using the equations [118, 124]

$$J_{O_2}(i-1) = \frac{1}{RT}\left[\left(k_1 + k_2\frac{p_{O_2}(i-1)+p_{O_2}(i)}{2}\right)\frac{p_{O_2}(i-1)+p_{O_2}(i)}{\Delta x_{(i-1)-(i)}} + k_2\frac{p_{O_2}(i-1)+p_{O_2}(i)}{2}\frac{p_{O_2}(i-1)+p_{O_2}(i)}{\Delta x_{(i-1)-(i)}}\right] \quad (7.11)$$

$$J_{N_2}(i-1) = \frac{1}{RT}\left[\left(k_3 + k_4\frac{p_{N_2}(i-1)+p_{N_2}(i)}{2}\right)\frac{p_{N_2}(i-1)+p_{N_2}(i)}{\Delta x_{(i-1)-(i)}} + k_4\frac{p_{N_2}(i-1)+p_{N_2}(i)}{2}\frac{p_{N_2}(i-1)+p_{N_2}(i)}{\Delta x_{(i-1)-(i)}}\right] \quad (7.12)$$

It is important to note that in the steady state solution, the net molar flux of nitrogen between segments is zero as nitrogen is neither consumed nor produced. The constants, $k_1 - k_4$, in Equations 7.11 and 7.12 are given as

$$k_1 = \frac{D^{\text{eff}}_{O_2-N_2} D^{\text{eff}}_{O_2,K}}{D^{\text{eff0}}_{O_2-N_2} + D^{\text{eff}}_{O_2-N_2,K}} \quad (7.13)$$

$$k_2 = k_4 = \frac{1}{p_{O_2} + p_{N_2}} \frac{D^{\text{eff}}_{O_2,K} D^{\text{eff}}_{N_2,K}}{D^{\text{eff}}_{O_2-N_2} + D^{\text{eff}}_{O_2-N_2,K}} + \frac{\epsilon^3}{\kappa_K (1-\epsilon)^2 A_0^2 \mu_{O_2-N_2}} \quad (7.14)$$

$$k_3 = \frac{D^{\text{eff}}_{O_2-N_2} D^{\text{eff}}_{N_2,K}}{D^{\text{eff}}_{O_2-N_2} + D^{\text{eff}}_{O_2-N_2,K}} \quad (7.15)$$

where k_K is the Kozeny constant and is around 5 for a porous media made of spherical particles [118]. The average viscosity of the gases, $\mu_{O_2-N_2}$, is given as $\mu_{O_2-N_2} = \chi_{O_2}\mu_{O_2} + \chi_{N_2}\mu_{N_2}$, where χ_{O_2} and χ_{O_2} are the molar fractions of oxygen and nitrogen in the gas phase, respectively and μ_{O_2} and μ_{N_2} are the viscosities of oxygen and nitrogen, respectively. The effective binary diffusion, $D^{\text{eff}}_{O_2-N_2}$, is calculated as $D^{\text{eff}}_{O_2-N_2} = \epsilon/\tau D_{O_2-N_2}$. The tortuosity, τ, is set to 3 as this typically represents porous electrodes of SOFCs [134]. The binary diffusion coefficient for oxygen and nitrogen, $D_{O_2-N_2}$ (m^2/s), is obtained from [135]

$$D_{O_2-N_2} = \frac{0.0143 T^{1.75}}{p(1000 M_{O_2-N_2})^{1/2}\left[V_{O_2}^{1/3} + V_{N_2}^{1/3}\right]^2} \quad (7.16)$$

where T (K) is the absolute temperature, p (Pa) is the total pressure and $M_{O_2-N_2}$ is the average molecular mass defined as $M_{O_2-N_2} = 2(1/M_{O_2} + 1/M_{N_2})^{-1}$ where M_{O_2} and M_{N_2} (kg mol^{-1}) are the molecular weights of oxygen and nitrogen, respectively. V_{O_2}

and V_{N_2} are the diffusion volume for oxygen and nitrogen, respectively. The values, V_{O_2}=16.3 and V_{N_2}=18.5 are used according to the recommendation of Todd and Young [136]. At 600°C, the binary diffusion coefficient is 1.35 $\times$ 10^{-4} m^2 s^{-1}.

The mixture Knudsen diffusion coefficient, $D^{\text{eff}}_{O_2-N_2,K}$, in Equations 7.13-7.15 is defined as $D^{\text{eff}}_{O_2-N_2,K} = x_{O_2} D^{\text{eff}}_{N_2,K} + \chi_{N_2} D^{\text{eff}}_{O_2,K}$, where $D^{\text{eff}}_{i,K}$ for each species is defined as [118]:

$$D_{O_2-N_2} = \frac{\epsilon}{\tau} \frac{97}{2} d_p \sqrt{\frac{T}{1000 M_i}} \tag{7.17}$$

The Knudsen diffusion is significant when the pore size becomes comparable to the mean free path of a gas molecule. In this case, an additional mass transport resistance has to be taken into account from the collision between the gas molecules and the solid structure [137]. A typical value of mixture Knudsen diffusion coefficient for O_2 and N_2 using the parameters for an infiltrated cathode considered in this study is 6.71 $\times$ 10^{-6} m^2 s^{-1} at 600°C.

The calculation of the total polarization resistance, R_p, involves solving a system of equations derived from considerations of charge and mass transfer conservation as will be outlined in the succeeding paragraphs. As also shown schematically in Fig. 7.3, the reduction of gaseous oxygen at segment (i) generates oxide ions that will either be transported to the electrolyte in the MIEC phase or transferred to the IC phase. The conservation of oxide ions in the MIEC phase requires that the flux of oxide ions into segment (i), $J_{O^{2-},MIEC}(i)$, is equal to the sum of the flux of oxide ions coming from segment $(i-1)$, $J_{O^{2-},MIEC}(i-1)$, and the total flux of oxide ions that is generated in the segment (i) by reduction of gaseous oxygen, $J_{O^{2-},gas\rightarrow MIEC}(i)$, minus the flux of the ions transferred from the MIEC phase to the IC phase, $J_{O^{2-},MIEC\rightarrow IC}(i)$, in segment (i):

$$J_{O^{2-},MIEC}(i) = J_{O^{2-},gas\rightarrow MIEC}(i) + J_{O^{2-},MIEC}(i-1) - J_{O^{2-},MIEC\rightarrow IC}(i) \tag{7.18}$$

and similarly, for the conservation of oxide ions in the IC phase:

$$J_{O^{2-},IC}(i) = J_{O^{2-},MIEC\rightarrow IC}(i) + J_{O^{2-},IC}(i-1) \tag{7.19}$$

where $J_{O^{2-},IC}$ and $J_{O^{2-},IC}(i-1)$ are the flux of oxide ions in the (i) and $(i-1)$ segments, respectively. Thus, the total flux of oxide ions into segment (i) can be expressed as:

$$\begin{aligned} J_{O^{2-}}(i) &= J_{O^{2-},MIEC}(i) + J_{O^{2-},IC}(i) \\ &= J_{O^{2-},gas\rightarrow MIEC}(i) + J_{O^{2-},MIEC}(i-1) + J_{O^{2-},IC}(i-1) \end{aligned} \tag{7.20}$$

It is assumed that the transport of oxide ions from the MIEC phase to the CGO phase (or vice versa) has no associated resistance. The flux of oxide ions that is generated in segment (i) by the reduction of gaseous oxygen, $J_{O^{2-},gas\rightarrow MIEC}(i)$, is related to the current density in the volume segment (i), $i_{MIEC}(i)$, by the equation

$$J_{O^{2-},gas\rightarrow MIEC}(i) = -\frac{1}{2F} A_{MIEC}(i) i_{MIEC}(i) \tag{7.21}$$

where F is the Faraday constant, $A_{MIEC}(i)$ is the active surface area of the percolated MIEC in the segment (i) and can be expressed as $A_{MIEC}(i) = V(i)A^{sp}_{MIEC}(i)$ where $V(i)$ is the volume in the segment and $A^{sp}_{MIEC}(i)$ is the volume specific surface area of the percolated MIEC in the segment (i). $i_{MIEC}(i)$ can be expressed from the overpotential in the segment, $\eta(i)$, and the material specific polarization resistance in the segment, $r_{p,MIEC}(i)$ as

$$i_{MIEC}(i) = \frac{\eta(i)}{r_{p,MIEC}(i)} \tag{7.22}$$

The overpotential in segment (i) is given by

$$\eta(i) = \eta_{io}(i) - \eta_{el}(i) + \eta_{gas}(i) \tag{7.23}$$

where $\eta_{el}(i)$ and $\eta_{el}(i)$ are the electric potentials in the electronic (MIEC) and ionic phase, respectively, and $\eta_{gas}(i)$ is the gas concentration polarization. $\eta_{el}(i)$ in segment (i) is calculated as:

$$\eta_{el}(i) = \eta_{el}(i-1) + I_{e^-}(i-1)R_{el}(i-1) \tag{7.24}$$

where $I_{e^-}(i-1)$ is the electronic current transported from segment $(i-1)$ to segment (i). The resistance associated with this transport, $R_{el}(i-1)$, is given as

$$R_{\mathrm{el}}(i-1) = \sigma^{eff}_{\mathrm{el,MIEC}} \Delta x A_{\mathrm{C}}^{-1} \tag{7.25}$$

where Δx is the distance between the middle of segment (i) and segment $(i-1)$ and A_{C} is the unit area of the cathode. The electric potential in the ionic phase, η_{io}, is calculated the same way as 7.24:

$$\eta_{\mathrm{io}}(i) = \eta_{\mathrm{io}}(i-1) + I_{\mathrm{io^-}}(i-1) R_{\mathrm{io}}(i-1) \tag{7.26}$$

where $I_{\mathrm{io^-}}(i-1)$ is the equivalent current associated with the transport of oxide ions from segment $(i-1)$ to segment (i). $R_{\mathrm{io}}(i-1)$ is the resistance associated with the transport of oxide ions in the said segments. R_{io} is the equivalent resistance associated with the transport of oxide ions in both the IC and MIEC phases placed in parallel. It is important to note that due to the assumption of zero resistance in the transfer of oxide ions between the IC and MIEC phase, the probability of percolation, P_{IC}, in the calculation of the effective ionic conductivity using Equation 7.5 is set to unity. The gas concentration polarization in segment i is given by

$$\eta_{gas}(i) = \frac{RT}{4F} \ln \frac{p_{\mathrm{O_2}}(i)}{p_{\mathrm{O_2}}(gas)} \tag{7.27}$$

where $p_{\mathrm{O_2}}(gas)$ is the oxygen partial pressure outside the electrode structure. For SOFC cathode operation, $p_{\mathrm{O_2}}(i) < p_{\mathrm{O_2}}(gas)$, wherefore $\eta_{\mathrm{gas}}(i)$ is negative.

The numerical calculation starts by specifying the composition and microstructural inputs such as the volume fraction of components, particle sizes, porosity, tortousity, length of cathode, etc. The bulk conductivity of the IC and MIEC phases are also defined according to temperature. The cathode structure is divided into segments where the microstructural inputs are defined. The effective conductivities are then calculated using Equation 7.6 along with the specific surface area of the percolated MIEC, using Equation 7.7. Using these results, the resistance for the transport of electrons and oxide ions between segments are found. Before the iteration, the current that should pass through the electrolyte is specified. Iteration begins by guessing the overpotential in the segment which is closest to the electrode/gas interface. The current density in this segment is then calculated using Equation 7.22. The total current in the segment is then found and employed to calculate the electric potentials in the next segment using Equations 7.24 and 7.26. The calculated electrical potentials would then be used

to obtain the current in the segment. The procedure continues until the electrolyte is reached and a current through the electrolyte is determined. The iteration is followed by the estimation of the gas concentration polarization through the calculation the partial pressures in each of the segments using the flux Equations, 7.11 and 7.12. The whole iteration is repeated but the guessed overpotential now includes the gas concentration polarization. The procedure continues until convergence has been obtained. Typically, at least 100 segments are necessary to ensure accuracy of solution (1×10^{-3} Ω cm^2 for R_{p}).

7.2.2 Thin coat model

The IC backbone is modeled from a random packing of spherical particles as outlined in the composite cathode case. However, in this case, the volume fraction of the IC and the probability of percolation are set to unity. The effective ionic conductivity of the IC phase is then reduced to

$$\sigma_{\mathrm{IC}}^{\mathrm{eff}} = \sigma_{\mathrm{IC}}^{0}(1-\epsilon)^{1.5} \tag{7.28}$$

where σ_{IC}^{0} is the bulk ionic conductivity of the IC phase. The calculation of the resistance associated with the transport of electrons follows the geometrical considerations illustrated in Fig. 7.2c. The resistance is assumed to be ohmic, with electrons flowing through the coating only, which is approximated as a sheet with a cross sectional area, A_{coat}, expressed as

$$A_{\mathrm{coat}} = l_{\mathrm{coat}} t_{\mathrm{coat}} \tag{7.29}$$

where t_{coat} is the thickness of the coating and l_{coat} is the length of the coat parallel to the CGO electrolyte as depicted schematically in Fig. 7.5a. The length of the coat is expressed as

$$l_{\mathrm{coat}} = \pi d_{\mathrm{IC,coat}} \sin\frac{\theta_{\mathrm{c}}}{2} N_{\mathrm{t}} d_{\mathrm{IC,coat}} n_{\mathrm{IC}} P_{\mathrm{IC}} A_{\mathrm{C}} \tag{7.30}$$

where $d_{\mathrm{IC,coat}}$ is the diameter of the IC particle with additional coating ($d_{\mathrm{IC,coat}} = d_{\mathrm{IC}} + 2t_{\mathrm{coat}}$) and A_{C} is the geometric area of the cathode. P_{IC} and n_{IC} are set to 1. This equation is identical to that used to calculate the triple phase boundary length of the

electronic particles in contact with an electrolyte [118]. It is easy to see that Equation 7.29 overestimates the actual cross-sectional area of the coat to a certain degree. For example, a thickness of 10% of the radius of the IC particle gives an overestimation error of about 4.8 % compared to the exact area calculated by subtracting the area of the circle formed by cutting the IC sphere in half from the area of the circle of the IC sphere with the thickness added. The error drops considerably for thin coatings. Because of the very thin coatings considered here[†] and since it is difficult to know exactly the diameters of spheres sliced in a segment to be able to calculate an exact cross sectional area, Equation 7.29 is found sufficient to estimate A_{coat}.

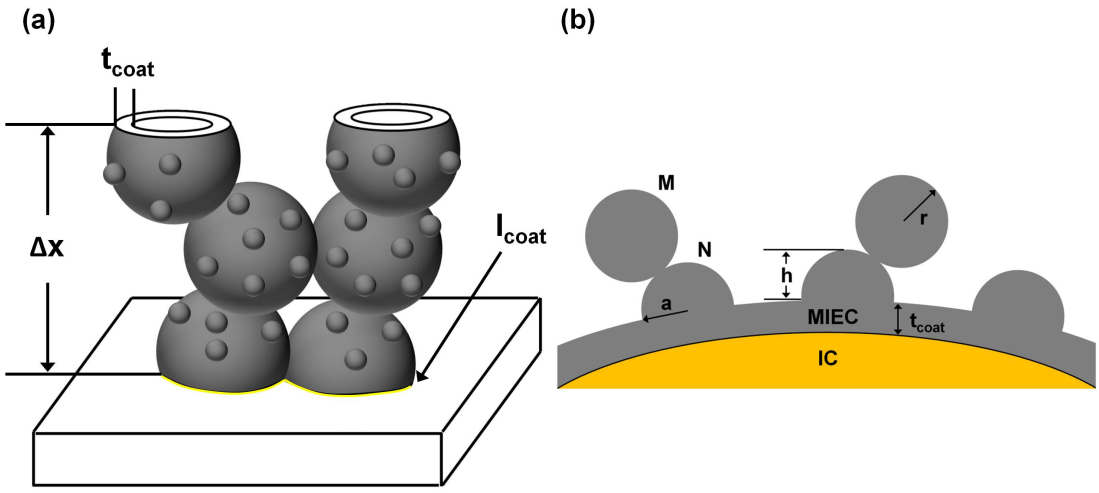

Figure 7.5: (a) Schematic depicting the parameters t_{coat} and l_{coat}. (b) Schematic depicting the geometry of infiltrated particles for calculation of the surface area factor. The case is shown for $N = 3$ spherical caps in the coat and $M = 2$ attached spherical MIEC particles. a is the base radius, r is the radius of the spherical MIEC particle and h is the spherical cap height. Δx is the distance between the middle of two segments as defined in Fig. 7.3.

The resistance associated with transporting electrons in the MIEC from segment $(i-1)$ to (i) can be expressed as

$$R_{\text{el,MIEC}}(i-1) = \frac{\tau \Delta x}{A_{\text{coat}} \sigma^0_{\text{el,MIEC}}} \tag{7.31}$$

[†]i.e. $d_{IC} \gg t_{coat}$ or $r_{IC} \gg t_{coat}/2$, where r_{IC} is the radius of the IC particle

where τ is the tortousity of the IC phase and $\sigma^0_{\text{el,MIEC}}$ is the bulk electronic conductivity of the MIEC phase. Similarly, the ionic resistance in from segment $(i-1)$ to (i) in the MIEC phase can be expressed as

$$R_{\text{io,MIEC}}(i-1) = \frac{\tau \Delta x}{A_{\text{coat}} \sigma^0_{\text{io,MIEC}}} \tag{7.32}$$

where $\sigma^0_{\text{io,MIEC}}$ is the bulk ionic conductivity of the MIEC phase. The calculation of the total ionic resistance is the same as that of the composite cathode case, where the IC and MIEC phase are placed in parallel only that Equation 7.32 is used for the MIEC phase. It is readily seen in Equation 7.31 that the thin coat model could not account for any loss of percolation as in the case of the binary sphere model. In actual electrodes, the coating may not be continuous throughout the whole cathode, thus the electronic path may be longer which increases the electronic resistance as defined in Equation 7.31. In theory, this contribution may be incorporated as a probability factor related to poor percolation. This is not defined in the present study. However, as will be seen in the discussion on the effect of the electronic conductivity of the infiltrate on R_{p}, it appears that this factor is not particularly significant for cathodes containing sufficient amount of electrocatalysts with high electronic conductivity.

In the calculation of the surface area of the percolated MIEC and the pore diameter, the thickness, t_{coat}, of the coating and the spherical caps together with the attached spheres are also taken into account as shown in Fig. 7.2d. The surface area, $A^{\text{particle}}_{\text{IC-MIEC}}$, of one IC particle with coating can be expressed in terms of the specific surface area of the IC backbone with coating over the number density of the IC particles,

$$A^{\text{particle}}_{\text{IC-MIEC}} = \frac{A_{\text{IC-MIEC}}}{N_{\text{t,inf}}} \tag{7.33}$$

where $A_{\text{IC-MIEC}}$ is the specific surface area of the CGO backbone with the added coating given as

$$A_{\text{IC-MIEC}} = \frac{\pi d^2_{\text{io,coat}}}{2} \left(2 - Z_{\text{IC}} \left(1 - \cos\left(\frac{\theta_{\text{c}}}{2}\right)\right)\right) n_{\text{IC}} P_{\text{IC}} N_{\text{t,inf}} \tag{7.34}$$

and where $N_{\text{t,inf}}$ is expressed as

$$N_{\mathrm{t,inf}} = \frac{1-\epsilon}{\left(\frac{\pi}{6}\right) d_{\mathrm{IC}}^3} \tag{7.35}$$

Since the only particles considered for the random packing are the IC particles, the following variables are set in Equation 7.34: $Z_{\mathrm{IC}} = 6$, $n_{\mathrm{IC}} = 1$, and $P_{\mathrm{IC}} = 1$. If the surface of one IC particle with coating is as shown in Fig. 7.5b, the increase in surface area with respect to $A_{\mathrm{IC-MIEC}}^{\mathrm{particle}}$, referred to as the surface area factor, s, can be expressed as

$$s = \frac{A_{\mathrm{IC-MIEC}}^{\mathrm{particle}} - N\pi a^2 + N2\pi rh + M4\pi r^2}{A_{\mathrm{IC-MIEC}}^{\mathrm{particle}}} \tag{7.36}$$

where N is the number of MIEC spherical caps on one IC particle (with coating), M is the number of spherical MIEC particles attached to the IC particle, a is the base radius, r is the radius of the spherical MIEC particle and h is the spherical cap height. For a hemispherical cap that is assumed in this study, Equation 7.36 reduces to

$$s = \frac{A_{\mathrm{IC-MIEC}}^{\mathrm{particle}} + N\pi r^2 + M4\pi r^2}{A_{\mathrm{IC-MIEC}}^{\mathrm{particle}}} \tag{7.37}$$

The maximum number of hemispherical caps that would fill the IC particle without overlapping is given by

$$N_{\mathrm{max}} = \frac{A_{\mathrm{IC-MIEC}}^{\mathrm{particle}}}{4r^2} \tag{7.38}$$

The calculation of the pore diameter follows accordingly. The pore diameter, $d_{\mathrm{p,inf}}$, in the infiltrated case is the same as Equation 7.9 but with $A_{0,\mathrm{inf}}$ expressed as

$$A_{0,\mathrm{inf}} = \frac{6}{d_{\mathrm{io,coat}}} + 2N_{\mathrm{t,inf}}N\pi r^2 + 4N_{\mathrm{t,inf}}M\pi r^2 \tag{7.39}$$

The calculation of the gas transport through the porous structure is identical to that of the composite cathode. Note that the porosity is also adjusted as the total volume of added hemispherical caps and spherical particles are added to the total volume of the electrode. The numerical procedure for the calculation of R_{p} is the same as the one outlined for the conventional composite cathode case.

The microstructural parameters used in modeling the infiltrated cathode are listed in Table 7.3. The radius of the LSC particles, r_{LSC}, and number of LSC particles (M or N) attached per CGO particle are estimated directly from the SEM images.

Parameter	Value
d_{CGO}	200 nm
L_{C}	25 μm
ϵ	0.59
τ	3
θ_{c}	30°
t_{coat}	5 nm
r_{LSC}	15 nm ($T_{\mathrm{max}} = 600°\mathrm{C}$)
	40 nm ($T_{\mathrm{max}} = 900°\mathrm{C}$)
N	125 ($T_{\mathrm{max}} = 600°\mathrm{C}$)
	10 ($T_{\mathrm{max}} = 900°\mathrm{C}$)
M	0

Table 7.3: Microstructural parameters used in modeling the infiltrated cathode.

7.3 Results and Discussion

7.3.1 LSC/CGO conventional composite cathode

In modeling the porous LSC/CGO composite cathode, the binary sphere model is used directly. Shown in Fig. 7.6 is the polarization resistance obtained from symmetric cells as a function of the reciprocal absolute temperature in air where the contribution originating from diffusion in a stagnant gas layer above the sample and the gas transport in the electrode have been subtracted for the LSC/CGO conventional composite cathode. To be able to subtract these contributions it was necessary to identify them from the impedance spectra of the LSC/CGO cathode. The identification was performed by fitting an equivalent RC circuit element to the low frequency arc in the impedance spectra that is sensitive to the change in oxygen partial pressures. Also shown in Fig. 7.6 is the best fit of the binary sphere model where the parameters listed in Table 7.1 and Table 7.2 have been used to generate the microstructure. The contribution originating from the gas transport in the electrode is excluded in the fitting. The diffusion in a stagnant gas layer above the sample and the gas transport in the electrode are

usually difficult to separate. Since the model can only describe the gas transport in the porous cathode and not the stagnant gas layer above the sample, the gas transport in the porous cathode is excluded altogether in the extraction of $r_{\mathrm{p,LSC}}$.

The expression for the resistance associated with oxygen reduction of LSC is defined in the present study as

$$r_{\mathrm{p,LSC}} = c_1 \exp\left(\frac{c_2}{RT}\right) \tag{7.40}$$

From the fitting with the gas transport subtracted, c_1 and c_2 are found to be 3.38 $\times$ 10^{-11} Ω m^2 and 1.32 $\times$ 10^5 J mol^{-1}, respectively.

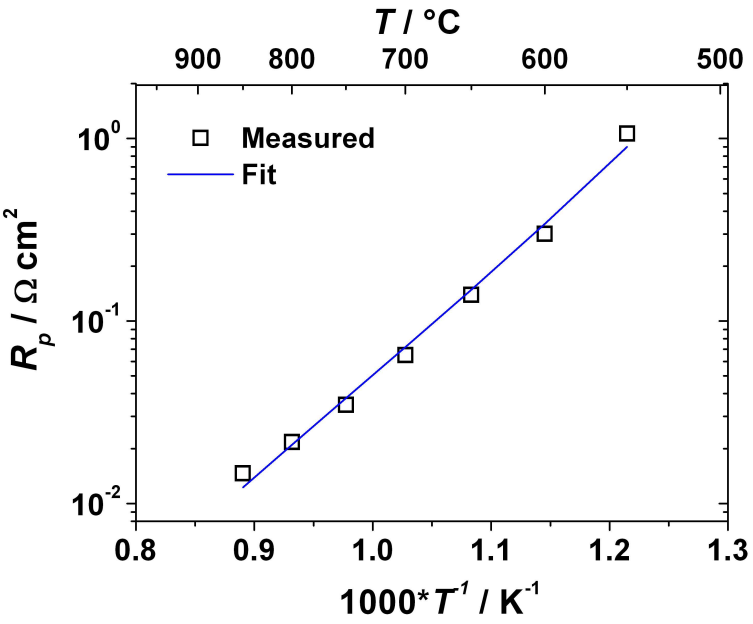

Figure 7.6: Measured polarization resistance, R_{p} (symbols), as a function of the reciprocal absolute temperature in air. The line shows the best fit using the binary sphere model.

The activation energy of 132 kJ mol^{-1} for the material specific polarization resistance in air obtained from the fitting is clearly within the range of 126 $\pm$ 10 kJ mol^{-1} which was deduced from polarization measurements performed by Baumann et al. [138] on thin dense films of LSC. It can be verified that the values of $r_{\mathrm{p,LSC}}$ calculated from Equation 7.40 are rather close to the lower limit values obtained by Baumann et al.

[138]. For example, at 750°C in air, Baumann et al. [138] finds $r_{p,LSC}$ in the range 4 - 8 Ω cm^2 while the corresponding value in this study is approximately 2 Ω cm^2. The discrepancy can be explained by several factors. One is the uncertainty in describing the microstructural paramaters of the electrode and the second is the uncertainty in comparing the surface composition of the LSC used in the porous composite cathode in this study and the LSC thin film deposited by pulsed laser deposition (PLD) in the study of Baumann et al. [138]. Kubicek et al. [139] have shown strong correlations between changes in electrode polarization resistance of oxygen reduction and surface composition. It is only pointed out here that a reasonable expression for the material specific polarization resistance can be obtained by employing a random binary sphere model.

It is important to note that the model can also accept as an input the expression for $r_{p,LSC}$. When the expression for $r_{p,LSC}$ derived from Baumann et al. [138] is used, it is found that although the activation energy of the experimental electrode polarization resistance R_p was accurate, the R_p values are overestimated by approximately a factor of two (for d_{LSC} = 400 nm) as shown in Fig. 7.7. It is possible to perform parametric variations to simulate the upper and lower limits of the parameters as observed in SEM and FIB tomography investigations. With $r_{p,LSC}$ fixed, it is possible to vary other parameters e. g. CGO and LSC grain diameter and porosity. It is found that a reasonable fit can only be attained by decreasing the LSC grain diameter to <200 nm as shown in Fig. 7.7 and that the other parameters within the uncertainty do not to a significant degree affect the calculated R_p. As this small predicted grain diameter of LSC is clearly inconsistent with the SEM investigation and FIB tomography, it is more likely that the discrepancy is due to the difference in the surface exchange characteristics of the LSC used in the composite cathode and that of the LSC thin film deposited by PLD. Thus, with careful consideration on the microstructure of composite electrodes and the bulk properties of the component materials, the binary sphere model is able to extract information on the surface characteristics of the electrocatalysts.

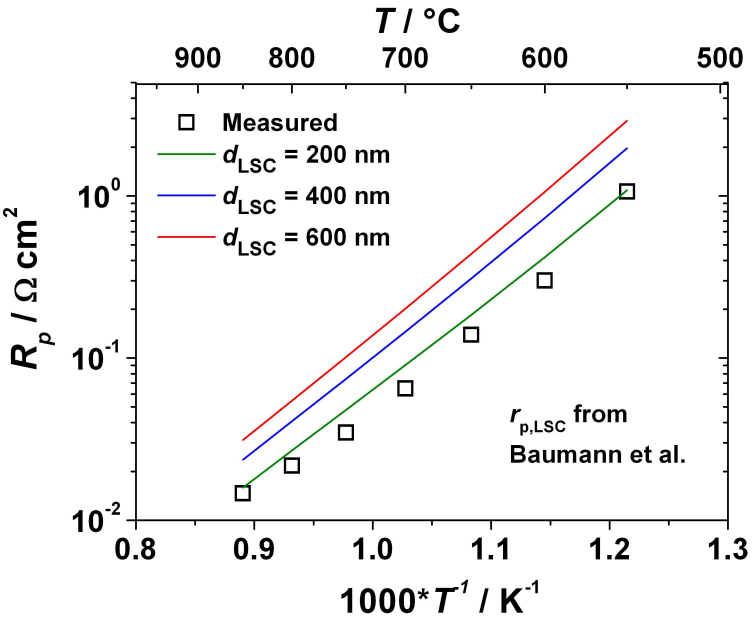

Figure 7.7: Polarization resistance, R_{p}, as a function of the reciprocal absolute temperature in air for different LSC diameters (d_{LSC}). Symbols show the measured R_{p}'s.The lines show the calculated values using the binary sphere model. The calculations use $r_{\mathrm{p,LSC}}$ from Baumann et al. [138].

7.3.2 Infiltrated cathodes

In the first step of modeling the LSC infiltrated cathodes, the extracted $r_{\mathrm{p,LSC}}$ from the random binary sphere model is used. In a later step, a fitting is performed to extract the $r_{\mathrm{p,LSC}}$ expression just as for the LSC/CGO composite case. The results obtained from each procedure are then discussed and compared. Due to the significant uncertainty associated with quantifying the microstructure of the infiltrated cathodes at different LSC firing temperatures, a series of parametric variations which tests the limits of each assumption put in the model is performed. In this a way, a more accurate picture of the microstructure and material property - performance relationship is obtained. It is important to consider that the "LSC" discussed here is multi-phased, as shown in Chapter 2. Thus, the surface exchange resistance extracted here is essentially that from a mixture of nanoparticulate electrocatalysts.

Infiltrated cathodes fired at 600°C

As the coating is essential to model the performance of infiltrated cathodes, the implications of this parameter to the estimation of R_p is first examined. Fig. 7.8 illustrates the effect of the thickness of the coating to the overall R_p, where the expression $r_{p,LSC}$ obtained from the fitting of the conventional composite cathode is used and the surface area factor, s, is set to unity, i.e. $N = M = 0$. The resistance due to gas transport is also not included in the calculation. The other parameters used in the calculation are listed in Table 7.3. The experimental R_p for the infiltrated cathode with the LSC infiltrate fired at 600°C is only shown as a reference. It is seen that the effect in thickness of the coating on R_p is only significant at high temperature (600°C). Further, it is seen that increasing the coating thickness decreases the overall R_p at high temperature consistent with equations 7.29 and 7.31. In the case of the infiltrated cathode studied here, although the actual thickness of the coating is difficult to establish, it is certain that it does not exceed 20 nm. As seen in Fig. 7.8, a physically meaningful assumption of the coating thickness in the range of 1-20 nm thick layer does not significantly affect the outcome of the calculation of R_p up to 600°C. This is intuitive considering the very high electronic conductivity of LSC combined with the large cross sectional area of the electronic path defined mainly by the considerable length as defined by l_{coat} in equation 7.29. The coating is assumed to be 5 nm in the remaining of the study.

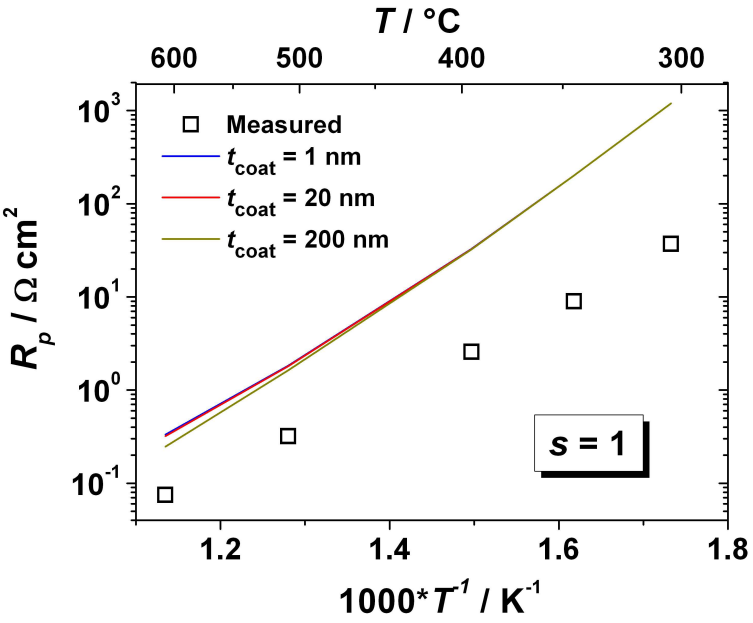

Figure 7.8: R_{p} as a function of the reciprocal absolute temperature in air for different LSC coating thickness (t_{coat}). Symbols show measured R_{p}'s. The lines show the calculated values using the thin coat model. The calculations use the $r_{\mathrm{p,LSC}}$ obtained from the LSC/CGO composite cathode. The surface area factor is set to unity.

Another important parameter to be considered in the thin coat model is the surface area factor, s. Fig. 7.9 shows the effect on R_{p} when varying the surface area factor. The expression for $r_{\mathrm{p,LSC}}$ from the fitting obtained in the LSC/CGO composite case is used and the parameters used to generate the microstructure are listed in Table 7.3. The gas transport is not included in the calculation. When s is set to unity, the calculated R_{p} values are about an order of magnitude higher than the experimental values. As s is increased, the calculated R_{p} values start to approach the experimental values. To obtain a reasonable agreement between the experimental and the calculated values, it can be seen that a surface area factor of 50 is necessary. In the case considered where the LSC spherical particles are embedded to half of their radius (15 nm), this corresponds to filling an entire particle of CGO with spherical caps of LSC without overlapping, with additional 1900 whole LSC particles attached to one CGO particle. Clearly, this is not consistent with the observations from SEM. The activation energy of the calculated R_{p} values (for $s = 50$) is also slightly higher (96 kJ mol^{-1}) than the activation energy of the measured values (85 kJ mol^{-1}). Thus, the excellent cathode performance of the LSC infiltrated cathode cannot be understood purely by geometrical considerations i.e., the

available surface area for oxygen surface exchange. A more probable explanation is that an improved oxygen surface exchange is at play. Interestingly, in the work of Dieterle et al. [54] on nanoscaled LSC prepared by dip coating, an improved oxygen surface exchange was also invoked after theoretical models with downscaled microstructure failed to explain the low R_p values that were obtained. It was speculated that the improvement in oxygen surface exchange was due to the presence of nanoparticulate Co_3O_4.

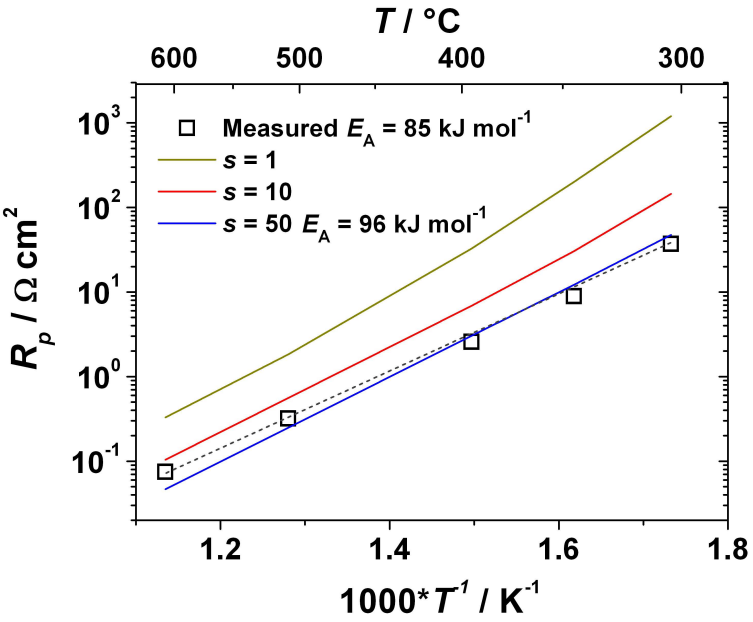

Figure 7.9: R_p as a function of the reciprocal absolute temperature in air for different surface area factors (s). Symbols show measured R_p's. The lines show the calculated values using the thin coat model. The calculations use the $r_{p,LSC}$ obtained from the LSC/CGO composite cathode.

Other parameters which might affect the calculation of R_p in the infiltrated cathode such as the diameter of the CGO and tortousity are also considered. Adjusting the tortousity to a worst/best (τ = 1-15) case does not affect the prediction of R_p. Decreasing the diameter of the CGO decreases the R_p due to an increase in surface area but as in the case of the surface area factor, the diameter of the CGO has be adjusted to very small values inconsistent with SEM observations.

The present model can also be used to extract information on the expression for the resistance associated with oxygen reduction of the LSC infiltrate material. Fig.

7.10 shows the polarization resistance, R_p, of the infiltrated cathode together with the best fit of the thin coat model where the parameters listed in Table 7.3 have been used to generate the microstructure. Like in the case of composite LSC/CGO cathode, the gas transport is excluded in the fitting. In the calculation of the surface area factor, s, the value for the number of LSC grains per CGO is fixed to 125 while the depth of the embedded LSC grain is 15 nm. The value of M in Equation 7.37 is set to zero. The value 125 represents the maximum number of spherical caps of LSC (N_{max}) with a base radius of 15 nm that will cover the entire CGO particle without overlapping. This corresponds to $s = 1.79$. It can be seen in Fig. 7.1c that these values provide adequate description to the microstructure. It should be mentioned that the LSC infiltrate is composed of several phases (see Chapter 2) and therefore it is very difficult to ascertain particles from each of the phases. It is assumed here that the infiltrated particles are homogeneous and that a representative value of r_p can be deduced. Using Equation 7.40 to describe the resistance associated with oxygen reduction in LSC in an infiltrated electrode, the following values are obtained: $c_1 = 5.80 \times 10^{-11}$ Ω m^2 and $c_2 = 1.10 \times 10^5$ J mol^{-1}. It is important to note that the activation energy obtained from the fitting is 110 kJ mol^{-1}, compared to 132 kJ mol^{-1} obtained from the fitting of the LSC/CGO composite cathode or from that of the thin film LSC from Baumann et al. [138] study. Thus, it is apparent that the multi-phased LSC obtained from infiltration has a significantly better surface exchange properties than the phase pure LSC used in the composite cathode. Note that the activation energy for the electrode polarization, 85 kJ mol^{-1}, is lower than the activation energy for oxygen reduction in LSC (110 kJ mol^{-1}) which points to the important role of ionic conduction in the electrode. The activation energy for R_p is a function of the activation energies for ionic transport in both CGO and LSC.

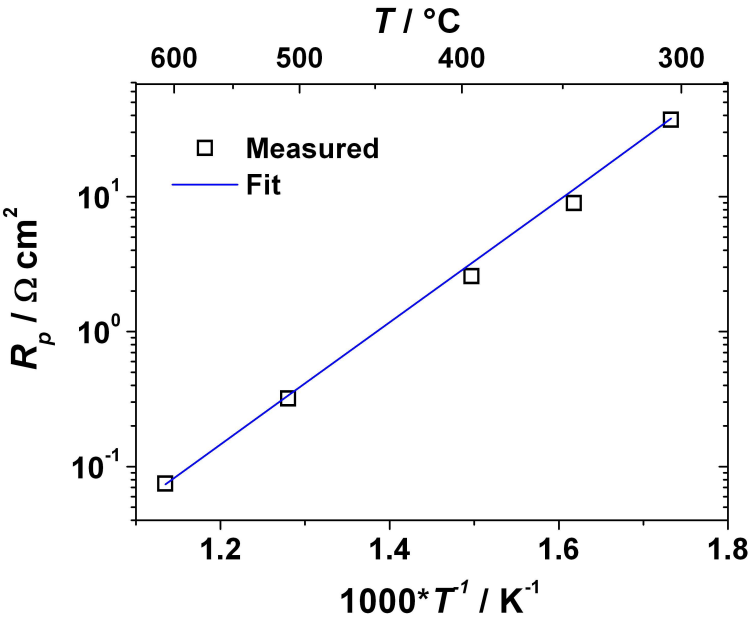

Figure 7.10: Measured polarization resistance, R_{p}, as a function of the reciprocal absolute temperature in air. The line shows the fit using the thin coat model. The LSC is fired at 600°C.

Infiltrated cathodes fired at 900°C

Fig. 7.11 shows the measured and calculated R_{p} using the thin coat model plotted against inverse absolute temperature for the infiltrated cathode but fired at 900°C. In the calculation, the expression of $r_{\mathrm{p,inf,600}}$ is used. The calculation of the surface area factor in the thin coat model assumes an average of 10 hemispherical LSC particles per CGO grain while the depth of embedding is set equal to the average radius of the LSC $h = r = 40$ nm based on the SEM imaging. The calculated surface area factor, s, is 1.45. Note that this value is lower than the calculated surface area factor of the LSC infiltrate fired at $T_{\mathrm{max}} = 600$°C.

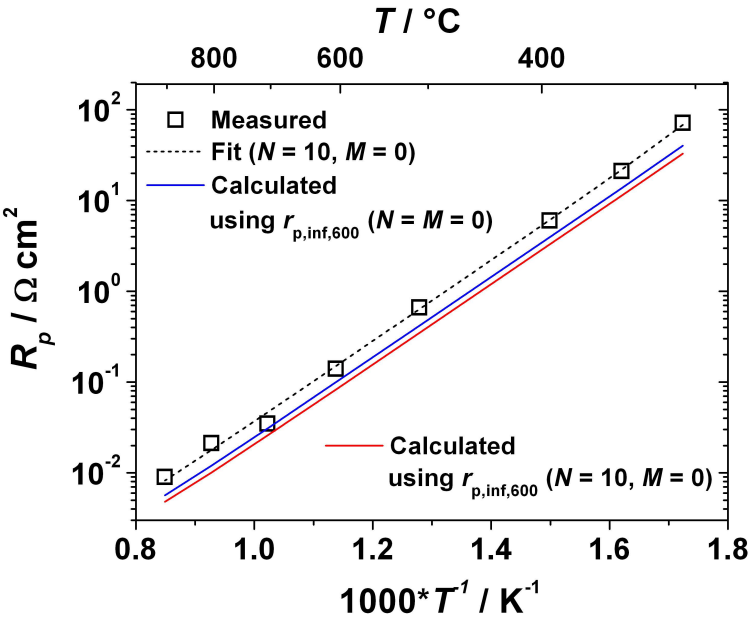

Figure 7.11: Measured polarization resistance, R_{p}, as a function of the reciprocal absolute temperature in air. The straight lines show the calculated R_{p}'s when $r_{\mathrm{p,inf,600}}$ is used. The dashed line is the fit. The gas transport is not included in the calculation.

It is seen from Fig. 7.11 that the calculated R_{p}'s are slightly lower than the experimental values suggesting that the infiltrate fired at 900°C have different surface exchange properties than the one fired at 600°C. This is plausible, considering the different phases that are formed when the LSC infiltrate is fired at different temperatures as seen in Chapter 2. To further verify that this is likely the case, the number of hemispheres, N, was varied in the model. As can be seen in Fig. 7.11, the R_{p} is still underestimated even when $N = 0$, i.e. no hemispheres are present to increase the overall surface area of the LSC electrocatalyst. Like in the case for $T_{\mathrm{max}} = 600$°C, it is possible to extract the r_{p} for $T_{\mathrm{max}} = 900$°C ($r_{\mathrm{p,inf,900}}$) as also shown in Fig. 7.11. In this case the values for constants c_1 and c_2 are found to be 2.18×10^{-10} Ω m^2 and 1.10×10^5 J mol^{-1}, respectively. The values of constants for the $r_{\mathrm{p,LSC}}$ expression is summarized in Table 7.4.

$r_{\mathrm{p,LSC}}$	$r_{\mathrm{p,LSC}} = c_1 \exp\left(\frac{c_2}{RT}\right)$	
	c_1 / Ω m^2	c_2 / J mol^{-1}
Baumann et al. [138]	2.26×10^{-10}	1.26×10^{5}
Binary sphere model (This work)	3.38×10^{-11}	1.32×10^{5}
Thin coat model, $T_{\max} = 600$°C (This work)	5.80×10^{-11}	1.10×10^{5}
$T_{\max} = 900$°C (This work)	2.18×10^{-10}	1.10×10^{5}

Table 7.4: Summary of extracted constants for the calculation of $r_{\mathrm{p,LSC}}$.

7.3.3 Optimization of infiltrated cathodes

A number of studies have already carried out parametric variations of composite cathodes consisting of IC and electronic/MIEC phases using the random sphere model with the goal of obtaining cathodes with optimized microstructure [118, 119, 121, 124, 140]. Here, we examine the physical properties essential to the infiltrated cathodes. In the previous discussions, the influence of gas transport in the infiltrated cathodes was not considered. In the following, the parametric variations include the gas transport to closely simulate the situation in actual electrodes unless indicated. The variables of interest are varied while keeping the other structural parameters constant according to Table 7.3 in the following parametric studies.

The effect of cathode thickness

The effect of the thickness of the cathodes on R_{p} is shown in Fig. 7.12. Fig. 7.12a shows the effect of the thickness of the cathode on R_{p} at varying temperatures. Notable at all temperatures is the decrease in R_{p} when the thickness is increased from ~ 1 μm to several micrometers. This is due to an increasing surface area available for oxygen reduction. This also implies that the IC phase has sufficient ionic conductivity for the range of thickness considered to transport the oxide ions to the electrolyte. When the thickness of the cathode is further increased, an increase in R_{p} is seen especially at high temperatures (> 700°C). The absolute increase is almost identical for all temperatures, but it is only clearly seen at higher temperatures because of the low R_{p}. With an increase in thickness, the available surface area for oxygen reduction is increased, but the length for gas transport is also increased which contributes more to R_{p}. Fig. 7.12b compares the R_{p} values at varying temperatures for selected cathode thicknesses. It is clear that the effect of cathode thickness is most significant at low temperatures.

The difference in the relative values of R_p decreases with increasing temperatures as reflected in the decrease in activation energy in going from 1 μm (109 kJ mol^{-1}) to 75 μm (82 kJ mol^{-1}) indicating the different processes that govern the performance of these cathodes. The thin cathode is governed mainly by the surface exchange process at practically all the temperatures considered in the model. This is due to the negligible contribution of ionic and gas transport to the total polarization brought about by the short ionic and gas pathways. Thus, the activation energy for electrode polarization reflects that for $r_{p,inf,900}$. For the thick cathode, ionic transport and the amount of active, percolated electrocatalysts are determined mainly by the IC phase. Thus, it is expected that a significant part of the overall activation energy reflects that for ionic transport in the IC phase.

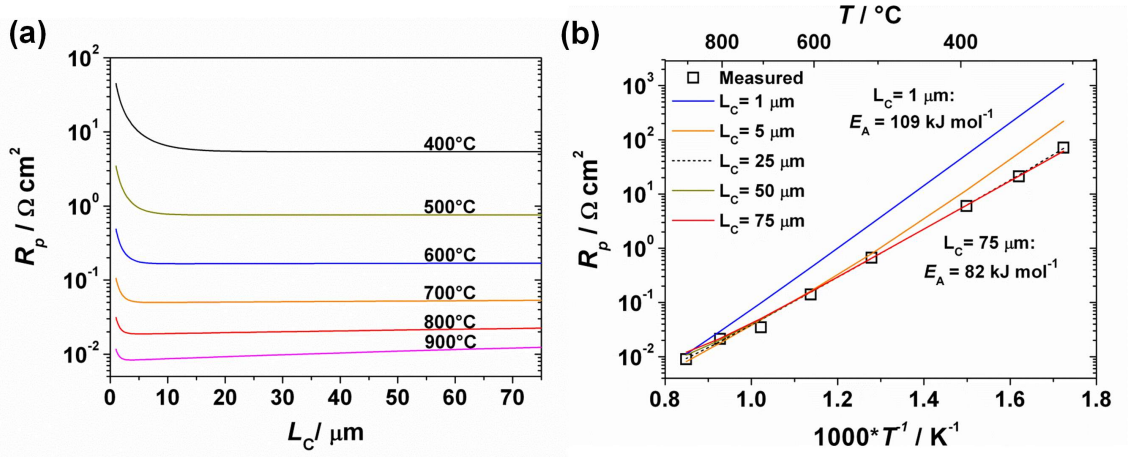

Figure 7.12: (a) R_p as a function of the cathode thickness at various temperatures. (b) R_p, as a function of the reciprocal absolute temperature in air for selected cathode thicknesses.

The effect of electronic conductivity in the MIEC phase

The effect of the thickness of the infiltrate coating is already described in the previous discussion. A related parameter that is very important, especially in infiltrated cathodes where the electrocatalysts are nanosized, is the electronic conductivity. This can be a concern because even though the bulk electronic conductivity is , the cross sectional area defined by A_{coat} in equation 7.29 can be very low which still translates

into high electronic resistance. Based on the calculated value for l_{coat}, it is calculated that the A_{coat} is only 4% of that of the geometrical area of the cathode if $t_{coat} = 5$ nm. Fig. 7.13a compares the calculated R_p's obtained from hypothetical infiltrates with varying bulk electronic conductivities but the same bulk ionic conductivities and surface exchange properties. The scenario for a thinner infiltrate coating (1 nm) is also shown for comparison (Fig. 7.13b). In both cases, the ionic conductivity and $r_{p,inf,900}$ of the LSC is fixed while the electronic conductivity is varied. The parameters in the case for LSC fired at $T_{max} = 900°C$ is also used. The gas transport is not included in the calculation. The electronic conductivities, 19000 and 4000 S m^{-1}, correspond to that for $Ca_3Co_4O_{9+\delta}$ [141] and Co_3O_4 [91] at 900°C, respectively. It can be observed from Fig. 7.13b that decreasing the electronic conductivity of the coating increases the R_p. However, the increase is only significant at high temperatures and at electronic conductivities significantly lower (100-fold) than the electronic conductivity of LSC. As most electrocatalyst used in SOFCs have bulk electronic conductivities greater than 20000 S m^{-1}, their electronic conductivity would not significantly contribute to the polarization resistance. In the case of a thinner coating such as that shown in Fig. 7.13b for 1 nm, the same trend as that for a 5 nm coating is seen, only that the increase in R_p is relatively greater with decreasing electronic conductivity. This result is expected considering the decrease in the cross sectional area for electron transport. It is seen here that the calculated R_p in this study is still accurate even for thinner coatings due to the relatively high electronic conductivity of the LSC phase. For potential infiltrates that has electronic conductivities lower than 1000 S m^{-1}, it is likely that an increased number of infiltration is required to ensure a thicker coating or better percolation among the particles to reduce the electronic conductivity loss.

As mentioned in Section 7.2.2, the present model does not account for the increase in electronic resistance due to a loss of percolation. However, from Fig. 7.13, it appears that this may not significantly affect the calculation in infiltrated cathodes where there is a high amount ($>$ 10 vol%, from the total electrode volume) of electrocatalysts that have high ($>$ 20000 S m^{-1}) electronic conductivity. It is evident that the loss of percolation may already be considered as a decrease in electronic conductivity, but as seen in Fig. 7.13 this would not significantly alter the calculated R_p.

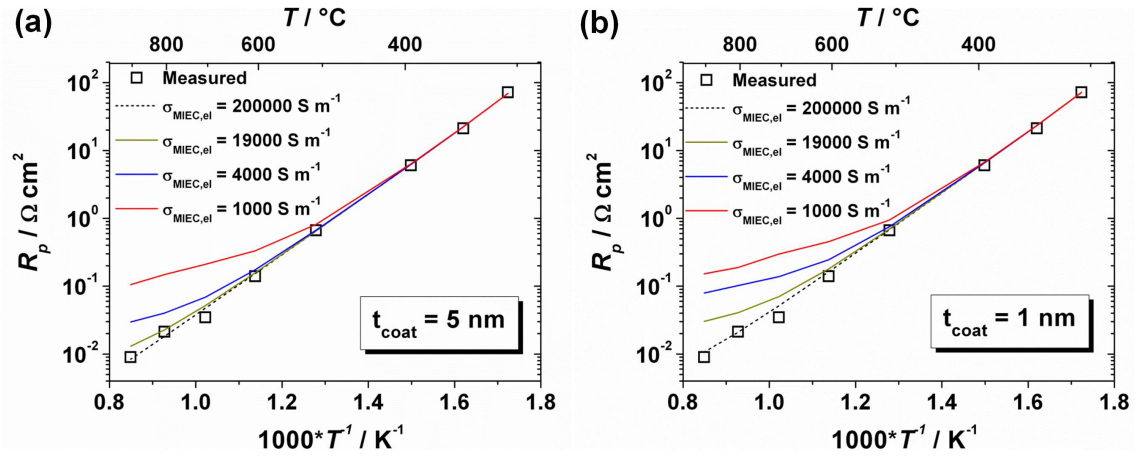

Figure 7.13: R_p as a function of the reciprocal absolute temperature in air for different electronic conductivities and thicknesses of coatings, (a) 5 nm and (b) 1 nm. The values given are bulk conductivities. Symbols show measured R_p's. The lines show the calculated values using the thin coat model. The gas transport is not included in the calculation.

The effect of the surface area of the MIEC phase

The significance of the surface area factor was mentioned briefly in the previous discussion. As also shown, the overall R_p decreases with increasing surface area factor due to an additional available surface area for oxygen surface exchange. Fig. 7.14a illustrates how much the surface area of the LSC is increased with the addition of N or M particles per CGO particle. As expected, the surface area increases with the addition of the particles. More than 10× increase in surface area can be gained if $N = N_\mathrm{max} = 17$ and $M = 50$. The specific surface area for the CGO backbone with LSC coating only, is 1.1×10^7 m^2 m^{-3}. This value is already higher than the calculated specific surface area for the conventional composite cathode (6×10^6 m^2 m^{-3}) discussed above.

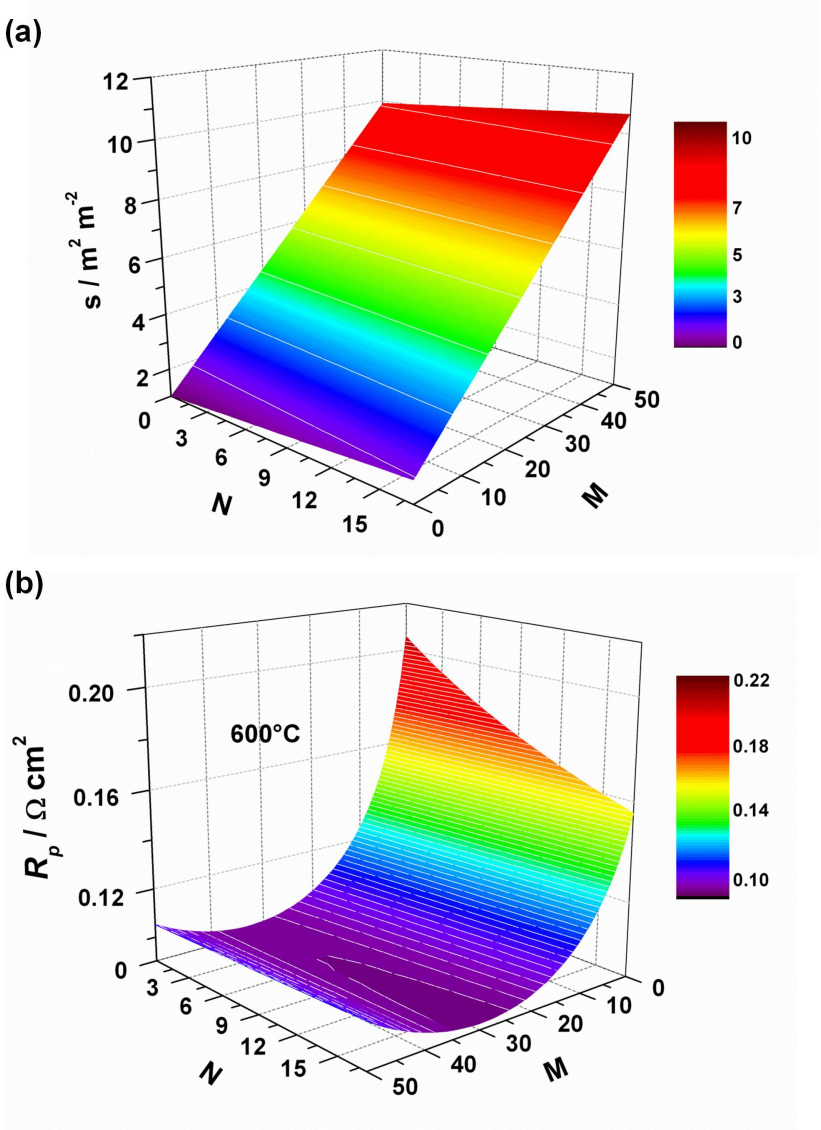

Figure 7.14: The dependence of (a) surface area factor and (b) R_{p} with N and M. Putting 50 M particles per CGO particle decreases the porosity to 15%. $N_{\max} = 17$. The temperature in (b) is fixed at 600°C.

The addition of particles, however, also entails an increase in the occupancy of pores (decrease in the porosity) and could greatly affect the gas transport in the porous electrode. Fig. 7.14b illustrates the effect at 600°C. The addition of particles decreases R_{p} up to a certain point. With further addition, the R_{p} starts to increase as the gas

transport limitation starts to dominate. Fig. 7.15 shows the effect of the amount of electrocatalyst on the overall R_p at varying temperatures. It is seen that an increase in the amount of electrocatalyst (M) decreases the R_p at low temperatures (<600°C) but increases at high temperatures. At high temperatures, the resistance associated with oxygen reduction and transport of oxide ions is low and becomes comparable to the resistance associated with the transport of oxygen in the porous structure. This situation is reversed at low temperatures and the cathode is mainly dominated by the high resistance associated with the oxygen reduction and transport of oxide ions.

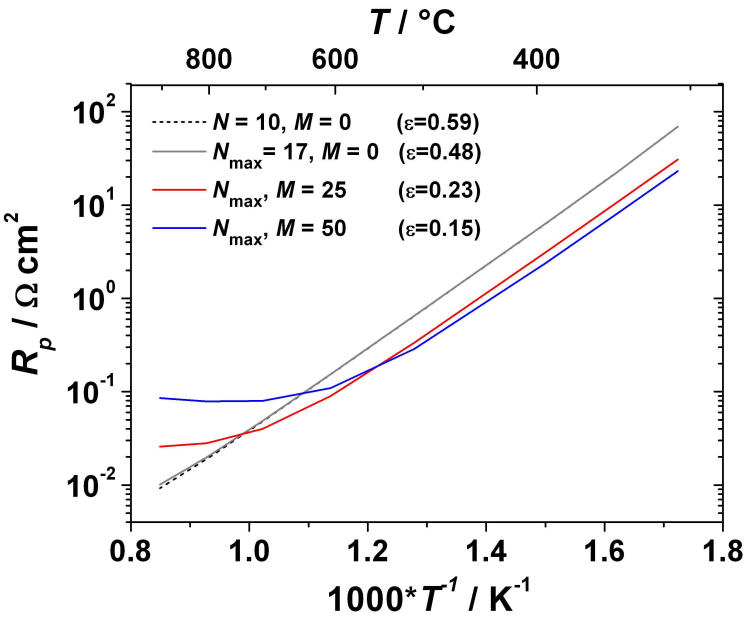

Figure 7.15: R_p as a function of the reciprocal absolute temperature in air for different amounts of LSC (hemispherical caps and spheres). The porosities (open) resulting from the addition of LSC particles are listed.

The effect of the ionic conductivity in IC and MIEC phases

The oxide ion transport properties of the backbone and the infiltrate material are also very important when considering infiltrated cathodes. Fig. 7.16 shows the effect of the ionic conductivity of the infiltrate. The ionic conductivities are varied using the bulk ionic conductivity of the LSC as a base. It is seen that in order to have a decrease in R_p, the bulk ionic conductivity has to be increased 100 times that of the bulk ionic conductivity of LSC. At this high ionic conductivity, the oxide ions going

to the electrolyte are most likely being transported in the MIEC rather than in the IC backbone which is consistent with the equivalent circuit shown in Fig. 7.4. At present there are no known MIEC that has 10 - 100 times higher ionic conductivity than LSC and it thus represents a grossly exaggerated situation. Also shown in Fig. 7.16 is the effect on R_p when decreasing the bulk ionic conductivity of the LSC. In this calculation, it was necessary to add an oxide ion diffusion contribution to r_p as it is expected that this would play a major contribution once the ionic conductivity of the MIEC goes to very low values. The length to travel for the oxide ion through the MIEC towards the IC backbone is set to $t_{coat} + r_{coat}$. As shown in Fig. 7.16, the effect in the calculated R_p is only observed when reducing the bulk ionic conductivity of the LSC 10000 times (e.g. reduction from 2.6×10^{-3} to 2.6×10^{-7} S cm^{-1} at 600°C). Due to the small oxide ion diffusion length, the ionic conductivity of the MIEC will therefore not limit the performance if the bulk ionic conductivity is greater than 10^{-7} S cm^{-1}. This has significant implications as it appears that any electrocatalyst, even with very low ionic conductivity, provided that it is has sufficient electronic conductivity, and good electrocatalytic activity can be used as an infiltrate.

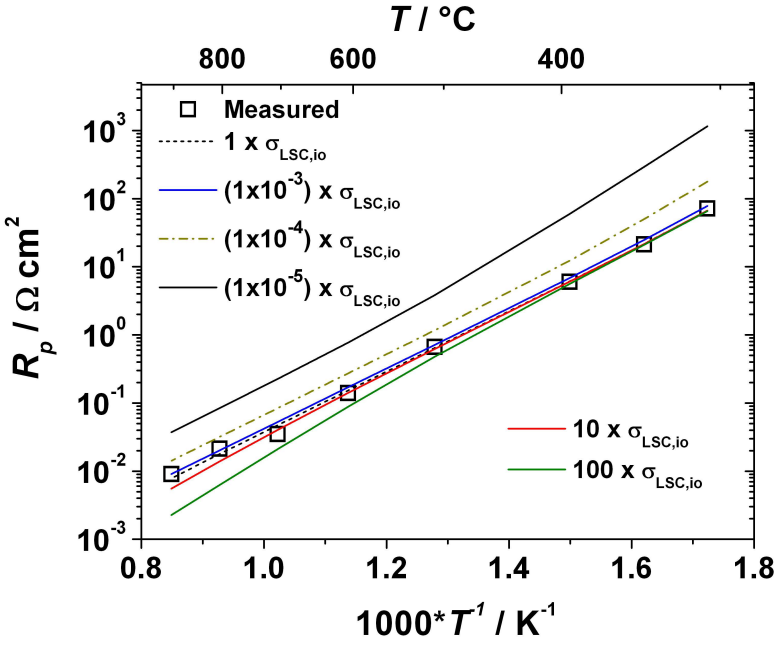

Figure 7.16: R_p as a function of the reciprocal absolute temperature in air for different ionic conductivities of the electrocatalyst used. The ionic conductivities only show multiples of the ionic conductivity of LSC. Symbols show measured R_p's. The gas transport is not included in the calculation.

Figs. 7.17a and 7.17b shows the effect of the ionic conductivity of the backbone on R_p for cathodes of thicknesses 25 μm and 75 μm, respectively. It is seen that the corresponding increase or decrease in R_p is less than the corresponding factor of change in the ionic conductivity. This is because the other resistors shown in the equivalent circuit in Fig. 7.4 also contribute to the total R_p. Another interesting point to consider is the relatively small decrease in R_p especially at low temperatures even with a 10-fold or 100-fold increase in the ionic conductivity of the backbone. Going to a thicker cathode (Fig. 7.17b), the relative decrease in R_p especially at low temperatures becomes more significant when the ionic conductivity of the backbone is increased. The difference in the relative decrease in R_p for the two thicknesses when the ionic conductivity of the backbone is increased can be understood by the difference in the size of areas activated at low temperatures in the 25 and 75 μm thick cathodes. In the 25 μm thick cathode, the already high ionic conductivity in the CGO backbone at low temperatures has most likely extended the active area to almost the entire electrode. A further increase in the ionic conductivity in this case only activates the rest of the volume slightly. This is clearly evident from the relatively small decrease in R_p at low temperatures when the ionic conductivity of the backbone is increased up to 100 times. For a thicker cathode (Fig. 7.17b), the inactive volume is still large and an increase in ionic conductivity of the backbone causes a significant part of this to be activated, resulting in significantly lower values of R_p.

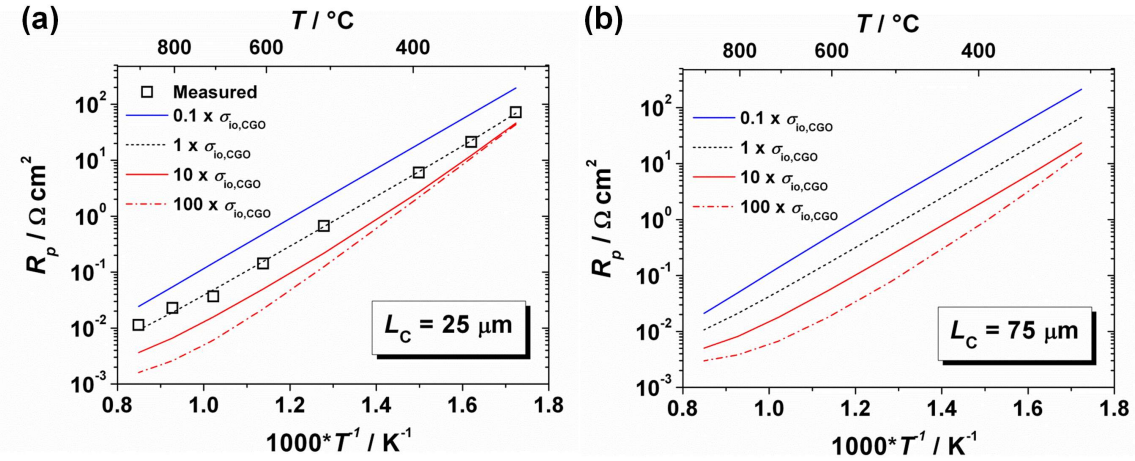

Figure 7.17: R_p as a function of the reciprocal absolute temperature in air for different ionic conductivities of the backbone and different cathode thicknesses: (a) 25 μm and (b) 75 μm. Symbols show measured R_p's.

Shown in Fig. 7.18a are the calculated R_p's at different temperatures using various ionic conductors as backbones for a 25 μm thick electrode considered in this model. The expressions used for the ionic conductivities of these materials are listed in Table 7.5. These expressions are extracted by fitting the experimental data from the corresponding list of references. The backbones considered in the model are $Ce_{0.9}Gd_{0.1}O_{1.95}$ (CGO) [43], 8 mol % yttria-stabilized zirconia (8YSZ) [13], 9.3 mol% Sc_2O_3 in ZrO_2 (9.3ScSZ) [42], $La_{0.9}Sr_{0.1}Ga_{0.9}Mg_{0.1}O_3$ (LSGM) [33], and $Bi_2V_{0.1}Cu_{0.8}O_{5.35}$ (BICUVOX) [34]. It should be noted that the study is only focusing on the values of the ionic conductivity of the said materials, thus the phase stability and reactivity of these materials with the infiltrate is not considered. Fig. 7.18a suggests that in order to get the lowest R_p, the backbone should have the highest ionic conductivity possible and in this case, the use of BICUVOX is suggested. However, for this thickness, the gain in R_p is small especially at low temperatures, even for a ten-fold increase in the ionic conductivity e.g. by switching from CGO to BICUVOX. Shown in Fig. 7.18b are the same data but using a thicker cathode (75 μm). It is clear, especially at low temperature that a significant advantage of having a BICUVOX backbone is only realized for very thick cathodes. A reduction of approximately 3 times in R_p can be obtained at low temperatures. As mentioned previously, this is because the other resistances (sur-

face exchange properties) are also limiting the performance of the cathode. Fig. 7.18c shows the R_p as a function of cathode thickness using CGO and BICUVOX backbones at 300 and 800°C. It shows that for an identical microstructure at low temperature, the decrease in R_p by increasing the ionic conductivity of the backbone (i.e. replacing CGO with BICUVOX) is predominantly realizable when the thickness of the electrode is increased.

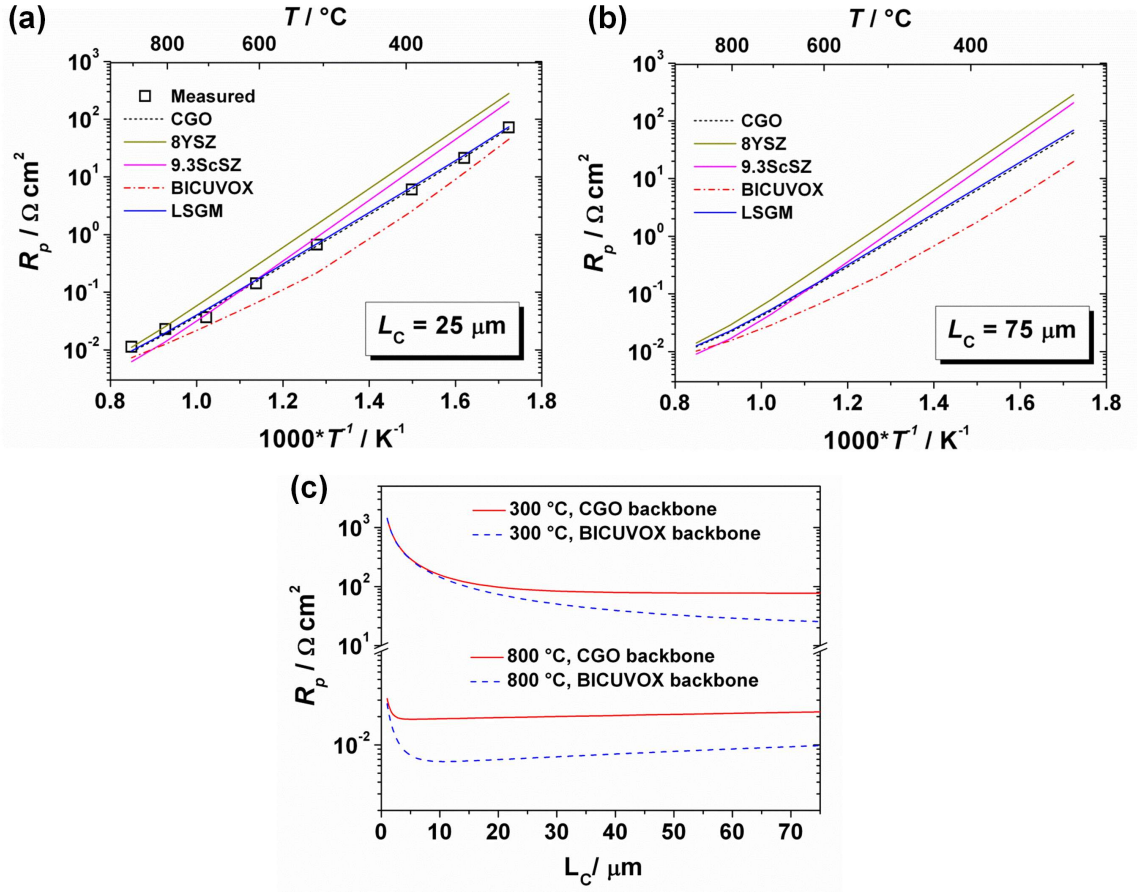

Figure 7.18: R_p as a function of the reciprocal absolute temperature in air for different SOFC backbones and different cathode thicknesses: (a) 25 μm and (b) 75 μm. Symbols show measured R_p's. (c) R_p as a function of cathode thickness for CGO and BICUVOX backbone. R_p's are shown for 300 and 800°C.

	$\sigma = \frac{\sigma_0}{T} \exp\left(\frac{E_A}{RT}\right)$		σ (S m^{-1})			
Backbone	σ_0 (S m^{-1})	E_A (J mol^{-1})	400°C	600°C	800°C	Ref.
CGO	1.3×10^7	6.5×10^4	0.19	2.0	8.8	[43]
8YSZ	1.4×10^8	9.1×10^3	0.016	0.53	4.5	[13]
9.3ScSZ	1.1×10^9	9.8×10^4	0.04	1.7	17	[42]
LSGM	1.8×10^7	6.8×10^4	0.14	1.7	7.9	[33]
BICUVOX:						
(<480°C)	5.1×10^7	5.8×10^4	2.3			[34]
(>480°C)	9.1×10^5	3.3×10^4		11	21	[34]

Table 7.5: Expressions used for the ionic conductivity of the backbones. The expressions are obtained by fitting the corresponding data from the listed references.

To examine the effect of the catalytic activity of the infiltrate, the R_p is examined as the area specific material surface exchange resistance, $r_{p,inf900}$, is varied. Fig. 7.19 shows the effect of increasing or decreasing $r_{p,inf900}$ on R_p for 25 and 75 μm thick cathodes. As in the case of changing the ionic conductivity of the backbone, the amount of increase/decrease in $r_{p,inf900}$ does not correspond to an equivalent amount of change in R_p. However, it is obvious from Table 7.6 that compared from changing the bulk ionic conductivity of the backbone, the gain in performance at low temperatures (e.g. 400°C) varies more proportionally with the change in $r_{p,inf900}$ irrespective of the cathode thickness. This means that for this range of thicknesses, the ionic conductivity of the backbone is sufficient to transport the increased amount of oxide ions which were converted from oxygen in the surface of the MIEC due to the decrease in r_p.

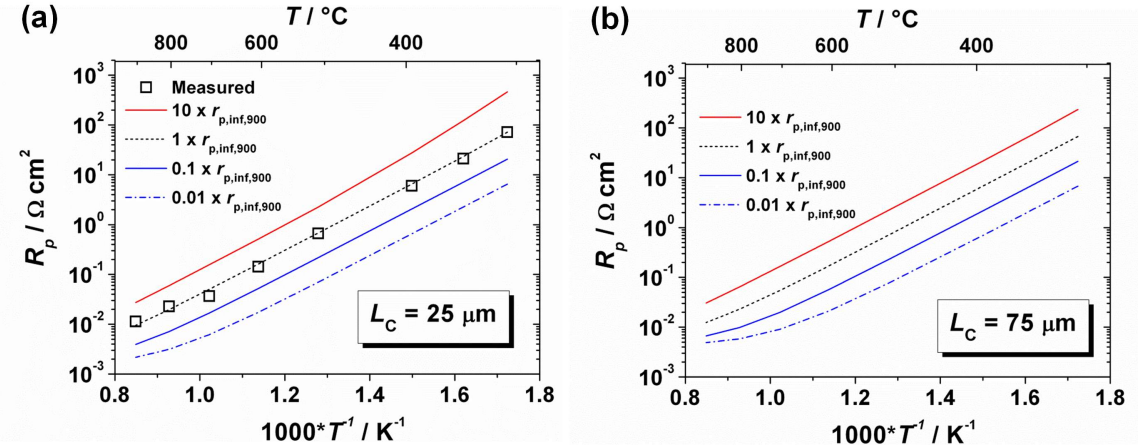

Figure 7.19: R_p as a function of the reciprocal absolute temperature in air for different $r_{\mathrm{p,inf,900}}$ and different cathode thicknesses: (a) 25 μm and (b) 75 μm. Symbols show measured R_p's. The r_p's only show multiples of the r_p of LSC fired at 900°C.

	R_p (Ω cm^2)			R_p (Ω cm^2)		
$L_\mathrm{C}(\mu\mathrm{m})$	1×	10×	100×	1×	0.1×	0.01×
	$\sigma_{\mathrm{io,CGO}}$			$r_{\mathrm{p,infCGO}}$		
25	6.8	2.8	2.2	6.8	2.1	0.67
75	6.7	2.1	0.91	6.7	2.1	0.69

Table 7.6: Comparison of the relative decrease in R_p at 400°C with the change in ionic conductivity of the backbone and surface exchange resistance. The values shown are multiples of the $\sigma_{\mathrm{io,CGO}}$ and $r_{\mathrm{p,inf,900}}$.

7.4 Summary

A 1-dimensional micromodel based on the concepts of a random binary sphere model combined with geometrical considerations to represent the microstructure of infiltrates has been developed that could predict the polarization resistance of cathodes prepared by infiltration. The binary sphere model was first used in a conventional LSC/CGO composite cathode to extract the material specific surface exchange resistance of LSC, $r_{\mathrm{p,LSC}}$, and was found to be lower compared to the values obtained by means of well-defined thin film model electrodes (e.g. at 750°C in air, the value of $r_{\mathrm{p,LSC}}$ obtained

in this study is about 2 Ω cm^2, compared to the range 4 - 8 Ω cm^2 for a thin film LSC model electrode). The thin coat model combined with this kinetic expression was used to estimate the polarization resistance of an LSC infiltrated cathode. It was found that the calculated R_p's are significantly higher than the measured values suggesting that the performance of the infiltrated cathodes are not only characterized by the high surface area available for oxygen surface exchange due to their nanoscale size but also from a better surface exchange property.

A series of parametric variations has been performed with the goal of obtaining high performance cathodes prepared by infiltration. It was shown that R_p decreases when the thickness of the cathode is increased up to a certain value due to increasing amount of electrocatalyst material that is available for surface exchange. Further increase in thickness would increase R_p due to increasing contribution of the gas transport resistance. The amount of infiltrated particles should be high enough not only to increase the surface area for oxygen surface exchange but to decrease the probability of loss of percolation when the infiltrated particles are fired at higher temperatures. The amount of infiltrates, however, should not reach a point where the infiltrates start to block the pores thereby increasing the gas transport resistance. Related to the amount of infiltrated particles is the thickness and percolation of the infiltrate coating. Due to the relatively high electronic conductivity of the infiltrate material considered in this study, it was observed that that the calculated R_p is not significantly changed in the range of thicknesses considered here (1 - 20 nm). For potential infiltrates with low bulk electronic conductivity (< 1000 S m^{-1}), it was observed that a thick coating (> 1 nm) is preferred in order to avoid electronic conduction limitation. In general, the backbone should have the highest ionic conductivity to minimize the oxide ion transport limitation especially at low temperatures. It was demonstrated that the ionic conductivity of the backbone plays a crucial role for thicker cathodes as this determines the amount of active thickness in the cathode. It was also demonstrated that an infiltrate material with the lowest area specific material surface exchange is preferred.

Chapter 8

Conclusion and Recommendations for Future Work

It was shown that high performance cathodes for potential operation at low temperatures can be obtained from multi-phased, $LaCoO_3$- based infiltrated - CGO cathodes. Specifically for LSC infiltrated - CGO cathodes, a systematic variation of parameters such as CGO backbone firing temperature, LSC firing temperature, and LSC loading, provided a guide for developing high performance LSC infiltrated cathodes. Functional cathodes were also obtained by infiltrating $LaCoO_3$ and Co_3O_4 onto a porous CGO backbone. The feasibility of integrating an LSC infiltrated - CGO cathode onto an anode supported solid oxide fuel has also been demonstrated. An attempt to replace the CGO backbone with a higher ionic conducting material such as BICUVOX has been performed but was found that the performance of LSC infiltrated - BICUVOX cathodes is limited by the poor microstructure of the BICUVOX backbone and the poor chemical compatibility of the BICUVOX and the LSC infiltrate. The material $Ca_3Co_4O_{9+\delta}$ was demonstrated to be an effective cathode material when used with CGO. Finally, a 1-dimensional model has been developed in order to understand nad predict the performance of cathodes prepared by infiltration.

Based on the findings of this dissertation, several recommendations for future work can be mentioned:

- The surface exchange properties of nanoparticulate LSC, $LaCoO_3$, and Co_3O_4 can be studied in detail. Further, the extent of the influence of Co_3O_4 on the surface exchange properties of $LaCoO_3$ and LSC has to be studied in depth. In this regard, an effort has to be done to obtain phase pure $LaCoO_3$ and LSC infiltrates. An experiment can then be performed which investigates the effect of the addition of cobalt on the material and electrochemical properties of $LaCoO_3$ and LSC infiltrated cathodes. The studies can be in the form of electrochemical characterization by impedance spectroscopy on symmetric cathodes or structural studies by transmission electron microscopy TEM which can involve *in - situ* high temperature TEM.

- Additional durability testing such as thermal cycling and atmosphere variation has to be performed to provide a more comprehensive information on the stability of the LSC infiltrated - CGO cathode. Further, as the results on the variation of LSC firing temperature suggest that the main degradation mechanism is grain growth leading to a loss of electronic percolation, future studies focusing on enhancing the durability of LSC infiltrated cathodes can consider suppressing the grain growth by addition of another phase such as ceria or doped ceria and/or limiting the loss of electronic percolation by using backbones with sufficient electronic conductivity.

- The surface exchange resistance values obtained for the LSC infiltrate in the modeling has to be verified by experiment.

- Other materials which have good chemical compatibility with BICUVOX such as Ag can be infiltrated into a BICUVOX backbone. Considering the microstructure of BICUVOX backbone, it was found that the resulting backbone microstructure is limited by the high temperature firing required for the BICUVOX to adhere to the dense CGO. This can be mitigated, if possible, by the deposition of a thin layer followed by firing of a bismuth-based material on top of the dense CGO prior to screen printing to provide an anchor and an interlayer to the screen printed BICUVOX. A possible low temperature firing can follow to obtain a BICUVOX backbone with fine microstructure.

Appendix A

Electrochemical performance of Pt paste/noninfiltrated backbone electrodes

The electrochemical performance of Pt paste/noninfiltrated backbones under varying firing temperatures in air is studied by electrochemical impedance spectroscopy. The noninfiltrated backbones include CGO and BICUVOX.

1. Pt paste/noninfiltrated CGO

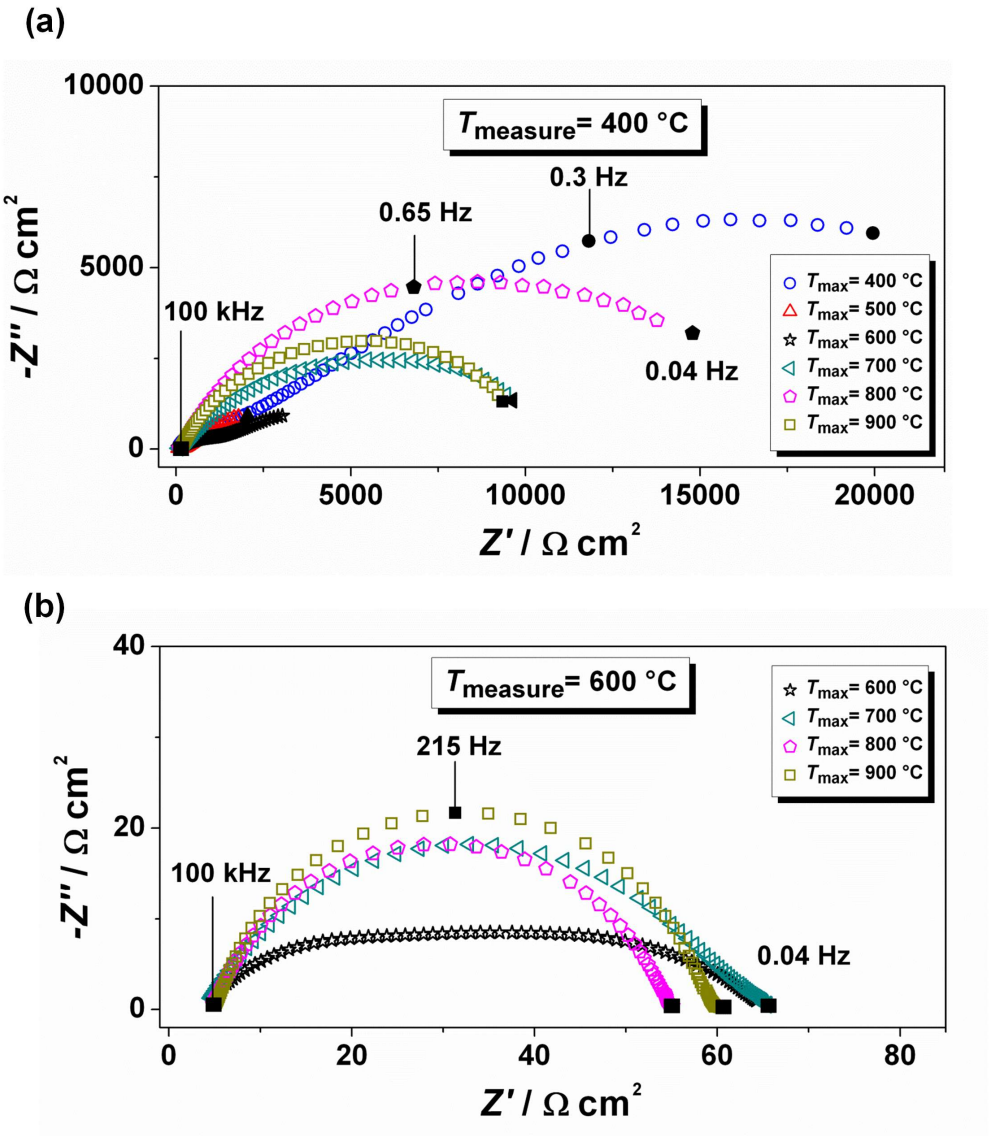

Figure A.1: Impedance spectra of the Pt paste/noninfiltrated CGO backbone electrode taken at (a) 400 and (b) 600°C under varying firing temperatures in air.

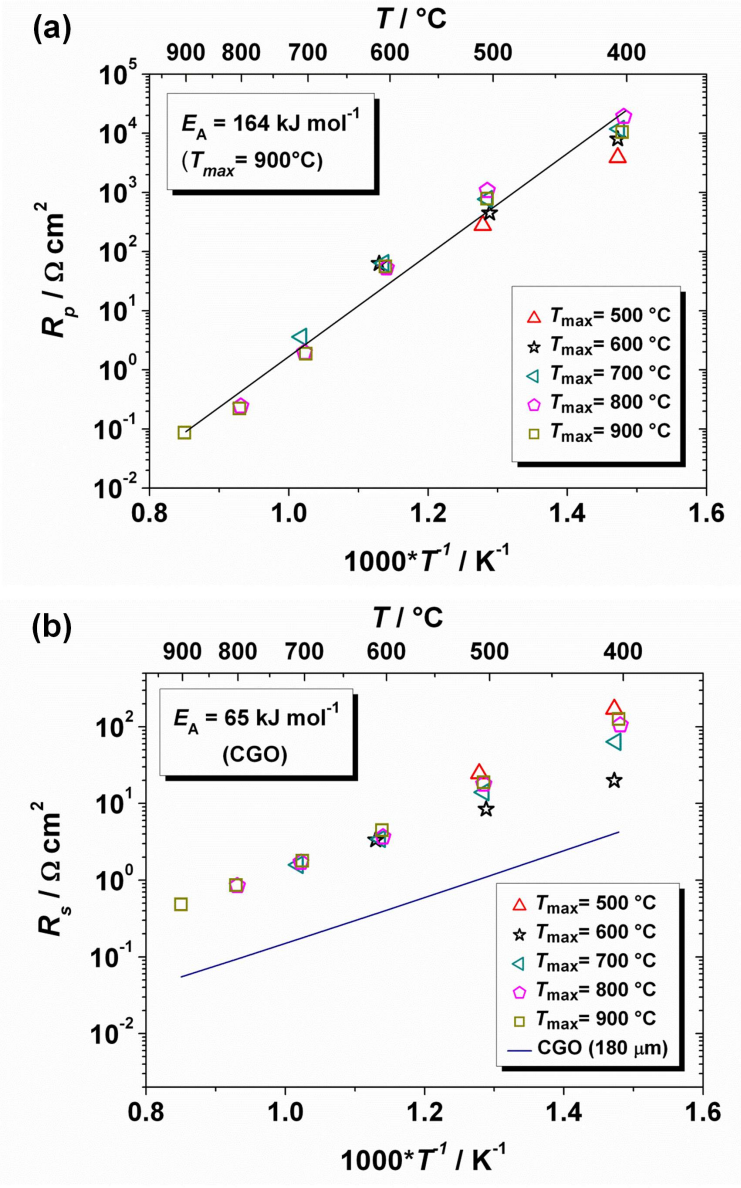

Figure A.2: (a) R_{p} and (b) R_{s} as a function of the reciprocal absolute temperature of the Pt paste/noninfiltrated CGO backbone electrode under varying firing temperatures in air. The straight line in (b) corresponds to the calculated series resistance of a 180 μm CGO electrolyte [43].

2. Pt paste/noninfiltrated BICUVOX

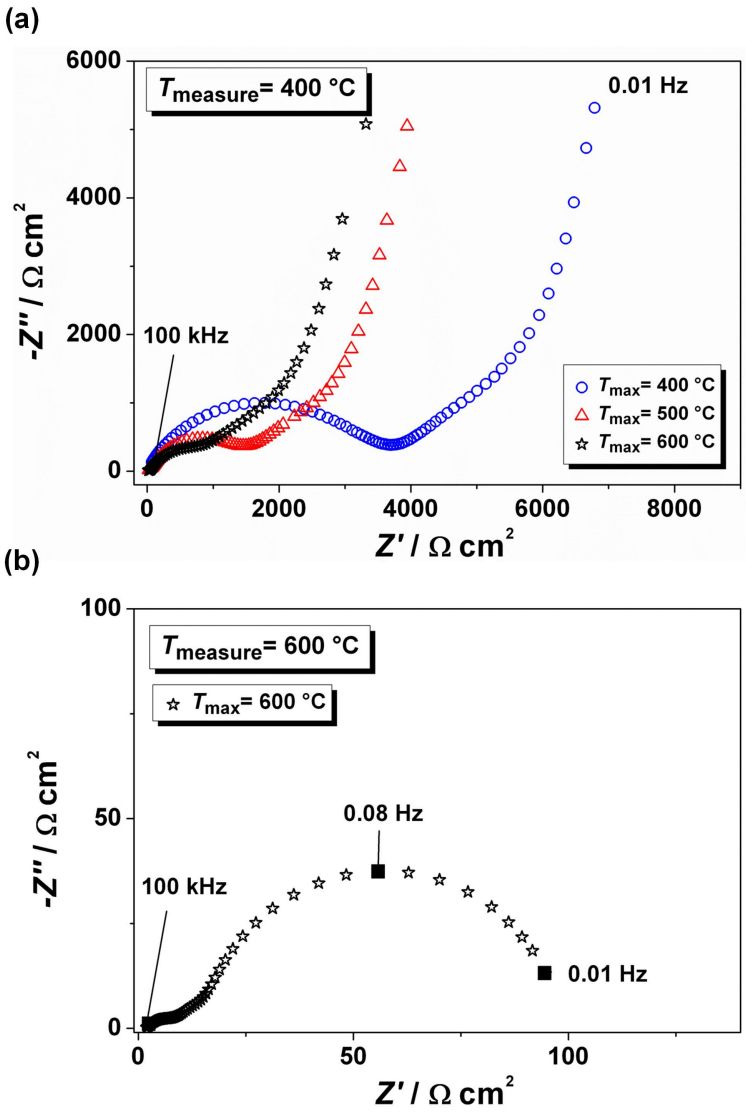

Figure A.3: Impedance spectra of the Pt paste/noninfiltrated BICUVOX backbone electrode taken at (a) 400 and (b) 600°C under varying firing temperatures in air.

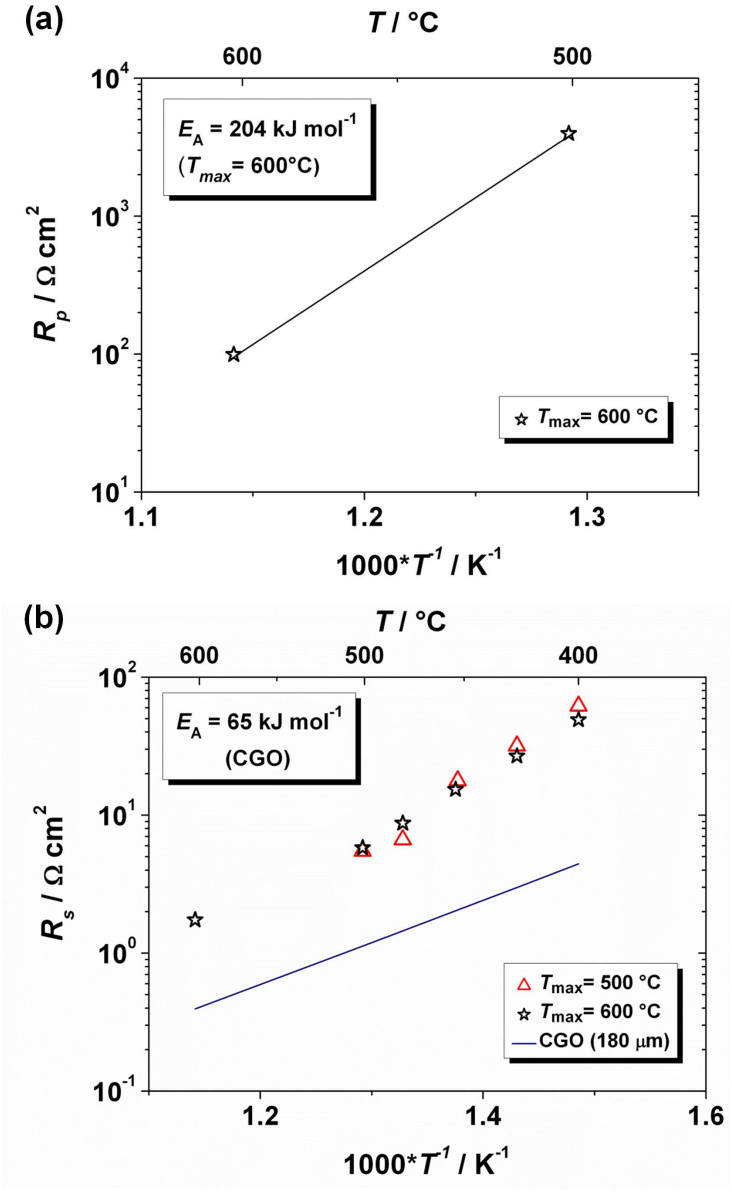

Figure A.4: (a) R_p and (b) R_s as a function of the reciprocal absolute temperature of the Pt paste/noninfiltrated BICUVOX backbone electrode under varying firing temperatures in air. The straight line in (b) corresponds to the calculated series resistance of a 180 μm CGO electrolyte [43].

Appendix B

Characterization of wet deposited LSC onto dense CGO electrolyte

The microstructure, in-plane electronic conductivity and electrochemical performance of wet deposited aqueous nitrate solution of LSC onto dense CGO electrolyte are investigated. Dense, 290 μm thick CGO electrolyte was cut into squares (6 $\times$ 6 cm^2). The dense CGO samples were dipped into an aqueous nitrate solution of LSC that was also used in infiltration. The resulting symmetric cell samples were then precalcined at 350°C followed by re-dipping into the same solution. The cycle is repeated for six times. Preparation of the samples for electrochemical performance and in-plane electronic conductivity characterization is as discussed in Chapters' 2 and 5, respectively.

Results:

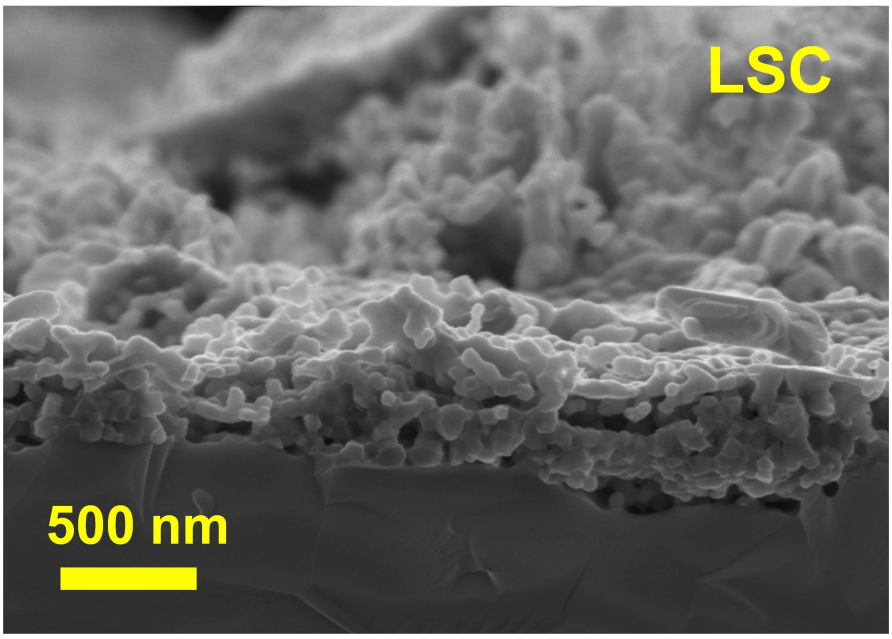

Figure B.1: Fracture cross section of wet deposited LSC onto dense CGO electrolyte after firing at 900°C in air.

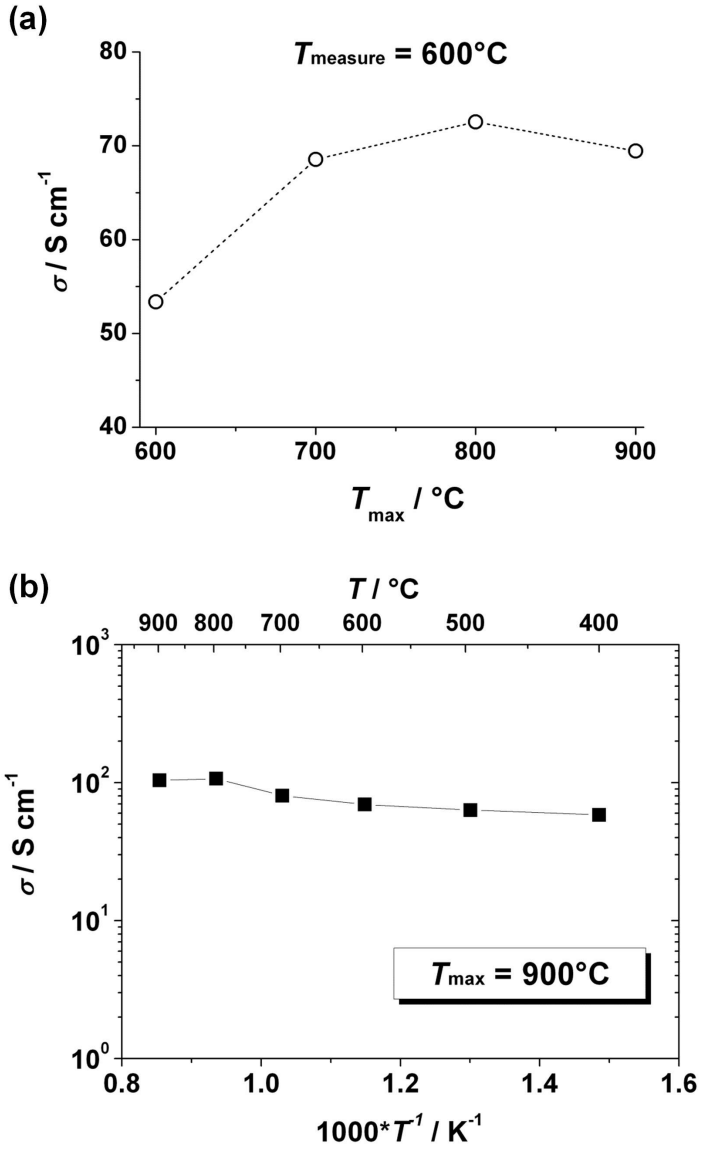

Figure B.2: (a) Dependence of the total conductivity of wet deposited LSC at 600°C with maximum firing temperature, $T_{\max}$. (b) Total conductivity of wet deposited LSC as function of the reciprocal absolute temperature. The layer is fired at 900°C in air.

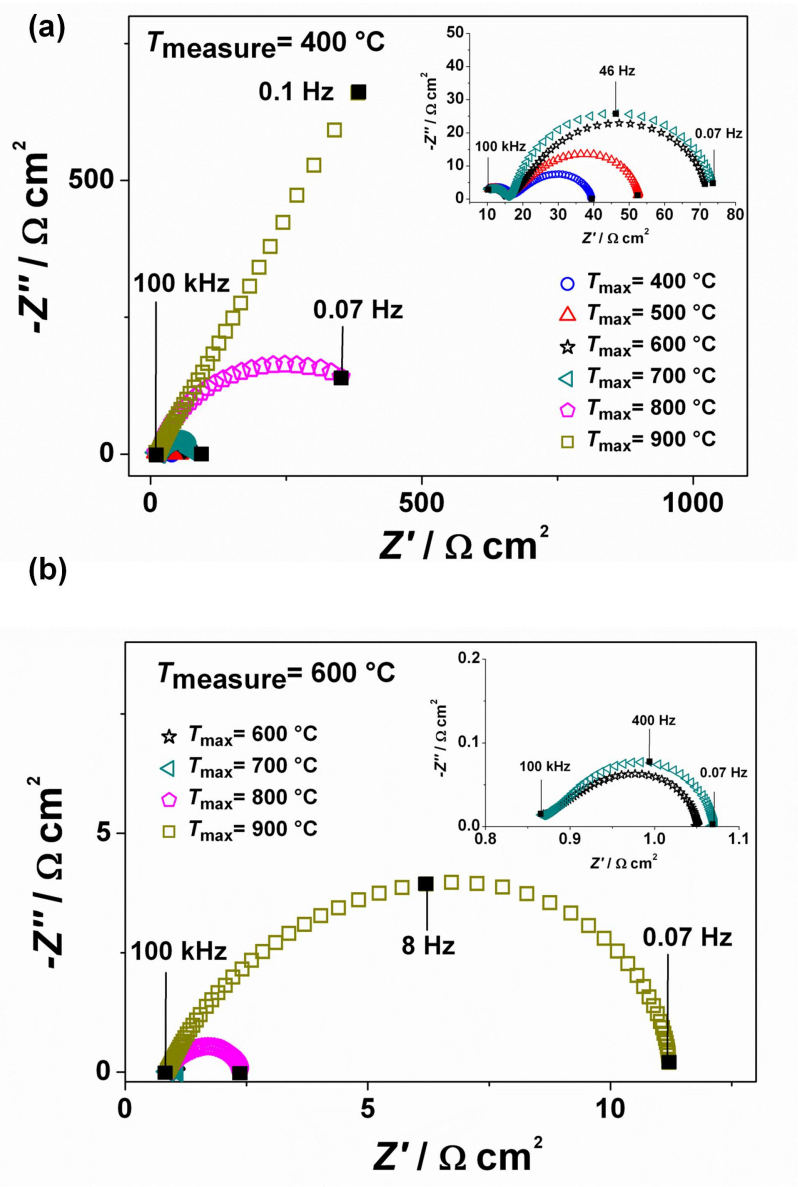

Figure B.3: Representative complex plane plots (a) at 400°C and (b) 600°C as a function of LSC firing temperature. The number of dippings into the LSC precursor solution and the corresponding precalcination step is fixed to 6 times.

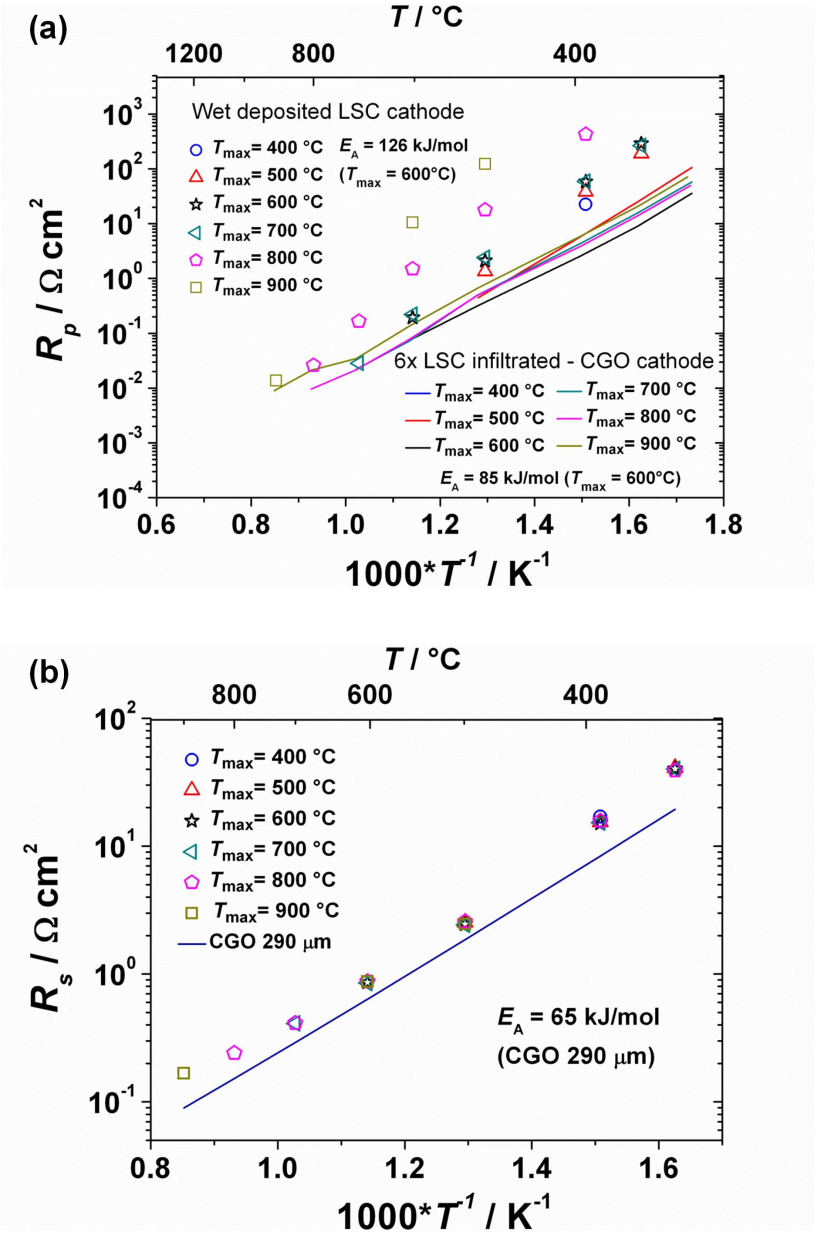

Figure B.4: (a) R_{p} and (b) R_{s} as a function of the reciprocal absolute temperature of the wet deposited LSC under varying firing temperatures in air. The data for a 6× LSC infiltrated - CGO cathode is shown for comparison. The straight line in (b) corresponds to the calculated series resistance of a 290 μm CGO electrolyte [43].

Bibliography

[1] M. Farooque and H. C. Maru, "Fuel cells - the clean and efficient power generators," *Proceeedings of the IEEE*, vol. 89, no. 12, pp. 1819–1829, 2001.

[2] W. Nernst, "Über die elektrolytische leitung fester körper bei sehr hohen temperaturen," *Zeitschrift für Elektrochemie*, vol. 6, no. 2, pp. 41–43, 1899.

[3] M. C. Tucker, "Progress in metal-supported solid oxide fuel cells: A review," *Journal of Power Sources*, vol. 195, pp. 4570–4582, 8/1 2010.

[4] C. Sun, R. Hui, and J. Roller, "Cathode materials for soild oxide fuel cells: a review," *Journal of Solid State Electrochemistry*, vol. 14, pp. 1125–1144, 2010.

[5] B. C. H. Steele, "Appraisal of $Ce_{1-y}Gd_yO_{2-y/2}$ electrolytes for IT-SOFC operation at 500°C," *Solid State Ionics*, vol. 129, pp. 95–110, 4 2000.

[6] B. C. H. Steele and A. Heinzel, "Materials for fuel-cell technologies," *Nature*, vol. 414, pp. 345–352, 2001.

[7] E. Ivers-Tiffeé and A. V. Virkar, *Electrode polarisations*, p. 230. High temperature solid oxide fuel cells: fundamentals, design and applicatios, Oxford, U.K.: Elsevier Ltd., 2003.

[8] J. Fleig, "Solid oxide fuel cell cathodes: Polarization mechanisms and modeling of the electrochemical performance," *Annual Review of Materials Research*, vol. 33, pp. 361–382, 08/01 2003. doi: 10.1146/annurev.matsci.33.022802.093258.

[9] S. B. Adler, "Factors governing oxygen reduction in solid oxide fuel cell cathodes," *Chemical reviews*, vol. 104, pp. 4791–4844, 10/01 2004. doi: 10.1021/cr020724o.

[10] H. Yokokawa and T. Horita, *Cathodes*, p. 126. High temperature solid oxide fuel cells: fundamentals, design and applications, Oxford, U.K: Elsevier Ltd., 2003.

[11] F. Tietz, I. A. Raj, M. Zahid, and D. Stöver, "Electrical conductivity and thermal expansion of $La_{0.8}Sr_{0.2}(Mn,Fe,Co)O_{3-\delta}$ perovskites," *Solid State Ionics*, vol. 177, pp. 1753–1756, 10/15 2006.

[12] H. Yokokawa and T. Horita, *Cathodes*, p. 125. High temperature solid oxide fuel cells: fundamentals, design and applications, Oxford, U.K.: Elsevier Ltd., 2003.

[13] M. Mori, T. Abe, H. Itoh, O. Yamamoto, Y. Takeda, and T. Kawahara, "Cubic-stabilized zirconia and alumina composites as electrolytes in planar type solid oxide fuel cells," *Solid State Ionics*, vol. 74, pp. 157–164, 12/15 1994.

[14] M. V. Patrakeev, J. A. Bahteeva, E. B. Mitberg, I. A. Leonidov, V. L. Kozhevnikov, and K. R. Poeppelmeier, "Electron/hole and ion transport in $La_{1-x}Sr_xFeO_{3-\delta}$," *Journal of Solid State Chemistry*, vol. 172, pp. 219–231, 4 2003.

[15] S. P. Simner, J. F. Bonnett, N. L. Canfield, K. D. Meinhardt, V. L. Sprenkle, and J. W. Stevenson, "Optimized lanthanum ferrite-based cathodes for anode-supported sofcs," *Electrochemical and Solid-State Letters*, vol. 5, pp. A173–A175, July 2002 2002.

[16] J. M. Ralph, C. Rossignol, and R. Kumar, "Cathode materials for reduced-temperature SOFCs," *Journal of the Electrochemical Society*, vol. 150, pp. A1518–A1522, November 2003 2003.

[17] C. Xia and M. Liu, "Low-temperature sofcs based on $Gd_{0.1}Ce_{0.9}O_{1.95}$ fabricated by dry pressing," *Solid State Ionics*, vol. 144, pp. 249–255, 12/11 2001.

[18] S. Wang, T. Chen, and S. Chen, "Kinetics of oxygen reduction over $Sm_{0.5}Sr_{0.5}CoO_3$ supported on $La_{0.9}Sr_{0.1}Ga_{0.8}Mg_{0.2}O_3$," *Journal of the Electrochemical Society*, vol. 151, pp. A1461–A1467, 2004 2004.

[19] Z. Shao and S. M. Haile, "A high-performance cathode for the next generation of fuel cells," *Nature*, vol. 431, pp. 170–173, 2004.

[20] V. V. Kharton, A. A. Yaremchenko, A. L. Shaula, M. V. Patrakeev, E. N. Naumovich, D. I. Logvinovich, J. R. Frade, and F. M. B. Marques, "Transport properties and stability of Ni-containing mixed conductors with perovskite- and K_2NiF_4-type structure," *Journal of Solid State Chemistry*, vol. 177, pp. 26–37, 1 2004.

[21] S. J. Skinner and J. A. Kilner, "Oxygen diffusion and surface exchange in $La_{2-x}Sr_xNiO_{4+d}$," *Solid State Ionics*, vol. 135, pp. 709–712, 11/1 2000.

[22] A. J. Jacobson, "Materials for solid oxide fuel cells," *Chemistry of Materials*, vol. 22, no. 22, pp. 660–674, 2010.

[23] A. A. Taskin, A. N. Lavrov, and Y. Ando, "Achieving fast oxygen diffusion in perovskites by cation ordering," *Applied Physics Letters*, vol. 86, p. 091910, 28 February 2005 2005.

[24] A. Tarancón, J. Pena-Martinez, D. Marrero-Lopez, A. Morata, J. C. Ruiz-Morales, and P. Nunez, "Stability, chemical compatibility and electrochemical performance of $GdBaCo_2O_{5+x}$ layered perovskite as a cathode for intermediate temperature solid oxide fuel cells," *Solid State Ionics*, vol. 179, pp. 2372–2378, 12/31 2008.

[25] J. H. Kim, M. Cassidy, J. T. S. Irvine, and J. Bae, "Advanced electrochemical properties of $LnBa_{0.5}Sr_{0.5}Co_2O_{5+\delta}$ (Ln = Pr, Sm, and Gd) as cathode materials for it-sofc," *Journal of the Electrochemical Society*, vol. 156, pp. B682–B689, 2009 2009.

[26] E. P. Murray and S. A. Barnett, "(La,Sr)MnO_3-(Ce,Gd)O_{2-x} composite cathodes for solid oxide fuel cells," *Solid State Ionics*, vol. 143, pp. 265–273, 7/2 2001.

[27] T. Kenjo and M. Nishiya, "$LaMnO_3$ air cathodes containing ZrO_2 electrolyte for high temperature solid oxide fuel cells," *Solid State Ionics*, vol. 57, pp. 295–302, 10 1992.

[28] M. J. L. Østergård, C. Clausen, C. Bagger, and M. Mogensen, "Manganite-zirconia composite cathodes for SOFC: Influence of structure and composition," *Electrochimica Acta*, vol. 40, pp. 1971–1981, 9 1995.

[29] M. J. Jørgensen, S. Primdahl, C. Bagger, and M. Mogensen, "Effect of sintering temperature on microstructure and performance of LSM-YSZ composite cathodes," *Solid State Ionics*, vol. 139, pp. 1–11, 1/2 2001.

[30] E. V. Tsipis and V. V. Kharton, "Electrode materials and reaction mechanisms in solid oxide fuel cells: a brief review II. electrochemical behavior vs. materials science aspects," *J Solid State Electrochem*, vol. 12, pp. 1367–1391, 2008.

[31] A. V. Berenov, A. Atkinson, J. A. Kilner, E. Bucher, and W. Sitte, "Oxygen tracer diffusion and surface exchange kinetics in $La_{0.6}Sr_{0.4}CoO_{3-\delta}$," *Solid State Ionics*, vol. 181, pp. 819–826, 6/17 2010.

[32] P. S. Manning, J. D. Sirman, and J. A. Kilner, "Oxygen self-diffusion and surface exchange studies of oxide electrolytes having the fluorite structure," *Solid State Ionics*, vol. 93, pp. 125–132, 12 1996.

[33] T. Ishihara, H. Matsuda, and Y. Takita, "Doped $LaGaO_3$ perovskite type oxide as a new oxide ionic conductor," *Journal of the American Chemical Society*, vol. 116, no. 9, p. 3801, 1994.

[34] F. Abraham, J. C. Boivin, G. Mairesse, and G. Nowogrocki, "The bimevox series: A new family of high performances oxide ion conductors," *Solid State Ionics*, vol. 40-41, pp. 934–937, 8 1990.

[35] J. W. Stevenson, T. R. Armstrong, L. R. Pederson, J. Li, C. A. Lewinsohn, and S. Baskaran, "Effect of A-site cation nonstoichiometry on the properties of doped lanthanum gallate," *Solid State Ionics*, vol. 113-115, pp. 571–583, 12/1 1998.

[36] E. Djurado and M. Labeau, "Second phases in doped lanthanum gallate perovskites," *Journal of the European Ceramic Society*, vol. 18, no. 10, pp. 1397–1404, 1998.

[37] K. R. Kendall, C. Navas, J. K. Thomas, and H. C. zur Loye, "Recent developments in oxide ion conductors: Aurivillius phases," *Chemistry of Materials*, vol. 8, no. 3, p. 642, 1996.

[38] J. C. Boivin and G. Mairesse, "Recent material developments in fast oxide ion conductors," *Chemistry of Materials*, vol. 10, pp. 2870–2888, 10/01 1998. doi: 10.1021/cm980236q.

[39] Z. Shao, J. Mederos, C. Kwak, and S. M. Haile, "Evaluation of $Bi_2V_{0.9}Cu_{0.1}O_{5.35}$—an Aurivillius-type conducting oxide—as a cathode material for single-chamber solid-oxide fuel cells," *Journal of Fuel Cell Science and Technology*, vol. 7, p. 021016, April 2010 2010.

[40] V. V. Kharton, E. N. Naumovich, and V. V. Samokhval, "Formation and properties of reaction layers of cobaltite electrodes on bismuth oxide electrolytes," *Solid State Ionics*, vol. 99, pp. 269–280, 8/2 1997.

[41] M. Mogensen, N. M. Sammes, and G. A. Tompsett, "Physical, chemical and electrochemical properties of pure and doped ceria," *Solid State Ionics*, vol. 129, pp. 63–94, 4 2000.

[42] S. P. S. Badwal, F. T. Ciacchi, and D. Milosevic, "Scandia-zirconia electrolytes for intermediate temperature solid oxide fuel cell operation," *Solid State Ionics*, vol. 136-137, pp. 91–99, 11/2 2000.

[43] B. Dalslet, P. Blennow, P. V. Hendriksen, N. Bonanos, D. Lybye, and M. Mogensen, "Assessment of doped ceria as electrolyte," *Journal of Solid State Electrochemistry*, vol. 10, pp. 547–561, 2006.

[44] C. Xia and M. Liu, "Novel cathodes for low-temperature solid oxide fuel cells," *Advanced Materials*, vol. 14, no. 7, pp. 521–523, 2002. CP: 2002 WILEY-VCH Verlag GmbH, Weinheim, Fed. Rep. of Germany; PN: 0935-9648.

[45] H. Yokokawa and T. Horita, *Cathodes*, p. 142. High temperature solid oxide fuel cells: fundamentals, design and applications, Oxford, U.K.: Elsevier Ltd., 2003.

[46] J. M. Vohs and R. J. Gorte, "High-performance sofc cathodes prepared by infiltration," *Advanced Materials*, vol. 21, no. 9, pp. 943–956, 2009. CP: Copyright 2009 WILEY-VCH Verlag GmbH & Co. KGaA, Weinheim; PN: 0935-9648.

[47] A. Evans, A. Bieberle-Hütter, J. L. M. Rupp, and L. J. Gauckler, "Review on microfabricated micro-solid oxide fuel cell membranes," *Journal of Power Sources*, vol. 194, pp. 119–129, 10/20 2009.

[48] D. Beckel, A. Bieberle-Hütter, A. Harvey, A. Infortuna, U. P. Muecke, M. Prestat, J. L. M. Rupp, and L. J. Gauckler, "Thin films for micro solid oxide fuel cells," *Journal of Power Sources*, vol. 173, pp. 325–345, 11/8 2007.

[49] S. Rey-Mermet and P. Muralt, "Solid oxide fuel cell membranes supported by nickel grid anode," *Solid State Ionics*, vol. 179, pp. 1497–1500, 9/30 2008.

[50] H. Huang, M. Nakamura, P. Su, R. Fasching, Y. Saito, and F. B. Prinz, "High-performance ultrathin solid oxide fuel cells for low-temperature operation," *Journal of the Electrochemical Society*, vol. 154, pp. B20–B24, 2007 2007.

[51] A. Bieberle-Hütter, M. Søgaard, and H. L. Tuller, "Electrical and electrochemical characterization of microstructured thin film $La_{1-x}Sr_xCoO_3$ electrodes," *Solid State Ionics*, vol. 177, pp. 1969–1975, 10/15 2006.

[52] M. Prestat, J. F. Koenig, and L. J. Gauckler, "Oxygen reduction at thin dense $La_{0.52}Sr_{0.48}Co_{0.18}Fe_{0.82}O_{3-\delta}$ electrodes," *Journal of Electroceramics*, vol. 18, pp. 87–101, 2007.

[53] F. S. Baumann, J. Fleig, H. U. Habermeier, and J. Maier, "$Ba_{0.5}Sr_{0.5}Co_{0.8}Fe_{0.2}O_{3-\delta}$ thin film microelectrodes investigated by impedance spectroscopy," *Solid State Ionics*, vol. 177, pp. 3187–3191, 11/30 2006.

[54] L. Dieterle, P. Bockstaller, D. Gerthsen, J. Hayd, E. Ivers-Tiffée, and U. Guntow, "Microstructure of nanoscaled $La_{0.6}Sr_{0.4}CoO_{3-\delta}$ cathodes for intermediate-temperature solid oxide fuel cells," *Advanced Energy Materials*, vol. 1, no. 2, pp. 249–258, 2011.

[55] A. J. Darbandi and H. Hahn, "Nanoparticulate cathode thin films with high electrochemical activity for low temperature SOFC applications," *Solid State Ionics*, vol. 180, pp. 1379–1387, 10/19 2009.

[56] A. Evans, A. Bieberle-Hütter, H. Galinski, J. L. M. Rupp, T. Ryll, B. Scherrer, R. Toelke, and L. J. Gauckler, "Micro-solid oxide fuel cells: status, challenges, and chances," *Monatshefte für Chemie / Chemical Monthly*, vol. 140, no. 9, pp. 975–983, 2009.

[57] Y. Huang, K. Ahn, J. M. Vohs, and R. J. Gorte, "Characterization of Sr-doped $LaCoO_3$-YSZ composites prepared by impregnation methods," *Journal of the Electrochemical Society*, vol. 151, pp. A1592–A1597, 2004 2004.

[58] Y. Huang, J. M. Vohs, and R. J. Gorte, "Characterization of LSM-YSZ composites prepared by impregnation methods," *Journal of the Electrochemical Society*, vol. 152, pp. A1347–A1353, 2005 2005.

[59] M. Shah and S. A. Barnett, "Solid oxide fuel cell cathodes by infiltration of $La_{0.6}Sr_{0.4}Co_{0.2}Fe_{0.8}O_{3-\delta}$ into Gd-doped ceria," *Solid State Ionics*, vol. 179, pp. 2059–2064, 10/30 2008.

[60] J. D. Nicholas and S. A. Barnett, "Measurements and modeling of $Sm_{0.5}Sr_{0.5}CoO_{3-x}$-$Ce_{0.9}Gd_{0.1}O_{1.95}$ SOFC cathodes produced using infiltrate solution additives," *Journal of the Electrochemical Society*, vol. 157, pp. B536–B541, 2010 2010.

[61] F. Zhao, R. Peng, and C. Xia, "LSC-based electrode with high durability for IT-SOFCs," *Fuel Cells Bulletin*, vol. 2008, pp. 12–16, 2 2008.

[62] F. Zhao, Z. Wang, M. Liu, L. Zhang, C. Xia, and F. Chen, "Novel nano-network cathodes for solid oxide fuel cells," *Journal of Power Sources*, vol. 185, pp. 13–18, 10/15 2008. M3: doi: DOI: 10.1016/j.jpowsour.2008.07.022.

[63] E. P. Murray, M. J. Sever, and S. A. Barnett, "Electrochemical performance of (La,Sr)(Co,Fe)O_3-(Ce,Gd)O_3 composite cathodes," *Solid State Ionics*, vol. 148, pp. 27–34, 5/1 2002.

[64] F. Zhao, R. Peng, and C. Xia, "A $La_{0.6}Sr_{0.4}CoO_{3-\delta}$-based electrode with high durability for intermediate temperature solid oxide fuel cells," *Materials Research Bulletin*, vol. 43, pp. 370–376, 2/5 2008.

[65] J. Hayd, L. Dieterle, U. Guntow, D. Gerthsen, and E. Ivers-Tiffée, "Nanoscaled $La_{0.6}Sr_{0.4}CoO_{3-\delta}$ as intermediate temperature solid oxide fuel cell cathode: Microstructure and electrochemical performance," *Journal of Power Sources*, vol. 196, pp. 7263–7270, 9/1 2011.

[66] V. V. Kharton, F. M. B. Marques, and A. Atkinson, "Transport properties of solid oxide electrolyte ceramics: a brief review," *Solid State Ionics*, vol. 174, pp. 135–149, 10/29 2004.

[67] R. H. E. van Doorn and A. J. Burggraaf, "Structural aspects of the ionic conductivity of $La_{1-x}Sr_xCoO_{3-\delta}$," *Solid State Ionics*, vol. 128, pp. 65–78, 2 2000.

[68] B. Gharbage, F. Mandier, H. Lauret, C. Roux, and T. Pagnier, "Electrical properties of $La_{0.5}Sr_{0.5}MnO_3$ thin films," *Solid State Ionics*, vol. 82, pp. 85–94, 11/15 1995.

[69] H. B. Wang, J. F. Gao, D. K. Peng, and G. Y. Meng, "Plasma deposition of $La_{0.8}Sr_{0.2}MnO_3$ thin films on yttria-stabilized zirconia from aerosol precursor," *Materials Chemistry and Physics*, vol. 72, pp. 297–300, 12/1 2001.

[70] S. Mentus, D. Jelic, and V. Grudic, "Lanthanum nitrate decomposition by both temperature and programmed heating and citrate gel combustion," *Journal of Thermal Analysis and Calorimetry*, vol. 90, no. 2, p. 393, 2007.

[71] K. H. Stern, "High temperature properties ans decomposition of inorganic salts part 3. nitrates and nitrites," *Journal of Physical and Chemical Reference Data*, vol. 1, no. 3, pp. 747–772, 1972.

[72] A. E. Gobichon, J. P. Auffrédic, and D. Louër, "Thermal decomposition of neutral and basic lanthanum nitrates studied with temperature-dependent powder diffraction and thermogravimetric analysis," *Solid State Ionics*, vol. 93, pp. 51–64, 12 1996.

[73] A. Mineshige, J. Izutsu, M. Nakamura, K. Nigaki, J. Abe, M. Kobune, S. Fujii, and T. Yazawa, "Introduction of A-site deficiency into $La_{0.6}Sr_{0.4}Co_{0.2}Fe_{0.8}O_{3-\delta}$ and its effect on structure and conductivity," *Solid State Ionics*, vol. 176, pp. 1145–1149, 3/31 2005.

[74] P. Gordes, N. Chrsitiansen, E. J. Jensen, and J. Villadsen, "Synthesis of perovskite-type compounds by drip pyrolysis," *Journal of Materials Science*, vol. 30, pp. 1053–1058, 1995.

[75] J. E. Mortensen, M. Søgaard, and T. Jacobsen, "Impedance modeling of solid oxide fuel cell cathodes," *ECS Transactions*, vol. 28, pp. 17–38, October 8, 2010 2010.

[76] S. B. Adler, J. A. Lane, and B. C. H. Steele, "Electrode kinetics of porous mixed-conducting oxygen electrodes," *Journal of the Electrochemical Society*, vol. 143, pp. 3554–3564, November 1996 1996.

[77] C. Peters, A. Weber, and E. Ivers-Tiffeé, "Nanoscaled $La_{0.5}Sr_{0.5}CoO_{3-\delta}$ thin film cathodes for SOFC application at 500°C < T < 700°C," *Journal of the Electrochemical Society*, vol. 155, pp. B730–B737, 2008 2008.

[78] J. Januschewsky, M. Ahrens, A. Opitz, F. Kubel, and J. Fleig, "Optimized $La_{0.6}Sr_{0.4}CoO_{3-\delta}$ thin-film electrodes with extremely fast oxygen-reduction kinetics," *Advanced Functional Materials*, vol. 19, no. 19, pp. 3151–3156, 2009.

[79] P. S. Jørgensen, K. V. Hansen, R. Larsen, and J. R. Bowen, "A framework for automatic segmentation in three dimensions of microstructural tomography data," *Ultramicroscopy*, vol. 110, pp. 216–228, 2 2010.

[80] A. Mineshige, M. Inaba, T. Yao, Z. Ogumi, K. Kikuchi, and M. Kawase, "Crystal structure and metal-insulator transition of $La_{1-x}Sr_xCoO_3$," *Journal of Solid State Chemistry*, vol. 121, pp. 423–429, 2/1 1996.

[81] T. Ishigaki, S. Yamauchi, J. Mizusaki, K. Fueki, and H. Tamura, "Tracer diffusion coefficient of oxide ions in $LaCoO_3$ single crystal," *Journal of Solid State Chemistry*, vol. 54, pp. 100–107, 8 1984.

[82] J. Mizusaki, Y. Mima, S. Yamauchi, K. Fueki, and H. Tagawa, "Nonstoichiometry of the perovskite-type oxides $La_{1-x}Sr_xCoO_{3-\delta}$," *Journal of Solid State Chemistry*, vol. 80, pp. 102–111, 5 1989.

[83] A. Mai, M. Becker, W. Assenmacher, F. Tietz, D. Hathiramani, E. Ivers-Tiffée, D. Stöver, and W. Mader, "Time-dependent performance of mixed-conducting SOFC cathodes," *Solid State Ionics*, vol. 177, pp. 1965–1968, 10/15 2006.

[84] A. Mai, V. A. C. Haanappel, S. Uhlenbruck, F. Tietz, and D. Stöver, "Ferrite-based perovskites as cathode materials for anode-supported solid oxide fuel cells: Part I. variation of composition," *Solid State Ionics*, vol. 176, pp. 1341–1350, 5/12 2005.

[85] L. Dieterle, D. Bach, R. Schneider, H. Störmer, D. Gerthsen, U. Guntow, E. Ivers-Tiffée, A. Weber, C. Peters, and H. Yokokawa, "Structural and chemical properties of nanocrystalline $La_{0.5}Sr_{0.5}CoO_{3-\delta}$ layers on yttria-stabilized zirconia analyzed by transmission electron microscopy," *Journal of Materials Science*, vol. 43, pp. 3135–3143, 2008.

[86] Y. Xiong, K. Yamaji, T. Horita, H. Yokokawa, J. Akikusa, H. Eto, and T. Inagaki, "Sulfur poisoning of SOFC cathodes," *Journal of the Electrochemical Society*, vol. 156, pp. B588–B592, 2009 2009.

[87] K. Yamahara, C. P. Jacobson, S. J. Visco, and L. C. D. Jonghe, "Catalyst-infiltrated supporting cathode for thin-film SOFCs," *Solid State Ionics*, vol. 176, pp. 451–456, 2/14 2005.

[88] N. Imanishi, R. Ohno, K. Murata, A. Hirano, Y. Takeda, O. Yamamoto, and K. Yamahara, "LSM-YSZ cathode with infiltrated cobalt oxide and cerium oxide nanoparticles," *Fuel Cells*, vol. 9, no. 3, pp. 215–221, 2009.

[89] Y. Huang, J. M. Vohs, and R. J. Gorte, "An examination of LSM-LSCo mixtures for use in sofc cathodes," *Journal of the Electrochemical Society*, vol. 153, pp. A951–A955, 2006 2006.

[90] A. Petric, P. Huang, and F. Tietz, "Evaluation of La-Sr-Co-Fe-O perovskites for solid oxide fuel cells and gas separation membranes," *Solid State Ionics*, vol. 135, pp. 719–725, 11/1 2000.

[91] S. Sakamoto, M. Yoshinaka, K. Hirota, and O. Yamaguchi, "Fabrication, mechanical properties, and electrical conductivity of Co_3O_4 ceramics," *Journal of the American Ceramic Society*, vol. 80, no. 1, pp. 267–268, 1997.

[92] M. Søgaard, P. V. Hendriksen, M. Mogensen, F. W. Poulsen, and E. Skou, "Oxygen nonstoichiometry and transport properties of strontium substituted lanthanum cobaltite," *Solid State Ionics*, vol. 177, pp. 3285–3296, 12 2006.

[93] Y. Ji, J. A. Kilner, and M. F. Carolan, "Electrical conductivity and oxygen transfer in gadolinia-doped ceria (CGO)-$Co_3O_{4-\delta}$ composites," *Journal of the European Ceramic Society*, vol. 24, pp. 3613–3616, 11 2004.

[94] J. A. Lane and J. A. Kilner, "Oxygen surface exchange on gadolinia doped ceria," *Solid State Ionics*, vol. 136137, pp. 927–932, 11/2 2000.

[95] K. Yamahara, C. P. Jacobson, S. J. Visco, X.-F. Zhang, and L. C. D. Jonghe, "Thin film SOFCs with cobalt-infiltrated cathodes," *Solid State Ionics*, vol. 176, pp. 275–279, 1/31 2005.

[96] A. A. Yaremchenko, V. V. Kharton, E. N. Naumovich, and F. M. B. Marques, "Physicochemical and transport properties of BICUVOX-based ceramics," *Journal of Electroceramics*, vol. 4, pp. 233–242, 1999.

[97] H. Hayashi, M. Kanoh, C. J. Quan, H. Inaba, S. Wang, M. Dokiya, and H. Tagawa, "Thermal expansion of Gd-doped ceria and reduced ceria," *Solid State Ionics*, vol. 132, pp. 227–233, 7/2 2000.

[98] J. S. Ahn, D. Pergolesi, M. A. Camaratta, H. Yoon, B. W. Lee, K. T. Lee, D. W. Jung, E. Traversa, and E. D. Wachsman, "High-performance bilayered electrolyte intermediate temperature solid oxide fuel cells," *Electrochemistry Communications*, vol. 11, pp. 1504–1507, 7 2009.

[99] Z. Gao, Z. Mao, J. Huang, R. Gao, C. Wang, and Z. Liu, "Composite cathode $La_{0.15}Bi_{0.85}O_{1.5}$-Ag for intermediate-temperature solid oxide fuel cells," *Materials Chemistry and Physics*, vol. 108, pp. 290–295, 4/15 2008.

[100] W. Wang, M. D. Gross, J. M. Vohs, and R. J. Gorte, "The stability of LSF-YSZ electrodes prepared by infiltration," *Journal of the Electrochemical Society*, vol. 154, pp. B439–B445, 2007 2007.

[101] T. Z. Sholklapper, V. Radmilovic, C. P. Jacobson, S. J. Visco, and L. C. D. Jonghe, "Synthesis and stability of a nanoparticle-infiltrated solid oxide fuel cell electrode," *Electrochemical and Solid-State Letters*, vol. 10, pp. B74–B76, 2007 2007.

[102] S. C. Singhal and K. Kendall, *High temperature solid oxide fuel cells: fundamentals, design, and applications*. Oxford, UK: Elsevier Ltd., 2003.

[103] J. T. S. Irvine, J. W. L. Dobson, T. Politova, S. G. Martin, and A. Shenouda, "Co-doping of scandia-zirconia electrolytes for SOFCs," *Faraday Discussions*, vol. 134, pp. 41–49, 2007.

[104] J. Yang, H. Muroyama, T. Matsui, and K. Eguchi, "A comparative study on polarization behavior of (La,Sr)MnO_3 and (La,Sr)CoO_3 cathodes for solid oxide fuel cells," *International Journal of Hydrogen Energy*, vol. 35, pp. 10505–10512, 10 2010.

[105] V. Dusastre and J. A. Kilner, "Optimisation of composite cathodes for intermediate temperature SOFC applications," *Solid State Ionics*, vol. 126, pp. 163–174, 11/1 1999.

[106] W. G. Wang and M. Mogensen, "High-performance lanthanum-ferrite-based cathode for SOFC," *Solid State Ionics*, vol. 176, pp. 457–462, 2/14 2005.

[107] H. Ullmann, N. Trofimenko, F. Tietz, D. Stöver, and A. Ahmad-Khanlou, "Correlation between thermal expansion and oxide ion transport in mixed conducting perovskite-type oxides for SOFC cathodes," *Solid State Ionics*, vol. 138, pp. 79–90, 12/1 2000.

[108] I. Yasuda, Y. Matsuzaki, T. Yamakawa, and T. Koyama, "Electrical conductivity and mechanical properties of alumina-dispersed doped lanthanum gallates," *Solid State Ionics*, vol. 135, pp. 381–388, 11/1 2000.

[109] N. V. Nong, N. Pryds, S. Linderoth, and M. Ohtaki, "Enhancement of the thermoelectric performance of p-type layered oxide $Ca_3Co_4O_{9+\delta}$ through heavy doping and metallic nanoinclusions," *Advanced Materials*, vol. 23, pp. 2484–2490, 2011.

[110] K. Nagasawa, S. Daviero-Minaud, N. Preux, A. Rolle, P. Roussel, H. Nakatsugawa, and O. Mentré, "$Ca_3Co_4O_{9-\delta}$: A thermoelectric material for SOFC cathode," *Chemistry of Materials*, vol. 21, pp. 4738–4745, 09/14; 10/13 2009; 2009. doi: 10.1021/cm902040v; M3: doi: 10.1021/cm902040v.

[111] A. Rolle, S. Boulfrad, K. Nagasawa, H. Nakatsugawa, O. Mentré, J. Irvine, and S. Daviero-Minaud, "Optimisation of the solid oxide fuel cell (SOFC) cathode material $Ca_3Co_4O_{9-\delta}$," *Journal of Power Sources*, vol. 196, pp. 7328–7332, 9/1 2011.

[112] A. C. Masset, C. Michel, A. Maignan, M. Hervieu, O. Toulemonde, F. Studer, B. Raveau, and J. Hejtmanek, "Misfit-layered cobaltite with an anisotropic giant magnetoresistance: $Ca_3Co_4O_9$," *Physical Review B*, vol. 62, p. 166, 07/01/ 2000. ID: 10.1103/PhysRevB.62.166; J1: PRB.

[113] U. P. Muecke, K. Akiba, A. Infortuna, T. Salkus, N. V. Stus, and L. J. Gauckler, "Electrochemical performance of nanocrystalline nickel/gadolinia-doped ceria thin film anodes for solid oxide fuel cells," *Solid State Ionics*, vol. 178, pp. 1762–1768, 1/31 2008.

[114] J. Shimoyama, S. Horii, K. Otzschi, M. Sano, and K. Kishio, "Oxygen nonstoichiometry in layered cobaltite $Ca_3Co_4O_y$," *Japanese Journal of Applied Physics*, vol. 42, no. Part 2, No. 2B, p. L194. ID: 10.1143/JJAP.42.L194; M1: Copyright (C) 2003 The Japan Society of Applied Physics.

[115] M. Tahashi, T. Tanimoto, H. Goto, M. Takahashi, and T. Ido, "Sintering temperature dependence of thermoelectric performance and crystal phase of calcium cobalt oxides," *Journal of the American Ceramic Society*, vol. 93, no. 10, pp. 3046–3048, 2010.

[116] T. Kenjo, S. Osawa, and K. Fujikawa, "High temperature air cathodes containing ion conductive oxides," *Journal of the Electrochemical Society*, vol. 138, pp. 349–355, February 1991 1991.

[117] C. W. Tanner, K.-Z. Fung, and A. V. Virkar, "The effect of porous composite electrode structure on solid oxide fuel cell performance," *Journal of the Electrochemical Society*, vol. 144, pp. 21–30, January 1997 1997.

[118] J. H. Nam and D. H. Jeon, "A comprehensive micro-scale model for transport and reaction in intermediate temperature solid oxide fuel cells," *Electrochimica Acta*, vol. 51, pp. 3446–3460, 4/25 2006.

[119] S. Farhad and F. Hamdullahpur, "Optimization of the microstructure of porous composite cathodes in solid oxide fuel cells," *AIChE Journal*, pp. n/a–n/a, 2011.

[120] X. J. Chen, S. H. Chan, and K. A. Khor, "Simulation of a composite cathode in solid oxide fuel cells," *Electrochimica Acta*, vol. 49, pp. 1851–1861, 4/30 2004.

[121] P. Costamagna, P. Costa, and V. Antonucci, "Micro-modelling of solid oxide fuel cell electrodes," *Electrochimica Acta*, vol. 43, no. 3-4, pp. 375–394, 1998.

[122] F. Bidrawn, R. Kungas, J. M. Vohs, and R. J. Gorte, "Modeling impedance response of SOFC cathodes prepared by infiltration," *Journal of the Electrochemical Society*, vol. 158, pp. B514–B525, 2011 2011.

[123] M. Shah, J. D. Nicholas, and S. A. Barnett, "Prediction of infiltrated solid oxide fuel cell cathode polarization resistance," *Electrochemistry Communications*, vol. 11, pp. 2–5, 1 2009.

[124] M. Søgaard, P. V. Hendriksen, T. Jacobsen, and M. Mogensen, "Modeling of the polarization resistance from surface exchange and diffusion coeffficient data," in *Proceedings of the 7th european solid oxide fuel cell fourm* (U. Bossel, ed.), July 3-7, 2006 2006.

[125] M. Suzuki and T. Oshima, "Estimation of the co-ordination number in a multicomponent mixture of spheres," *Powder Technology*, vol. 35, pp. 159–166, 8 1983.

[126] D. Bouvard and F. F. Lange, "Relation between percolation and particle coordination in binary powder mixtures," *Acta Metallurgica et Materialia*, vol. 39, pp. 3083–3090, 12 1991.

[127] C. H. Kuo and P. K. Gupta, "Rigidity and conductivity percolation thresholds in particulate composites," *Acta Metallurgica et Materialia*, vol. 43, pp. 397–403, 1 1995.

[128] H. He, Y. Huang, J. Regal, M. Boaro, J. M. Vohs, and R. J. Gorte, "Low-temperature fabrication of oxide composites for solid-oxide fuel cells," *Journal of the American Ceramic Society*, vol. 87, no. 3, pp. 331–336, 2004. PN: 0002-7820.

[129] J. Sanyal, G. M. Goldin, H. Zhu, and R. J. Kee, "A particle-based model for predicting the effective conductivities of composite electrodes," *Journal of Power Sources*, vol. 195, pp. 6671–6679, 10/1 2010.

[130] P. S. Jørgensen, K. V. Hansen, R. Larsen, and J. R. Bowen, "Geometrical characterization of interconnected phase networks in three dimensions," *Journal of microscopy*, pp. no–no, 2011.

[131] P. S. Jørgensen, K. V. Hansen, R. Larsen, and J. R. Bowen, "High accuracy interface characterization of three phase material systems in three dimensions," *Journal of Power Sources*, vol. 195, pp. 8168–8176, 12/15 2010.

[132] E. A. Mason and A. P. Malinauskas, *Gas Transport in Porous Media: The Dusty Gas Model*. New York: Elsevier, 1983.

[133] E. A. Mason and H. K. Lonsdale, "Statistical-mechanical theory of membrane transport," *Journal of Membrane Science*, vol. 51, pp. 1–81, 7/15 1990.

[134] R. E. Williford, L. A. Chick, G. D. Maupin, S. P. Simner, and J. W. Stevenson, "Diffusion limitations in the porous anodes of SOFCs," *Journal of the Electrochemical Society*, vol. 150, pp. A1067–A1072, August 2003 2003.

[135] E. N. Fuller, P. D. Schettler, and J. C. Giddings, "New method for prediction of binary gas-phase diffusion coefficients," *Industrial & Engineering Chemistry*, vol. 58, no. 5, p. 18, 1966.

[136] B. Todd and J. B. Young, "Thermodynamic and transport properties of gases for use in solid oxide fuel cell modelling," *Journal of Power Sources*, vol. 110, pp. 186–200, 7/20 2002.

[137] R. B. Bird, W. E. Stewart, and E. N. Lightfoot, *Transport Phenomena*. New York: Wiley & Sons, 2nd ed., 2002.

[138] F. S. Baumann, J. Fleig, G. Cristiani, B. Stuhlhofer, H. U. Habermeier, and J. Maier, "Quantitative comparison of mixed conducting SOFC cathode materials by means of thin film model electrodes," *Journal of the Electrochemical Society*, vol. 154, pp. B931–B941, 2007 2007.

[139] M. Kubicek, A. Limbeck, T. Fromling, H. Hutter, and J. Fleig, "Relationship between cation segregation and the electrochemical oxygen reduction kinetics of $La_{0.6}Sr_{0.4}CoO_{3-\delta}$ thin film electrodes," *Journal of the Electrochemical Society*, vol. 158, pp. B727–B734, 2011 2011.

[140] S. H. Chan, X. J. Chen, and K. A. Khor, "Cathode micromodel of solid oxide fuel cell," *Journal of the Electrochemical Society*, vol. 151, pp. A164–A172, 2004 2004.

[141] Y. H. Lin, C. W. Nan, Y. Liu, J. Li, T. Mizokawa, and Z. Shen, "High-temperature electrical transport and thermoelectric power of partially substituted

$Ca_3Co_4O_9$-based ceramics," *Journal of the American Ceramic Society*, vol. 90, no. 1, pp. 132–136, 2007.